University of Stellenbosch

Wideband Direction Finding of RFI for MeerKAT

by
Mourits de Beer

Thesis presented in fulfilment of the requirements for the degree Master of Engineering in the Faculty of Engineering at Stellenbosch University

Supervisors:
Dr. P. G. Wiid & Prof. D. B. Davidson

March 2017

The financial assistance of the National Research Foundation (NRF) towards this research is hereby acknowledged. Opinions expressed and conclusions arrived at, are those of the author and are not necessarily to be attributed to the NRF.

Stellenbosch University https://scholar.sun.ac.za

Declaration

By submitting this thesis electronically, I declare that the entirety of the work contained therein is my own original work, that I am the authorship owner thereof (unless to the extent explicitly otherwise stated) and that I have not previously in its entirety or in part submitted it for obtaining any qualification.

Signature: .....

Date: March 2017

Copyright © 2017 Stellenbosch University
All rights reserved

Stellenbosch University https://scholar.sun.ac.za

Abstract

The Karoo desert in the Northern Cape of South Africa is currently host to the MeerKAT radio telescope – a precursor facility for the Square Kilometre Array (SKA) project. The area was selected due to its natural quietness from man-made sources of radio-frequency interference (RFI), as the telescope site needs to uphold demanding electromagnetic compatibility (EMC) standards in order to perform sensitive radio astronomy observations. It is therefore necessary that the facility monitors the spectrum across MeerKAT's operational bandwidth to identify the presence of noise sources that may compromise the integrity of future measurements. This thesis presents the design and simulation of a direction finding (DF) solution that will prove to be an essential means of locating and mitigating on-site or outside sources of interference. The asymptotic conical dipole (ACD) antenna is implemented with a 3D-printed plastic design, coated in metal to achieve an impedance bandwidth greater than 100:1. Four units of these designs are manufactured for use in a multi-receiver system, which applies a phase correlation DF algorithm to estimate the bearing of an impulse source. The accuracy of arbitrary antenna configurations is investigated by simulation to evaluate the performance under noisy conditions. Field measurements are conducted that verify the simulated angular resolution of the system, which obtains source angle estimates within $\pm 2.5^\circ$ accuracy.

Stellenbosch University https://scholar.sun.ac.za

Opsomming

Die Karoo woestein-gebied in die Noord Kaap provinsie van Suid Afrika is tans die tuiste van die MeerKAT radio teleskoop wat as voorloper tot die SKA-projek dien. Die area is gekies weens die natuurlike afwesigheid van mensgemaakte radiogolf-steurings. Die terrein moet voldoen aan baie hoë vereistes ten op sigte van elektro-magnetiese-aanpasbaarheidstandaarde, ten einde die doelstelling van hoogs sen-sitiewe sterrekundige waarnemings te kan bemagtig. Dit is dus noodsaaklik vir die fasiliteit om die operasionele frekwensie-spektrum te monitor, om die teen-woordigheid van seinsteurings, wat die waarnemings kan beinvloed, te identifiseer. Hierdie tesis bied die ontwerp van ‘n rigtingsvinding stelsel, wat van kardinale be-lang sal wees in die aanduiding en versagting van steuringsbronne. ‘n Asimtoties-koniese dipool-antenna, wat met 3-D drukkers uit plastiek geskep is en dan met metaal oorgetrek is, word gebruik om ‘n bandwydte-impedansie van meer as 100:1 te behaal. Vier eenhede, volgens diè ontwerp, is vervaardig vir die gebruik in ‘n multi-ontvangerstelsel, waar die toepassing van ’n fase-korrelasie rigtingsvinding-algoritme, die oorsprong van steurings bereken. Die akkuraatheid van arbitrêre antenna konfigurasies is ondersoek en evalueer deur die gebruik van gesimuleerde waarnemings onder steuringsomstandighede. Waarnemings tydens praktiese toetse bevestig die hoek resolusie van die stelselkonfigurasie met ‘n akuraatheid binne $\pm 2.5^\circ$ ten opsigte van die ware invalshoek.

Stellenbosch University https://scholar.sun.ac.za

Acknowledgements

"A hundred times every day I remind myself that my inner and outer life are based on the labors of other men, living and dead, and that I must exert myself in order to give in the same measure as I have received and am still receiving . . . "

—Albert Einstein

The work contained within this thesis is a result of the influence and contribution of countless people – both near, and far; past, and present. But above all, it is the result of the direct contribution of those mentioned here.

I would like to express my sincerest thanks to Dr. Gideon Wiid, for his continued guidance throughout this project, and for providing the necessary insight to stay on track;

To Prof. Davidson, for the expertise that fostered new ideas;

To Joely Andriambeloson, for his invested efforts in guaranteeing the success of the final measurements;

A special thanks to Wessel Croukamp, for all the extended hours that was spent on the planning and manufacturing of the antennas;

To Anneke Bester, for her valuable contribution to all the antenna measurements performed;

To Wynand van Eeden, for trusting me with his 3D printer;

To Antheun Botha and Hardie Pienaar, for their helpful advice in a time of uncertainty;

To my sister, Dyani, for being my personal guru and doctor – literally;

And to my loving parents, Ian and Analda, for their unending support in the pursuit of my ambitions, and for teaching me that if something is worth doing, it is worth doing right.

Stellenbosch University https://scholar.sun.ac.za

Table of Contents

Stellenbosch University https://scholar.sun.ac.za

Stellenbosch University https://scholar.sun.ac.za

Stellenbosch University https://scholar.sun.ac.za

List of Figures

Stellenbosch University https://scholar.sun.ac.za

Stellenbosch University https://scholar.sun.ac.za

List of Tables

Stellenbosch University https://scholar.sun.ac.za

Nomenclature

Abbreviations

ACD	Asymptotic Conical Dipole
AoA	Angle of Arrival
ASKAP	Australian Square Kilometre Array Pathfinder
DF	Direction Finding
DSP	Digital Signal Processing
ITU	International Telecommunication Union
KAPB	Karoo Array Processing Building
KAT	Karoo Array Telescope
MWA	Murchison Widefield Array
PLF	Polarisation Loss Factor
RF	Radio-Frequency
RFI	Radio-Frequency Interference
RMSE	Root-Mean-Square Error
SHF	Super High Frequency
SKA	Square Kilometre Array
SNR	Signal-to-Noise Ratio
TDOA	Time Difference of Arrival
UHF	Ultra High Frequency
VLA	Very Large Array

Stellenbosch University https://scholar.sun.ac.za

VNA	Vector Network Analyser
VSWR	Voltage Standing Wave Ratio

Constants

ϵ_0	Vacuum permittivity — 8.854×10^{-12} Farads per metre
c	Speed of light in a vacuum — 299 792 458 metres per second

Symbols

Γ	Voltage reflection coefficient
λ	Wavelength
ϕ	Angular coordinate (azimuthal angle in spherical system)
θ	Angular coordinate (elevation angle in spherical system)
B	Bandwidth
D	Directivity
e	Efficiency
G	Gain
I	Current
P	Power
r	Radial distance in spherical coordinate system
U	Radiation intensity
V	Voltage
Z	Impedance
dB	Decibels
dBi	Decibels relative to isotropic radiator

Stellenbosch University https://scholar.sun.ac.za

Chapter 1

Introduction

"There is now a feeling that the pieces of physics are falling into place, not because of any single revolutionary idea or because of the efforts of any one physicist, but because of a flowering of many seeds of theory, most of them planted long ago."

—Steven Weinberg

1.1 The SKA Project

The Square Kilometre Array (SKA) project is an international endeavour in engineering and science to develop the world's largest and most sensitive radio telescope. The objective of the design is to have an effective collecting area of 1 square kilometre. For comparison, the Karl G. Jansky Very Large Array (VLA), which is currently the most sensitive telescope over L-band (1–2 GHz) in the world, has approximately 13 000 square metres collecting area [1]. The SKA will therefore be up to 100 times more sensitive than present capabilities. The only way for such a large area to be covered, is by utilising thousands of antennas in an interferometric array, with receiving stations spread over the world. The scale of the array will provide a greater field of view of the sky, allowing for higher resolution images and significantly faster survey speeds than is currently feasible.

The candidate locations for the SKA core sites included areas in Argentina, Australia, China, South Africa, and the USA. The factors that contributed to selecting these sites were, among others, the infrastructure cost and having predictable weather patterns, but the most critical concern was the levels of radio-frequency interference (RFI), which must be as low as possible for the weak signals from distant space to be measured with high fidelity. As a result, the SKA Organisation decided in 2012 that the Australian and South African bids were strongest, and that the SKA telescopes would be constructed in both countries: the Mid West region of Australia, and the Northern Cape of South Africa. [2]

Stellenbosch University https://scholar.sun.ac.za

Figure 1.1: MeerKAT dishes in operation at the core site in the Karoo, South Africa, pictured in April 2016 [3]. The empty, foundation structures are prepared for future dishes.

The SKA will be developed in two phases: SKA1 and SKA2. Phase 1 will consist of two separate instruments: the low frequency array in Australia (SKA1-Low) and the mid-high frequency array in South Africa (SKA1-Mid). The Australian SKA Pathfinder (ASKAP) radio telescope and the Murchison Widefield Array (MWA) represent the precursor facilities of SKA1-Low. ASKAP and MWA are innovative observatories in their own right, but their primary purpose is to lay the foundation for future development. More than one hundred thousand antennas will be spread between 500 stations in Western Australia to provide a collecting area of 0.4 km^2, over the frequency range 50–350 MHz. SKA2 will further expand the sites to include up to a million antennas [4].

South Africa's precursor facility, the seven-dish Karoo Array Telescope (KAT-7), finished construction in 2010 [5], and served as the proof of concept before extending development to the 64-dish MeerKAT[1]. The telescope operates over the frequency range 0.5–14.5 GHz, and will represent the foundation of SKA1-Mid. In July 2016, MeerKAT consisted of 16 offset Gregorian dishes (some shown in Figure 1.1), with scientific observations in progress. The full array of 64 dishes is expected to be operational by the end of 2017 [6]. Once MeerKAT is complete, SKA1 construction will expand the Karoo site to host 197 dishes [7]. This will provide 10% of the target capability of the full SKA, as SKA2 is planned to roll out thousands of additional dishes in the Northern Cape, as well as distant stations across the eight SKA African partner countries: Botswana, Ghana, Kenya, Madagascar, Mauritius, Mozambique, Namibia, and Zambia [8].

The high sensitivity of the full array will permit observations of distant and ancient signals that were generated in the early universe, which will provide un-

[1]MeerKAT literally means *more of KAT*.

Stellenbosch University https://scholar.sun.ac.za

precedented insight into the history of the cosmos. The SKA will therefore become a revolutionary platform for scientific investigations in cosmology, physics, astrophysics, and astrobiology. Nevertheless, the success of the science relies on countless engineering challenges first being resolved.

1.2 MeerKAT and the Problem of RFI

The Karoo desert is a naturally RFI-quiet area, due to its remoteness and some fortunate landscape features – surrounding flat-topped hills serve as a natural shield. With the extremely high sensitivity goals of the SKA, it is critical that this low-RFI advantage of the site is maintained. As a result, the South African government introduced the Astronomy Geographic Advantage Act [9], which prohibits and restricts the use of the RF spectrum from 100 MHz up to 25.5 GHz. This act is enforced within the Central Astronomy Advantage Area, which makes up a size that is roughly equal to a circle of 200 km radius around the core site [10]. However, the concern still remains that emissions will be generated by the facility itself.

The MeerKAT telescopes are connected via a data communications network to the Karoo Array Processor Building (KAPB), an underground facility for data storage and digital signal processing (DSP). The building was carefully designed to minimise any potential RFI leakage: power cabling is located in screened enclosures wherever possible; the data storage lab is fully shielded with steel panels; earthing is provided to protect against lightning strikes; and soil berms were constructed around the KAPB to further limit any RFI emissions in the direction of the antennas. Furthermore, all electrical designs were prepared with the foresight that inevitable scaling out will be required. The eventual big data problem will demand large expansion of the local network and power capacity: as the number of telescopes increases, so will the power requirement, the data-throughput rates, and the size of the data storage centre. Therefore, several studies have been and are being conducted on shielding characteristics [11], mitigation techniques [12], propagation models [13], and the electromagnetic coupling between telescopes [14], all as a collaborative effort to better understand how interference will be monitored and managed.

Together with the challenge of mitigating on-site emissions, there exists the potential that transient, sporadic sources of RFI can occur unmonitored. Short-duration bursts of energy may occur from sparking electric fences or power lines. Sufficiently large impulses may be capable of saturating the electronic receivers, corrupting data not only in the frequency range of the noise, but across the telescope's bandwidth. Additionally, a visitor's car, cellphone, or laptop, may be the source of irregular noise. Therefore, it is an essential part of the successful operation of MeerKAT and the SKA that the spectral environment is monitored in real-time throughout development and operation, to ensure that RFI sources can be identified and mitigated.

Stellenbosch University https://scholar.sun.ac.za

1.3 Thesis Objectives

The primary objective of this thesis is to develop a direction finding (DF) system that is capable of accurately resolving the angle towards a source of RFI. This must be achieved for transient interference signals over the processing bandwidth of the MeerKAT telescopes. We therefore have the initial requirement to design an omnidirectional antenna capable of operating from 580 MHz up to 14.5 GHz. A secondary objective is for the antenna design to implement a low-cost methodology with 3D-printed plastic, so that several such antennas can be readily manufactured to make up the receiver component of the DF system. A DSP based algorithm must then be developed to process the measured time-domain signals and yield an estimated angle of arrival (AoA) for the incoming wavefronts. This algorithm must be applied in a calibrated measurement to verify that estimated AoA results are accurate within a $\pm 2.5^\circ$ angular resolution – a standard benchmark for DF systems.

1.4 Contributions

The original contributions provided in this thesis include the following:

1.4.1 Design of a Novel, Ultra-Wideband Antenna

The DF system requires an omnidirectional, wideband antenna, which will serve as the receiver for detecting interference signals that exist over MeerKAT's bandwidth. It is desirable for the receivers to operate with as low a cut-off frequency as possible, while maintaining a small antenna size. A study of bandwidth enhancement techniques, applied to different antenna configurations, is investigated by simulation, and leads to the development of a novel, 3D-printed, asymptotic conical dipole design that achieves an impedance bandwidth in excess of 100:1.

1.4.2 Implementation of a Phase Correlation DF Algorithm and Simulation Tool

The algorithm for the DF system is developed with the phase correlation method, and is designed to provide reconfigurable simulation results to assess the angular resolution and ambiguity resistance of arbitrary receiver configurations. An asymmetrical antenna layout is shown to demonstrate wideband direction finding capabilities, in contrast to the narrowband limitations of symmetrical layouts. The expected results provided by the simulation are verified by field measurements, which test these two configurations using four manufactured units of the wideband receivers. Measurements demonstrate that sufficient signal-to-noise ratios are obtained to accurately resolve the angle of a pulse source within 2.5° angular resolution.

Stellenbosch University https://scholar.sun.ac.za

1.5 Overview of Contents

Chapter 2 provides a review of the literature that comprises the background for the antenna design process. Relevant antenna theory is covered, in order to introduce the criteria that define how performance characteristics are assessed. Techniques to enhance antenna bandwidth are discussed, together with the candidate designs that are considered for the DF application. This is followed by an overview and comparison of different DF methods, where the functionality of phase correlation is explained with greater emphasis, as this method is employed for the implementation of the DF algorithm.

Chapter 3 focuses on the antenna design, covering the simulation results and the investigations that were made. Bandwidth enhancement techniques are applied in FEKO to a conical antenna, and the improved performance is compared with that of an asymptotic conical dipole. The manufacturing process of the final, selected design is presented, and followed by final measurement results.

Chapter 4 provides an overview of the functionality of the designed DF algorithm. The inner workings of the applied phase correlation method is covered such that the presented code can be reconfigured as desired. The importance of the receiver configuration is investigated by simulating the AoA estimation accuracy under various, noisy conditions. Results are presented over a wide frequency range to show how the prevalence of ambiguity errors varies for the different layouts.

Finally, the manufactured antennas were utilised in combination with the DF algorithm, in a field measurement setup that is presented in Chapter 5. A pulse source was placed in known locations, with a series of time-domain measurements obtained for two separate antenna configurations. The captured data is processed and applied with the phase correlation algorithm, to compare the AoA estimation accuracy with the expected performance that is generated by simulation.

Stellenbosch University https://scholar.sun.ac.za

Chapter 2

Literature Review

"... the only laws of matter are those which our minds must fabricate, and the only laws of mind are fabricated for it by matter."

—James Clerk Maxwell

2.1 Introduction

This chapter provides an overview of the theoretical framework that is required to understand the design process presented in Chapters 3 and 4, and the results obtained throughout. Definitions of principles and nomenclature are explained only insofar as necessary to cover the scope of this project. Therefore, the primary topics are on antennas and direction finding. Fundamental antenna characteristics and parameters are introduced in order to evaluate the performance of key types of antennas that are considered. This is followed by discussion on the DF principle, presenting different techniques and their applications.

2.2 Antenna Theory

Most discussions on antenna theory are prefaced with an introduction to electromagnetism and Maxwell's equations. For the purposes of this section, it is sufficient to know that EM waves propagate through free space at the speed of light, and that EM radiation is generated by accelerating electric currents. This implies that constant velocity current (such as DC) that moves along a straight wire will not generate any radiation, unless the wire is curved, bent, or discontinuous (such as at the ends of the wire), because these features result in a change of charge direction or velocity. Oscillating current (such as the AC power from residential wall sockets) is time-varying and will radiate even on a straight wire. [15, p. 10]

An antenna is a device that converts electrical currents in conductors into EM radiation in free space, or vice versa. This principle is illustrated in Figure 2.1. The

Stellenbosch University https://scholar.sun.ac.za

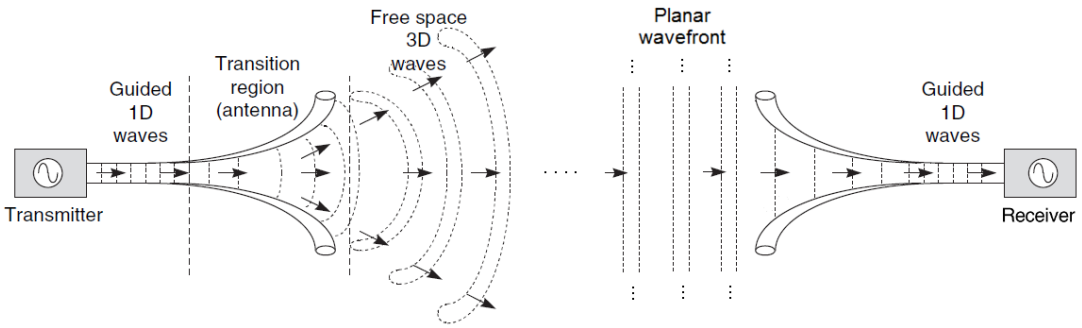

Figure 2.1: An antenna depicted as a transition region between guided and propagating waves [16, p. 61]. It is important to note that passive antenna systems are reciprocal, and work equally well as transmitter or receiver.

goal of antenna design is to ensure that the conversion between current and radiation occurs as efficiently as possible, and that power is transmitted or received with desired characteristics. The following subsection will expand on these characteristics by detailing some of the definitions and parameters that are important in describing the performance.

2.2.1 Fundamentals of Antennas

The way that an antenna radiates is determined by its geometry: the physical wires or surfaces over which currents and fields are distributed. The dimensions of the geometry is the major feature that determines which signal frequencies will radiate most effectively. Material properties or physical features (such as bends, folds, turns or cuts) will alter the resonant point in different ways, and so the number of potential antenna designs is effectively limitless.

In free space, all EM radiation travels at the same speed. The wavelength of a signal is therefore inversely proportional to its frequency, as described by

$$c = f\lambda, \tag{2.1}$$

where c is the speed of light, f is the frequency [Hz] and λ is the wavelength [m]. This shows the relationship between an antenna's size and its frequency of operation: as an antenna is scaled larger, the resonant wavelength increases, resulting in the radiation of lower frequency signals. As an aside, there are materials, such as glass, plastics and ceramics, which have dielectric properties that reduce the speed of EM waves as a function of frequency. This results in non-linear scaling of wavelength such that it is not quite inversely proportional to the frequency. As discussed later in Section 2.2.2, these materials can be used to improve an antenna's performance at low frequencies, and extend its total bandwidth, while maintaining a small antenna size.

Stellenbosch University https://scholar.sun.ac.za

Table 2.1: Common frequency bands and their application

Frequency Band Name	**Frequency Range**	**Wavelength**	**Example Application**
Extremely Low Frequency (ELF)	3–30 Hz	10 000–100 000 km	Underwater communication
Super Low Frequency (SLF)	30–300 Hz	1 000–10 000 km	AC power
Ultra Low Frequency (ULF)	300–3 000 Hz	100–1 000 km	Audio, music
Very Low Frequency (VLF)	3–30 kHz	10–100 km	Navigational beacons
Low Frequency (LF)	30–300 kHz	1–10 km	AM radio
Medium Frequency (MF)	300–3 000 kHz	100–1 000 m	AM radio and aviation
High Frequency (HF)	3–30 MHz	10–100 m	Shortwave radio, over-the-horizon radar
Very High Frequency (VHF)	30–300 MHz	1–10 m	FM radio, television broadcasts
Ultra High Frequency (UHF)	300–3 000 MHz	10–100 cm	Television, mobile phones, GPS
Super High Frequency (SHF)	3–30 GHz	1–10 cm	Radio astronomy, satellite comms
Extremely High Frequency (EHF)	30–300 GHz	1–10 mm	Radio astronomy, remote sensing
Visible Spectrum *Not regulated by ITU	400–790 THz	380–750 nm	Human vision

Frequency bands and interference

Antenna engineers have, over the years, subdivided the radio spectrum into frequency bands that are allocated for specific applications or users. This is necessary to prevent interference between different telecommunication systems. For instance, FM radio wouldn't work if every station shared the same broadcasting frequency. Today, use of the spectrum is regulated by national laws, which is overseen by the International Telecommunication Union (ITU). Table 2.1 shows the radio bands as divided by the ITU, with some example applications.

The MeerKAT radio telescope will operate over a very wide bandwidth, across UHF and part of SHF (specifically L-band, 1–2 GHz, and X-band, 8–12 GHz), and so there is a great range over which noise can corrupt the radio astronomy measurements. As listed in the table, the primary background interference will come from TV and mobile networks. This is the reason that the Astronomy Geographic Advantage Act was created, to restrict such broadcasts around the area [9]. Some other

Stellenbosch University https://scholar.sun.ac.za

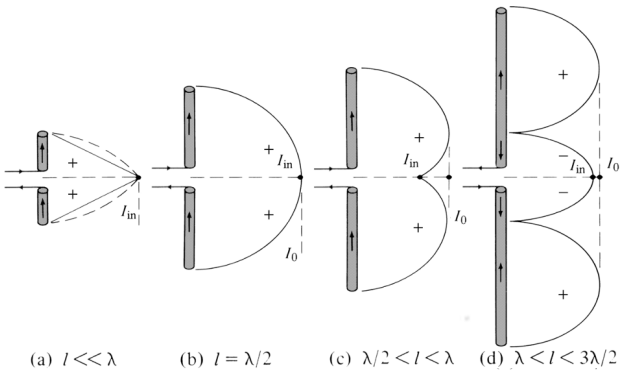

Figure 2.2: Current distributions on a linear dipole [15, p. 19]. I_{in} is the input current, and I_0 the maximum amplitude.

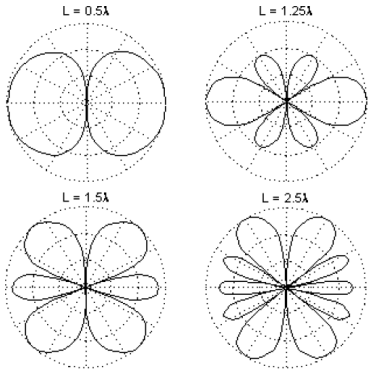

Figure 2.3: Vertical cuts showing frequency effect on dipole radiation pattern [18, p. 3-4.1].

technology that operates within these bands include Bluetooth and WiFi, which may be active on a visitor's cellphone or laptop. Radio-navigation and communications technology on aircraft flying around the reserve will also be problematic. In addition, there may exist sporadic noise sources that will irregularly release bursts of energy, such as sparking electric fences. Langat [17] characterises the radiation from power lines, and sparking noise was found to contain significant energy across a broad spectrum, from below 50 MHz to beyond 3.6 GHz.

Due to the wide range of potential interference sources that would need to be monitored, MeerKAT will require a system that can accurately resolve the direction of signals that constitute part of environmental noise, as well as for transient, sporadic bursts of energy.

Radiation of a dipole

For a centre-fed wire dipole, resonance occurs at signal lengths of $\frac{\lambda}{2}$. This concept is illustrated in Figure 2.2, by comparing the current distribution on a dipole at different signal lengths. It is important to note that Figures 2.2(a-d) can be considered to represent the same dipole with equivalent *physical* length, l, but the *signal* length changes at different frequencies. (b) represents what is "seen" by the signal at the resonant frequency. This is the point at which a maximum amount of energy is radiated, and hence there is a minimum amount of energy reflected back to the transmitter. (a) represents signal frequencies below this point, and (c-d) frequencies above this point.

When $l > \lambda$ it is shown that current polarity begins to reverse along the wire. This creates stark changes in the directions that energy is radiated, as shown in Figure 2.3. The illustrated patterns show a view of the angular distribution of radiated energy, for a vertical dipole viewed from the front.

Stellenbosch University https://scholar.sun.ac.za

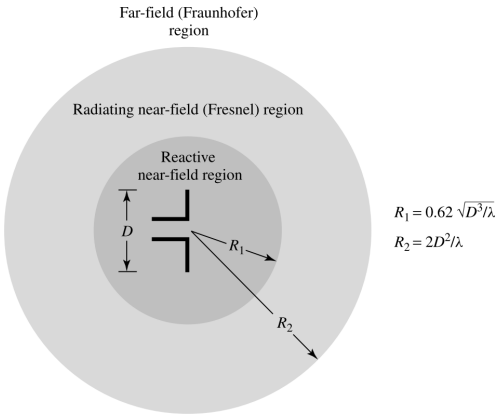

Figure 2.4: Field regions of an antenna [15, p. 34]. D represents the maximum antenna dimension, and R the region boundaries.

Field regions

When describing the EM fields that are radiated from an antenna, it is useful to divide the surrounding space into three regions: the reactive near-field, the radiating near-field, and the far-field, as shown in Figure 2.4. The space that immediately surrounds an antenna, the reactive near-field region, is an area where reactive energy predominates the radiating energy. That is to say that within this region there is a greater amount of stored energy, which returns to the antenna in each cycle, than there is transmitted energy. Because of this, the distribution of fields varies rapidly as one moves away from the antenna. If the antenna is large compared to the signal wavelength ($D > \lambda$), the reactive near-field is taken to be bounded by a distance

$$R < 0.62\sqrt{D^3/\lambda}, \tag{2.2}$$

where D is the largest dimension of the antenna. Beyond this boundary exists the radiating near-field, or Fresnel region, wherein reactive energy still exists, but is now predominated by radiated energy. EM fields continue to vary with distance, until we reach the far-field, or Fraunhofer region, at the distance

$$R > 2D^2/\lambda. \tag{2.3}$$

Within this region, reactive energy can be considered negligible, and the angular distribution of EM fields becomes independent of distance. [15, pp. 34–35]

When measuring the radiation characteristics of an antenna, it is especially important to be aware of the near- and far-field region boundaries. Radiated power must be measured well within the far-field, otherwise additional efforts must be spent to account for the influence of the reactive fields. Furthermore, other metal objects must be kept out of the antenna's near-field, as they will couple with the reactive energy and alter the antenna's impedance characteristics. [16, p. 63]

Stellenbosch University https://scholar.sun.ac.za

Radiation pattern and directivity

The far-field distribution of radiated energy is of great importance in antenna design, because it shows how much energy is transmitted from or received by the antenna, for any given direction. The distribution is typically represented graphically as a function of angular coordinates, in what is called the radiation pattern.

Here it is helpful to introduce the hypothetical concept of the isotropic source: an ideal radiator that emits equally in all directions. The radiation pattern therefore resembles a sphere. This provides a reference for classifying the radiation performance of real antennas. For an isotropic source that radiates a total power of P_{rad}, the measured power density S (in W/m^2) at a distance r is [16, Eq. (4.5)]

$$S = \frac{P_{rad}}{\text{area}} = \frac{P_{rad}}{4\pi r^2}, \tag{2.4}$$

because the power is spread over a sphere of radius r. This quantity can be made independent of distance by simply factoring it out, giving the definition for radiation intensity U (in Watts per unit solid angle) of an isotropic radiator [16, Eq. (4.6)]:

$$U_0 = r^2 S = \frac{P_{rad}}{4\pi}. \tag{2.5}$$

Now we define the *directivity* of an antenna as the ratio of radiation intensity in a specific angular direction (θ, ϕ) and its total radiation intensity averaged over all directions. This average is identical to the radiation intensity of the isotropic radiator emitting the same amount of power. Therefore, the directivity D may be expressed mathematically [15, Eq. (2-16)]:

$$D(\theta, \phi) = \frac{U(\theta, \phi)}{U_0} = \frac{4\pi U(\theta, \phi)}{P_{rad}}. \tag{2.6}$$

This quantity is an expression of how well the radiated energy is focused in any direction. An antenna with high directivity concentrates its radiation over a smaller area. If the directivity is expressed without a specified angular direction, then it usually implies that it is the maximum directivity over all directions. The quantity is dimensionless, and is commonly expressed in decibels. The units are then given in dBi to emphasise that it is relative to the isotropic radiator:

$$D[\text{dBi}] = 10 \log D. \tag{2.7}$$

It is important to note that directivity is expressed in terms of *radiated* power. The *total* power that is input to a practical antenna system will undergo ohmic and mismatch losses, due to resistive heating and reflected energy, and so the resulting radiated power is always less than the input power.

It is typically desirable to design an antenna that is either directional or omni-directional. An example of both these types of patterns is shown in Figures 2.5

Stellenbosch University https://scholar.sun.ac.za

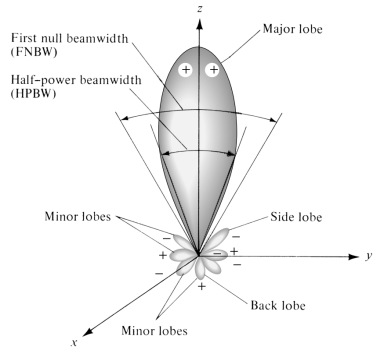

Figure 2.5: A highly directional pattern showing definitions for radiation lobes [15, Fig. 2.3].

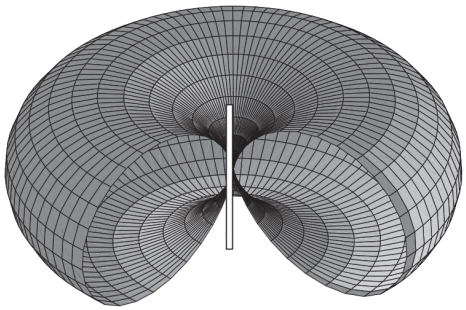

Figure 2.6: 3D radiation pattern of a short dipole [16, p. 66]. A section has been cut away to reveal detail.

and 2.6, indicating how the radiated energy is concentrated. These beams of energy are called *lobes*, where the maximum energy is contained in the major lobe. Side and back lobes are usually unintended consequences of the frequency effect, as previously discussed for the radiation of a dipole.

Radiation and directivity patterns are often shown as 2D cuts of the 3D distribution. An omnidirectional pattern would therefore be directional in the elevation plane (viewed from the front) and non-directional in the azimuth plane (viewed from above). Figure 2.3 provides an example of an elevation plane view.

Antenna impedance and efficiency

The equivalent circuit diagram of a transmitting antenna is shown in Figure 2.7, where a transmitter with source impedance $Z_s = R_s + jX_s$ feeds into an antenna with impedance $Z_a = R_r + R_l + jX_a$. The antenna's resistance is composed of the *radiation resistance* R_r and a *loss resistance* R_l. These components represent, respectively, the power that is dissipated through radiated energy, and the power lost in the conducting or dielectric parts of the antenna. Radiation is the desired output of the system, and so we can define the antenna efficiency as [16, Eq. (4.12)]

$$e = \frac{\text{Power radiated}}{\text{Power accepted by antenna}} = \frac{R_r}{R_r + R_l}. \tag{2.8}$$

It is evident that efficiency is a dimensionless quantity between 0 and 1. In order to improve radiation efficiency, we desire minimal ohmic and dielectric losses.

There is an additional measure of efficiency that associates the power transfer from the source to the antenna. The difference between source impedance Z_s and antenna impedance Z_a determines the proportion of power that is accepted by the antenna. If the impedance conjugates are equal[1], then the system is said to

[1]Conjugately equal refers to the complex number expression for impedance. The source and antenna resistances must be equal, but the reactances must negate one another: $X_s = -X_a$.

Stellenbosch University https://scholar.sun.ac.za

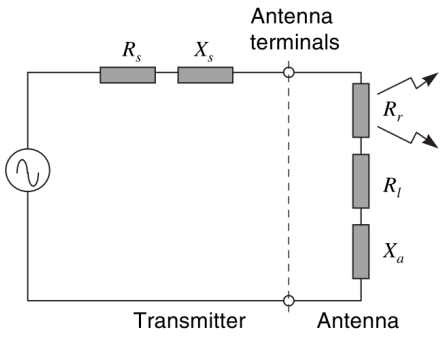

Figure 2.7: Equivalent circuit of transmitting antenna [16, p. 67].

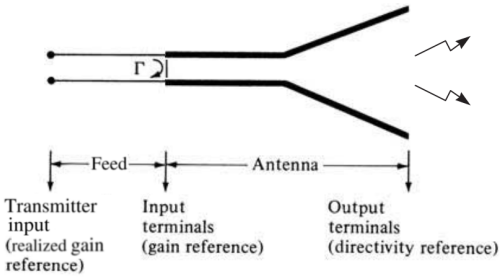

Figure 2.8: Reference terminals of feed and antenna [15, p. 65].

be matched, and maximum power is transferred. If a high impedance antenna is driven by a low impedance source, or vice versa, then it results in some energy being reflected at the terminal boundaries (as indicated at the feed on Figure 2.8). The degree of mismatch is measured using the voltage reflection coefficient Γ (also called return loss), which is defined by [16, Eq. (4.13)]

$$\Gamma = \frac{V_r}{V_i} = \frac{Z_a - Z_s}{Z_a + Z_s}, \tag{2.9}$$

where V_i and V_r are the amplitudes of the voltage waves that are incident from the source onto the antenna terminals and reflected back from the antenna to the source, respectively. Network ports and transmission lines are commonly designed to have a characteristic impedance of 50 Ω, and antennas are usually designed to match this value accordingly. The greater the mismatch, the greater the reflected energy. From this, the reflection efficiency can be expressed [15, p. 65]

$$e_r = 1 - |\Gamma|^2. \tag{2.10}$$

Reflection efficiency is an important measure of an antenna's performance, and so, sensibly, there is more than one expression for it. A common measure for impedance mismatch is the *voltage standing wave ratio* (VSWR), which has an optimal value of 1: [16, Eq. (4.14)]

$$\text{VSWR} = \frac{1 + |\Gamma|}{1 - |\Gamma|}. \tag{2.11}$$

In addition, we also have the *scattering parameters*, or S-parameters, which is used to express the proportional voltage transfer between terminals of an N-port network. The parameter S_{ij} is defined as the ratio of voltage wave V_i^- out of port i as a result of the voltage wave V_j^+ applied to port j. S_{11} is therefore equivalent to the expression for reflection coefficient in Eq. 2.9, as follows:

$$S_{11} = \frac{{V_1}^-}{{V_1}^+} = \frac{V_r}{V_i} = \Gamma. \tag{2.12}$$

Stellenbosch University https://scholar.sun.ac.za

Gain

As previously discussed, directivity is defined in terms of radiated power, and not the actual accepted power. The combination of antenna efficiency e and reflection efficiency e_r in Eq. 2.8 and 2.10 expresses the proportion of input power that is converted to radiation. By combining directivity with these efficiencies, we obtain antenna patterns with losses taken into account. These new expressions are the *power gain* and *realised gain*, which give improved measure of true system performance. Power gain only takes the antenna losses into account, whereas realised gain also includes the system's mismatch losses. This is expressed mathematically as follows [15, p. 66]:

$$\begin{aligned} \mathrm{G}_{power}(\theta,\phi) &= eD(\theta,\phi), \\ \mathrm{G}_{realised}(\theta,\phi) &= e_r eD(\theta,\phi). \end{aligned} \tag{2.13}$$

It is evident that there is only a scale factor difference between these parameters, and so their plots will have the same shape. This is why the terms are often used interchangeably, but it is important to note the distinction. The reference terminals for the definitions of each parameter are indicated on Figure 2.8. For a full system design, it is most advantageous to work with realised gain.

The gain of a transmitter or receiver is practically measured by setting up two antennas directed at one another. Either one of the antenna's gain distributions must be known in order to solve for the gain of the other. The relationship is expressed by the Friis transmission equation [15, Eq. (2-119)]

$$\frac{P_r}{P_t} = \left(\frac{\lambda}{4\pi R}\right)^2 G_t G_r, \tag{2.14}$$

which relates the power P_t that is input to the transmitter to the power P_r that is received. If the separation distance is in the far-field of the larger antenna ($R > 2D^2/\lambda$), then the unknown gain can be solved.

Polarisation

An EM wave can be characterised according to the orientation of its electric field vector. This vector is coupled with a magnetic field vector, which lie orthogonal to each other and to the direction of wave travel. The *polarisation* of a wave describes the variation in the electric field that is traced out in space as the wave propagates.

For the radiated fields from a dipole, the electric vector is polarised linearly, in line with the orientation of the wire. A dipole can therefore only receive waves that are polarised in the same plane. In general, there is a power loss associated with a mismatch of polarisation. The polarisation loss factor (PLF), or polarisation efficiency, is expressed mathematically as [15, p. 76]

$$\mathrm{PLF} = |\cos\psi|^2, \tag{2.15}$$

Stellenbosch University https://scholar.sun.ac.za

where ψ is the angle between polarisation of the wave and the antenna. It is clear if $\psi = 90°$, then PLF $= 0$ and there will be no received power. This is because a horizontally polarised wave will not excite any fields over a vertically polarised antenna, and vice versa. The basic Friis equation (Eq. 2.14) assumes that polarisations are matched, but there are modified forms that take additional losses into account [15, p. 95].

Linearly polarised waves have an electric field with only one directional component, but there may exist two orthogonal components, each with their own magnitude and time-phase relative to the other. The geometric figure that is traced over time by the sum of these electric field components is, in general, an ellipse, with either a clockwise or counter-clockwise rotation. Circular polarisation is a case that arises when the magnitude of the vectors are equal and right out of phase.

All measures of directivity and gain are evaluated for one specific polarisation, in the same way that they are taken at one frequency point.

Bandwidth

The *bandwidth* of an antenna is a measure of the range of frequencies that can be varied over while still obtaining an acceptable radiation pattern with minimal losses. Bandwidth is usually expressed by the range of lower and upper cut-off frequencies F_L and F_U. For antennas with a narrow band of operation, it is better expressed as a percentage around a centre frequency F_C, as follows:

$$B = \frac{F_U - F_L}{F_C} \cdot 100\%. \tag{2.16}$$

For broadband antennas it is more appropriate to define bandwidth as a ratio:

$$B = \frac{F_U}{F_L}, \tag{2.17}$$

which is typically used when $B > 2:1$, or, correspondingly, when $B > 66\%$.

The conditions for defining an acceptable band depend on the system specifications, and so the precise criteria for defining bandwidth can be fairly fluid. For instance, a system may require a receiver with power gain greater than 3 dBi, which will by definition have a narrower bandwidth of operation than the same system if it only required gain greater than 0 or -3 dBi. Therefore, there are different bandwidths for each condition. Reflection losses are commonly deemed acceptable when Γ or $S_{11} < -10$ dB, which corresponds to a VSWR less than $2:1$. The band over which this condition is satisfied will be referred to as the *impedance bandwidth*.

Stellenbosch University https://scholar.sun.ac.za

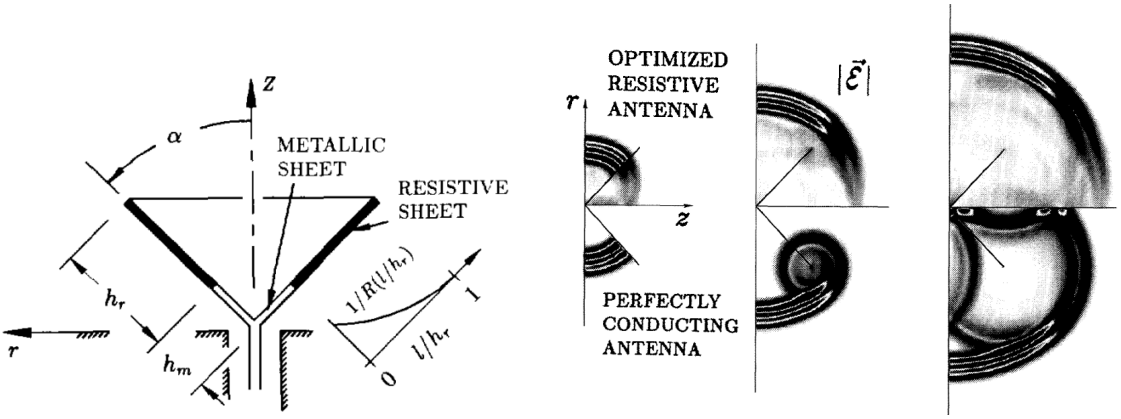

(a) Geometry of a resistively loaded monocone [20, Fig. 1]. The resistance profile is shown as $1/R$ over length.

(b) Radiation of a pulse over time is compared for a loaded and non-loaded cone [20, Fig. 5]. The loaded design radiates without reflection.

Figure 2.9: Resistive loading applied to a monocone.

2.2.2 Techniques to Enhance Antenna Bandwidth

The geometry of an antenna determines how it radiates, while its material properties determine the loss resistance R_L and reactance X_a. Antennas are almost exclusively composed of only highly conductive metals, which provide maximum radiation efficiency, but materials can be added to yield different responses. The added material will absorb power by ohmic heating, but may be applied wittingly to improve the antenna impedance. Therefore, with proper technique, it is possible to trade off some efficiency for a wider band of operation.

Resistive loading

In 1965, Wu and King [19] released their seminal paper on the analysis of adding a distributed internal impedance over an antenna's length. This of course reduces the efficiency, but Wu and King proved that applying a particular distribution of impedance (a loading profile) over the antenna's length, the efficiency can be traded off optimally for an improved bandwidth.

Maloney [20] provides the design of a resistively loaded conical antenna that is optimised for pulse radiation. A diagram of the loaded monocone's geometry is show in Figure 2.9(a), with comparison of a resistive and a metal antenna's radiation shown in (b).

Resistive loading works because it flattens the antenna's impedance response over frequency, such that it can be matched over a wider band. A typical loading profile would have a gradual, almost linear increase in impedance (5–20 Ω) over the first two thirds of the antenna's length, after which it increases exponentially, with very high impedance (500–2000 Ω) at the ends. Such an impedance profile causes

Stellenbosch University https://scholar.sun.ac.za

the energy that has not yet been radiated to be dissipated at the ends, instead of being reflected. With loading, efficiency levels can be expected to fall around 50–60%, but the Wu-King impedance profile is usually scaled to moderate between the desired characteristics.

Dielectric coating

As was mentioned at the beginning of Section 2.2.1, dielectric mediums have the property of changing the speed of EM wave propagation, typically with variable response over frequency. Dielectrics can therefore be applied onto an antenna to reduce or increase its electrical length, in turn shifting the resonant frequency up or down, respectively [15, p. 513]. As with resistive loading, the additional material results in more power being dissipated as heat, again as a trade-off between efficiency and improved bandwidth. According to [15, p. 515], however, it is not a very efficient technique to broadband the antenna, due to the high loss of most materials. Therefore, careful consideration needs to be made in order to find material that is appropriate for a specific application.

A comprehensive study of dielectric coating applied to a monopole is available in [21]. It is stated that commercial materials can be useful to improve on some antenna designs, but in general, research may be necessary to acquire or synthesise materials with desired characteristics. Most critically, the materials need to be low-loss, with suitable permittivity values over the frequency range of interest. Therefore, it is largely a material sciences problem, and, fortunately, significant developments are being made. Wang et al. [22] discusses the synthesis of ceramics with very high permittivity ($> 10^4$ F/m) and low dielectric loss. Moon et al. [23] investigates different compositions of epoxy-dielectrics (10–100 F/m) with an emphasis on adjusting concentrations to yield varied permittivity responses over frequency. These advancements provide new possibilities for antenna engineers, with a lot of potential applications to be explored.

2.2.3 The Bicone and Monocone

The biconical antenna (see Figure 2.10) has long been studied due to its simple geometric configuration and broadband characteristics. The reason for its wide bandwidth is best understood when considering the theoretical case of an infinitely long bicone: since it has no ends, the infinite bicone could be scaled with no change to its shape, and it is therefore a frequency independent structure [15, Ch. 11]. A practical bicone must of course be truncated, which limits the operational bandwidth, and introduces reflections from the ends.

The characteristics of the bicone is also theoretically realisable as a monocone above a ground plane. From image theory [15, p. 185], the conducting ground plane reflects a mirror image of the cone, as illustrated in Figure 2.11. The finite ground plane introduces its own set of reflections, and its size has a significant effect on

Stellenbosch University https://scholar.sun.ac.za

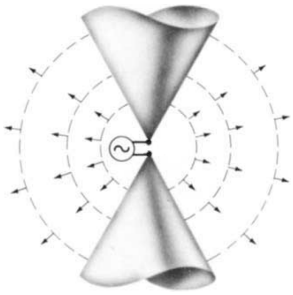

Figure 2.10: Geometry of bicone with radiated spherical waves [15, p. 500].

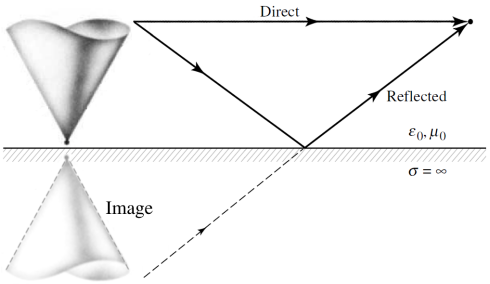

Figure 2.11: Monocone above a ground plane creates a reflected image.

the far-field radiation pattern. With proper design, the monocone has been proven to give good omnidirectional gain over a wide band. Typical performance can be expected to give a power gain of 0–4 dBi, over a 4:1 bandwidth [18, p. 3-3.6].

Previous work

The initial design considerations that are discussed in Chapter 3 is an extension of the past work of Dr Gideon Wiid and Dr Joely Andriambeloson.

Wiid [24] designed an optimised monocone for wideband matching to a 50 Ω system. It was found that an angle of 41° between the cone and ground plane yielded optimal realised gain and reflection efficiency. Measurements of the 75 cm diameter cone show that a -10 dB impedance bandwidth of 35:1 was obtained, from 140 MHz up to 4.9 GHz.

Andriambeloson [25] investigated the same 41° angle design, utilising a 3D-printed plastic structure coated with conductive paint as a light-weight, low-cost design method. An 18 cm diameter cone obtained an impedance bandwidth of 20:1 from 430 MHz up to 8.5 GHz, demonstrating that carbon- and nickel-based paints provide suitable properties for antenna design. This provided the motivation to implement a 3D-printed design, as presented in Chapter 3.

2.2.4 The Asymptotic Conical Dipole

In 1952, two pioneers of advanced electromagnetic theory, Sergei A. Schelkunoff and Harald T. Friis, introduced the analysis of a tapered biconical design, such that it has a uniformly distributed capacitance [26]. This design later became known as the asymptotic conical dipole (ACD), and is also referred to as the Schelkunoff-Friis antenna. The geometry of the ACD is shown in Figure 2.12(a), and is defined according to a curve that is revolved around its axis to obtain a symmetrical, three-dimensional shape. The contour is determined in [27, Eq. (2)] to be:

$$r = h\left[\frac{(1+k)\cos\theta + (1-k)}{(1+k)\cos\theta + (1-k)\cos^2\theta}\right], \tag{2.18}$$

Stellenbosch University https://scholar.sun.ac.za

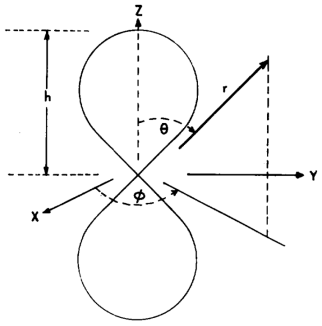

(a) Shape of the ACD [27, Fig. 1].

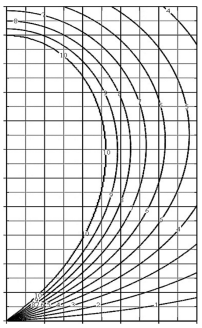

(b) The contour shape determines the input impedance. Wider contours have lower impedance. [28, Fig. 2]

Figure 2.12: Geometry of the asymptotic conical dipole.

where

$$k = e^{4\pi\epsilon_0 \frac{V}{q}}. \tag{2.19}$$

The variables r and θ refer to the polar coordinates over which the contour is sketched. The maximum height of the design is determined by the scaling factor h, whereas the shape or width of the contour is determined by the desired ratio of potential (V) and charge (q) on the line. The contour is only evaluated up to an angle θ such that $0 \leq r \leq h$. Therefore, θ is bounded up to [27, Eq. (4)]:

$$\theta_{\max} = \cos^{-1}\left(\frac{k-1}{k+1}\right). \tag{2.20}$$

Simpson [28] uses quasi-static analysis to obtain the following expression for the antenna's characteristic impedance:

$$Z = \frac{nV}{cq}, \tag{2.21}$$

where c is the speed of light and n is a constant that corresponds to the design of a monopole ($n = 1$) or a dipole ($n = 2$). Jacobs et al. [29] conducted a parametric study to determine whether the relation in Eq. 2.21 provides an adequate design guideline for an ACD antenna's input impedance. It is said that the approximation is improved by altering the values of n to be 1.25 for a monopole and 2.5 for a dipole.

By rearranging Eq. 2.21 in terms of V/q, and substituting into Eq. 2.19, we can design the ACD curve in terms of a desired impedance Z:

$$k = e^{(4\pi\epsilon_0 c/n)Z}. \tag{2.22}$$

For increasing values of Z we obtain thinner contours. Figure 2.12(b) shows how the shape varies for different impedance designs.

In Chapter 3, various ACD curves are investigated alongside the cone antenna to find a suitable design for the DF application.

Stellenbosch University https://scholar.sun.ac.za

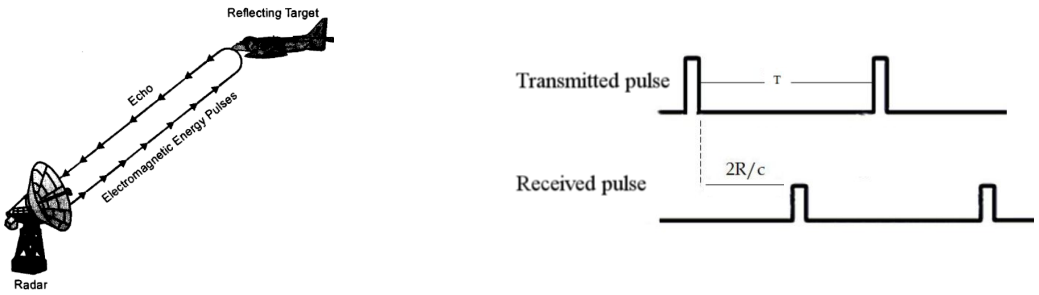

(a) The transmitted signal arrives at and reflects off the metallic target. Some of the scattered waves return to the receiver. [30]

(b) The time difference between transmitting and receiving a pulse indicates the range (R) of the target.

Figure 2.13: A basic example of the radar principle.

2.3 Radio Direction Finding

The idea to use radio waves to locate an object was conceived from the experiments of Heinrich Hertz in the late 19th century, after it was proven that electromagnetic waves are reflected by metallic objects. This discovery led to the development of early radar[2] systems for military applications, capable of geolocating navy vessels or aircraft. The basic functionality of such a system is shown in Figure 2.13. The range of the target can either be approximated from the ratio of transmitted and received power, or by measuring the time delay of the reflected signal.

The bearing of the target can be estimated according to numerous methods: a single directional antenna (with known gain pattern) can be rotated across the desired field of view – the angle of maximum received power then corresponds to the approximate angle of the target; to improve the angular resolution, several receivers can be used in combination, to triangulate the source. The geometric layout of the receivers introduces a set of time and phase delays, which provides information to the system. In the case of directional antennas with known patterns, there is further angular information that can be extracted from the power amplitudes.

Passive direction finding is the act of listening without transmitting. The first applications were in warfare and security surveillance, but is now also used in radio-monitoring, to search for sources of interference. In contrast to radar, passive systems have no prior knowledge of the signal properties; there is no comparison between a transmitted and a received signal. The consequence of this lack of information is that it is much more difficult to deduce the range of a source. To obtain accurate range information, a passive DF system would require receivers that are separated on the order of kilometres (for an area as large as the Karoo). On the other hand, the methods to infer the angle of arrival (AoA) remain much the same,

[2]RADAR was first coined as an acronym for RAdio Detection And Ranging. The term was later adopted as a common noun, losing all capitalization.

Stellenbosch University https://scholar.sun.ac.za

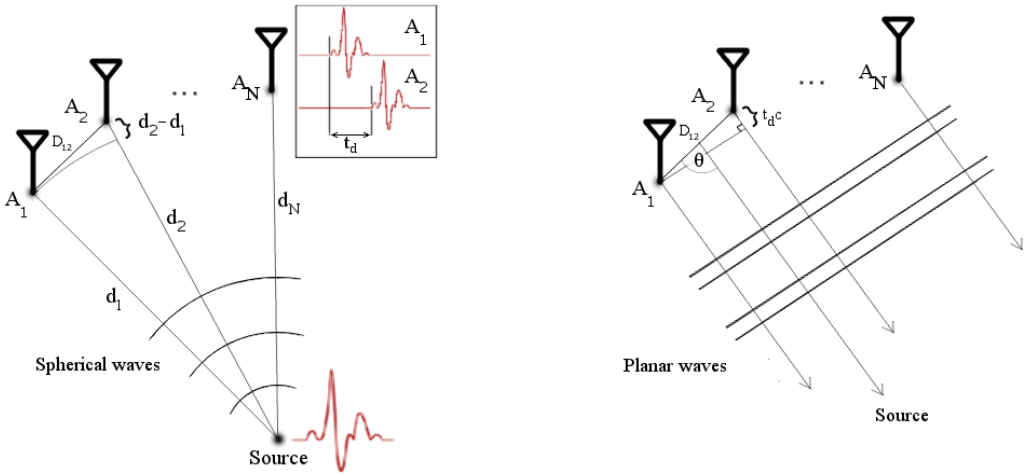

(a) Receiving a pulse from a nearby source. (b) Receiving a pulse from far away.

Figure 2.14: Illustration of the time difference of arrival method.

in that it can be deduced by comparing power amplitudes, time delays or phase shifts across multiple receivers. Each comparison method offers its own degree of accuracy, sensitivity, angular resolution, and immunity to reflections. [31]

A minimum of two antennas is required for DF to work, but it is important to note that this case will guarantee ambiguous results: signals received from one region will look identical to signals received from another. It is specifically the phase comparison method that suffers the most from potential ambiguities. Increasing the number of receivers will reduce the likelihood of an ambiguous result, but due to noise and measurement errors, it will always remain a factor.

2.3.1 Time Difference of Arrival

The elementary principle behind the TDOA method is to have the receivers in a known configuration, such that the geometry and time information reveals the angle towards the source. An example of an N-antenna configuration is shown in Figure 2.14. If a source is radiating nearby, then we have the geometry problem shown in (a), where the distances d_n to the source need to be known in order to solve for the interior angles. If the source is radiating from sufficiently far away (far field of the receivers), then the geometry can be approximated as in (b): the lines toward the source are assumed to be parallel, and then it is only required to know the antenna separation distances D_n, with the time delay t_d. With these variables known, the AoA (denoted as θ) can be calculated by trigonometry as follows:

$$\cos\theta = \frac{d_1 - d_2}{D_{12}} \qquad \wedge \qquad t_d = \frac{d_1 - d_2}{c},$$

$$\therefore \theta = \cos^{-1}\left(\frac{t_d c}{D_{12}}\right).$$

Stellenbosch University https://scholar.sun.ac.za

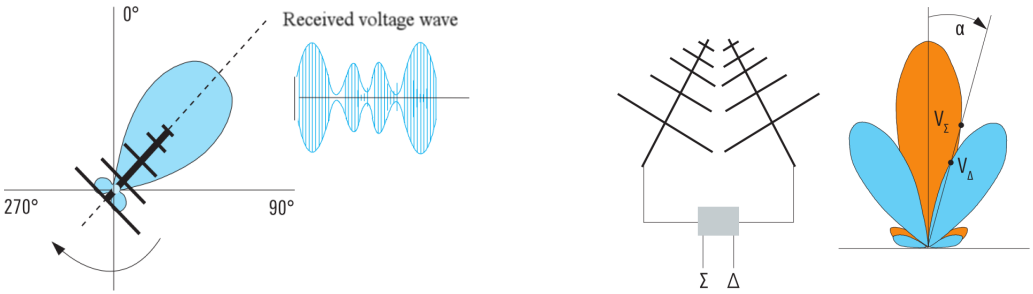

(a) A rotating directional receiver. An example of output is shown over time.

(b) Two receivers in sum-difference configuration. V_Σ and V_Δ indicates the patterns of the sum and difference outputs, respectively.

Figure 2.15: Example of amplitude comparison method. [31, p. 77]

This will yield ambiguous results, which can be alleviated by using additional receivers. Analysis of the multi-antenna TDOA system is available in [32, Ch. 3]

The accuracy of the AoA calculation is dependent on the incoming signal and how accurately the time differences can be measured. This is required to be on the order of hundreds of picoseconds, for receivers less than a meter apart (as light travels 1 metre in $\sim 3.3 \times 10^{-9}$ seconds). The angular resolution is also not only dependent on the system's sampling rate, which needs to be as high as possible, but also on the maximum separation distance, which increases accuracy.

2.3.2 Amplitude Comparison

A classic DF method is to evaluate the received power of a rotating directional antenna. The angle of maximum received power correlates with the approximate bearing of the source. Figure 2.15(a) shows an illustration of this method. A receiver with a narrow beamwidth will offer high sensitivity, as the incoming wave traces out the gain pattern of the antenna. However, using only one antenna will give limited angular detection range: due to the speed of rotation, it is likely for the receiver to overlook sporadic or short-duration signals.

The amplitude comparison technique utilises multiple directional receivers in different orientations to extract angular information from the received power. With two antennas, one can utilise both the sum and the differences of the outputs to effectively create two new radiation patterns, as shown in Figure 2.15(b). The sharp null of the difference pattern, together with the peak of the sum pattern, provides improved angular resolution and accuracy. More antennas can be added as needed to cover a larger field of view, such that mechanical rotation is unnecessary. The most popular application of this form is the Watson-Watt array [32, p. 157].

The major disadvantage of this method is that the directional pattern of an antenna is very sensitive to frequency. Therefore, it would be exceedingly complex to apply an amplitude comparison solution over a broad bandwidth.

Stellenbosch University https://scholar.sun.ac.za

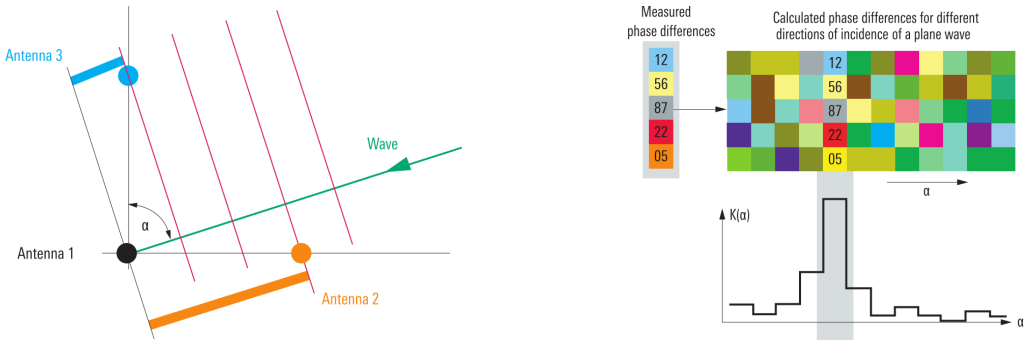

(a) Triangular layout of a three-antenna system with an incoming wavefront from angle α.

(b) Graph shows the correlation of measured phase differences with a dataset of known phase differences at known angles.

Figure 2.16: Example of the phase correlation method. [31, p. 81]

2.3.3 Phase Correlation

The phase correlation method (also referred to as phase interferometry or phase comparison) is similar to TDOA, as it also relies on the delay in propagation times between different receivers. The simple difference is that the phase information is compared, which reveals significantly more properties of the measured signal than the time information, and provides greater ability in isolating signals of interest.

The advantage in angular resolution is clear for antennas that are separated on the order of half the signal wavelength, $\frac{\lambda}{2}$: the phase differences are then large enough (compared to the lower frequencies) to be measured far more accurately than time differences, which give greater measurement variance.

For a $\frac{\lambda}{2}$ separation distance between receivers, the measured phase differences will exist over the full range from $-180°$ to $180°$. Longer signal wavelengths will yield phase differences over a smaller range, whereas shorter wavelengths will go through additional cycles, exceeding the $360°$ range. The latter case is illustrated in Figure 2.16(a): the plane wave lines indicate points of common phase, which overlap with the receivers, resulting in a measured phase difference of zero. This is because measurement of phase in the frequency domain is by definition constrained within $\pm 180°$, and so the additional cycles cannot be resolved so simply. However, the delay information is contained in the antenna layout: a time-domain sample of multiple receivers provides content that is tied to the geometry of the receivers. Therefore, knowledge of the configuration is a critical factor in resolving ambiguous measurements, which would otherwise yield erroneous AoA estimates.

There are two well-known techniques [31, p. 81] to alleviate the phase ambiguity problem. The first option is to utilise a densely filled array of receivers, such that separation distances are $\leq \frac{\lambda}{2}$ between all neighbouring receivers. In this case, the AoA can be estimated trigonometrically, similar to what was discussed for the TDOA method. A detailed trigonometric solution is available in [32, Sec. 3.4.2].

Stellenbosch University https://scholar.sun.ac.za

The alternative option is a sparse array of elements, such that phase differences $>$ 180° are in fact permitted between at least one pair of neighbouring receivers. The ambiguities are then resolved by means of calibrating the system and comparing measurements with a dataset of expected phase differences. The working of this method is represented graphically in Figure 2.16(b).

The correlation function calculates the quadratic error between two sets of data as one is moved over the other. For the phase correlation method, a row of measured phase differences is correlated over a matrix of expected phase differences at known angles. This expected dataset can be generated computationally, or by physically calibrating of the system. The dataset entry that yields a minimum error (or maximum correlation coefficient) compared to the measurement, corresponds with the estimated AoA.

The accuracy of the phase correlation method is dependent on the exact receiver configuration, the frequency of interest, and the noise of the measurement (from the environment, cable effects, and the layout error). The impact of these factors is investigated with MATLAB code presented in Chapter 4, where the goal is to develop a DF algorithm that works accurately over a wide range of frequencies.

2.4 Conclusion

This literature review provides the necessary background for understanding the antenna design process of Chapter 3, and the implementation of the DF algorithm in Chapter 4. It is explained that the desired characteristics for the receivers of the DF system must have an omnidirectional pattern, with high realised gain over a wide impedance bandwidth, such that a variety of interference sources can be detected. Bandwidth enhancement techniques are introduced, as well as the two candidate antennas that are considered. Finally, the workings of three radio DF techniques are discussed, with an outline on the advantage of the phase correlation method. These topics are now addressed with greater focus in the following chapters.

Stellenbosch University https://scholar.sun.ac.za

Chapter 3

Antenna Design, Simulation and Results

"When you see a good move, look for a better one."

—Emanuel Lasker

3.1 Introduction

This chapter presents a detailed overview of the process behind designing a wide-band, omnidirectional antenna for use in RFI direction finding. Two candidate designs are considered: the biconical antenna, and the asymptotic conical dipole. The bicone is simpler to manufacture, but is limited by its impedance bandwidth. Therefore, it is first considered to determine the efficacy of impedance loading as a bandwidth enhancing technique, by means of software simulation. The enhanced bicone is compared with standard ACD designs of varied shapes. The designs are optimised to find the best low frequency response for a small antenna size. The chapter concludes by detailing the manufacturing process for the selected design, and finally provides practical measurement results of the antenna's performance.

3.2 FEKO Simulation

The electromagnetic simulation software FEKO was used to model the considered antenna designs. The software performs full-wave analysis (solving the complete set of Maxwell's equations) to accurately evaluate the EM solutions of arbitrary 3D structures. FEKO was selected instead of CST (an alternative EM simulation tool) due to its extensive material library, and capability of modelling customised dielectrics and resistive sheets. The materials were manually defined to have variable impedance profiles, so as to implement and study the resistive loading and dielectric

Stellenbosch University https://scholar.sun.ac.za

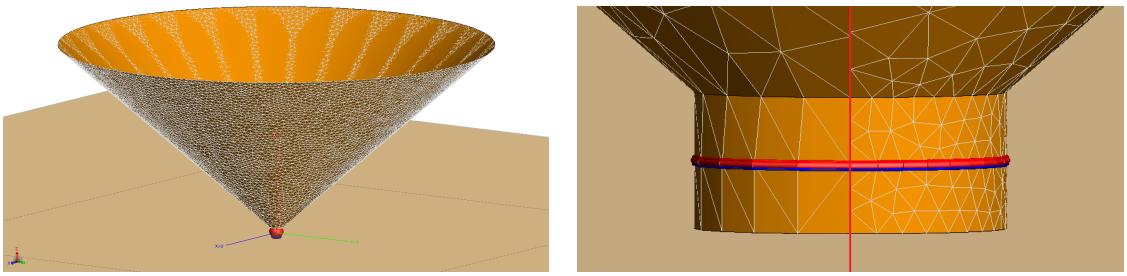

(a) Model of a monocone above a ground plane, with overlaid solution elements (mesh).

(b) Close-up view of the feed region. A coarse mesh (left) contrasted with a finer mesh (right).

Figure 3.1: FEKO model of the 41° monocone.

coating techniques discussed in Section 2.2.2. The simulated performance is then compared to that of the ACD with varied geometry.

3.2.1 Design of an Enhanced Conical Antenna

A monocone above an infinite ground plane gives analogous performance to that of a similar bicone. The difference is that modelling of a bicone is significantly more computationally expensive to solve, due to having double the model size. Therefore, due to the large number of high frequency simulations and optimisations that was performed, the 41° monocone design [24] was selected as a benchmark for the investigation.

The FEKO model of a cone antenna is shown in Figure 3.1(a). The image shows the flat, triangular mesh elements that approximate the curved, metal surface, over which the current and field distributions are computed. The accuracy of the simulation is largely dependent on having a mesh that is sufficiently fine. This is most important at high frequencies, where small details have the largest influence.

The dimensions for the model were determined according to the maximum size that could be manufactured by the available 3D printer. The width was constrained to 24 cm, giving a cone radius of 12 cm, height of 10.4 cm, and side length of 15.9 cm. These dimensions were held constant throughout the following simulations.

Feed region

The first matter of study was the feed region, where the source excites the antenna. By varying the number of local mesh elements at the feed, shown in Figure 3.1(b), it was found that the default meshing is not adequate for an accurate high frequency response. This is because a coarse mesh gives a crude approximation of the curved structure, yielding a false (and optimistic) evaluation of high frequency performance.

The results of the feed region testing are presented in Appendix A.1, as substantiation of this inherent shortcoming of simulation. To alleviate these effects, a local region was defined for the port that is about three times finer than the software

Stellenbosch University https://scholar.sun.ac.za

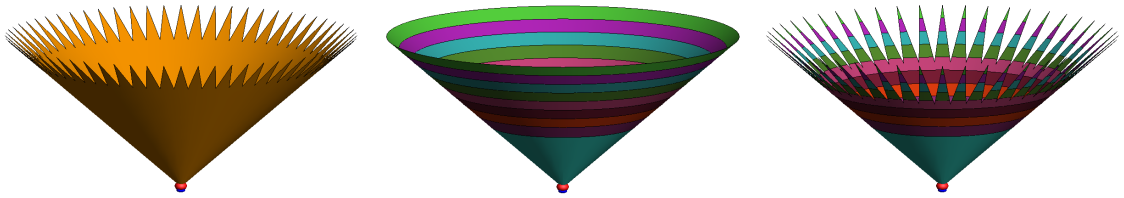

(a) Serrated cone. (b) Discretely loaded cone. (c) Loading with serrations.

Figure 3.2: FEKO models of a cone with added serrations and resistive loading.

default. The adjustment increased the total mesh elements by roughly 2%, which is a negligible trade-off for greater accuracy. This setting was maintained across all simulations for the sake of reliably comparing results.

Serrated edges

A FEKO model was created to simulate how the performance of a monocone is influenced by the addition of serrated edges. The total number of serrations was varied over several cases ($N = 32,\ 48,\ 64,\ 96,\ 128$) with three different sets of serration lengths ($l = 1,\ 2,\ 3$ cm). Figure 3.2(a) shows an example of one of these configurations. These serrations were introduced to the model by projecting a polyline onto the cone surface, with 3D point coordinates calculated by the MATLAB code that is available in Appendix B.1.

The expected result is that serrations will improve the reflection coefficient by reducing the effect of diffraction at the edge. However, this expectation was not met: all of the test cases returned only slight variation around the same result. The simulated reflection coefficients are compared in Appendix A.2. It was postulated that the lack of substantial variation in results is due to the model approximation of metal as a perfect conductor: if the antenna has 100% efficiency, then the additional path length that is travelled by the diffracted currents will not provide any loss. The same amount of energy will therefore return to the source in each of the simulated configurations. Serrations are later applied in combination with resistive loading in order to verify if this may be the case.

Resistive loading

The purposeful addition of resistance to an antenna is a well-known technique to enhance impedance bandwidth, and is briefly introduced in Section 2.2.2. Loading of a wire antenna can be simulated (and physically realised) by the addition of resistive elements at discrete instances along the track. The conical antenna, however, cannot be loaded with lumped elements. The metal surface must instead transition to an absorbing sheet that has some distributed resistance.

EM absorbing sheets are commercially available, and are characterised according to a bulk resistivity (or volume resistance) typically given in units of Ω·cm. This

Stellenbosch University https://scholar.sun.ac.za

Table 3.1: Wu-King loading profile over the side length of a 41° cone.

Length (cm)	0	6	8.4	10	11.6	13	14.3	15.2	15.7
Resistance (Ω)	20	30	40	50	70	100	180	470	1870

is equivalent to the material's sheet resistance multiplied by its film thickness. The sheet resistance is commonly described in units of Ω/square, which is dimensionally equal to an ohm, but is expressed as such to avoid ambiguity.

The Wu-King loading profile is defined in terms of the height and radius of a wire antenna. The MATLAB code of Groch [33, Appendix D.1] was used to compute the relevant profile for a 12 cm radius, 41° cone. This code is made available in Appendix B.2 for the sake of accessibility. The result is the ideal, continuous loading profile, but this is non-trivial to be practically realised. An absorbing sheet would need to be tapered in thickness, becoming thinner towards the end of the cone, which would be a practically complicated and expensive design. One possibility is to manufacture a sheet of graphite-impregnated plastic, where the graphite volume may be controlled over length. The properties of the plastic may also be designed, to create a complete impedance profile.

Alternatively, it is simpler to apply a discrete profile with a number of constant resistance sheets. The performance of this approximation is simulated in FEKO, with varied number of layers. Table 3.1 shows the computed values that are used for a full loading profile. It was found that, when applied over the full length, roughly nine sheets, as in Figure 3.2(b), is ample to capture the form of the profile, but this can be simplified as desired. For instance, five sheets can be applied, starting halfway along the length. These cases are simulated with various loading factors (30–100%) to investigate the effect on efficiency and bandwidth.

On the following page, Figures 3.3 and 3.4 provide the reflection coefficient and realised gain results, respectively, for the different loading factors. It is evident from the S_{11} plot that that the low frequency cut-off is significantly improved by the full loading profile: the −10 dB reflection point is reduced to 260 MHz, compared to 470 MHz of the standard cone. Additionally, it can be seen that there is less variation in reflection coefficient over frequency, which is as a result of the input impedance having a flattened response, as expected.

The trade-off is clear in the realised gain performance, as the efficiency reduces with greater loading. The 30% loading, however, has distinctly similar performance to the metal cone, and so it is clear that an optimal trade-off can be made, depending on the design specifications.

It is interesting to note that the loaded gain is in fact greater between 5.5 GHz and 8 GHz, in all cases, which cannot be due to efficiency being improved. This may be a result of the radiation pattern lobes having slightly shifted to radiate more on the azimuth plane.

Stellenbosch University https://scholar.sun.ac.za

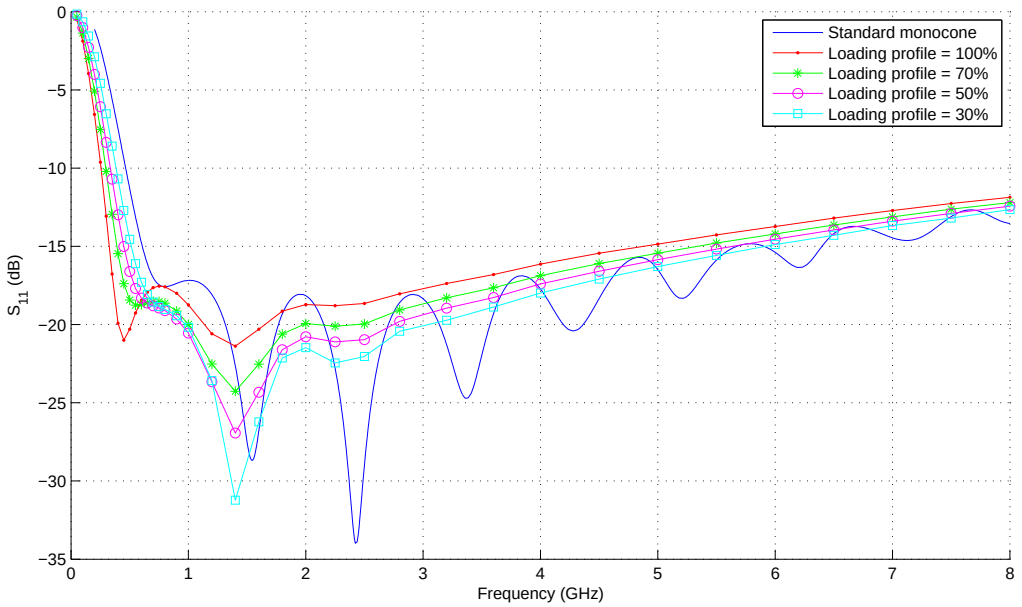

Figure 3.3: Simulated reflection coefficient with varied loading factor. The standard cone has a -10 dB cut-off at 470 MHz, which is improved to 260 MHz by the full loading profile.

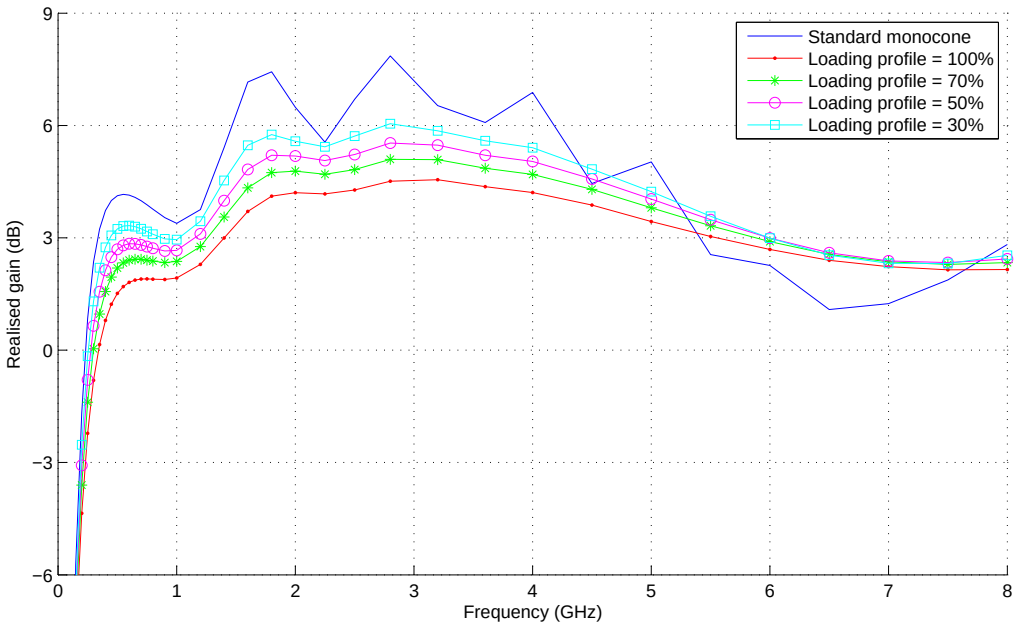

Figure 3.4: Simulated boresight realised gain ($\theta = 90°$) with varied loading factor.

Stellenbosch University https://scholar.sun.ac.za

Resistive loading with serrations

As previously stated, the addition of serrated edges to the top of a monocone did not yield significant simulated improvement. It was postulated that greater influence will be seen with a combination of serrations together with resistive loading. Further simulations were performed to verify if this may be the case.

The reflection coefficient results of the simulation are presented in Appendix A.3. There is again only a slight variation between the different test cases, with no improvement greater than the standard, fully loaded monocone.

The reason that there is again no substantial improvement, may be due to the fact that the added serrations reduce the surface area of the absorbing region, meaning that any potential reduction in reflection as a result of added serrations is negated by the fact that less energy is now absorbed by the resistive sheet. Further simulation is required to yield conclusive results.

Dielectric coating

The simulated effect of adding a dielectric coating to the surface of a cone was briefly studied. The epoxy composites presented in Moon et al. [23, Figure 3] were modelled as dielectrics in FEKO to investigate what could be achieved with different permittivity profiles.

The dielectric region was applied to a monocone in various ways: as a thin coating that was optimised according to thickness; as a tapered coating with decreasing thickness over length; and as a large, filled region on the outside of the cone. Each of these cases tested three different epoxy concentrations. Unfortunately, no positive results could be obtained. The tests with thin or tapered coatings did not yield any bandwidth improvement, most likely due to the large skin depth required for the coating to influence low frequency signals. However, for the tests with a thick dielectric region, a large part of the band (between 500 MHz and 1 GHz) would suffer extreme decreases in efficiency, due to the loss. The results made it clear that significant analysis would be required to find an appropriate design.

Remarks

The application of a full, resistive loading profile to a cone antenna proved to give the best simulated performance that could be obtained by varying the material properties with a fixed geometry. This can only be practically realised with the acquisition of suitable materials. Therefore, the availability and cost of dielectrics and absorbing sheets needs to be factored in to assessing the suitability of these enhancement techniques. A practical configuration will be with graphite-impregnated epoxies that have carefully designed properties, which may be used to achieve an optimal impedance profile. However, this exists beyond the scope of this project, and is left for future investigation.

Stellenbosch University https://scholar.sun.ac.za

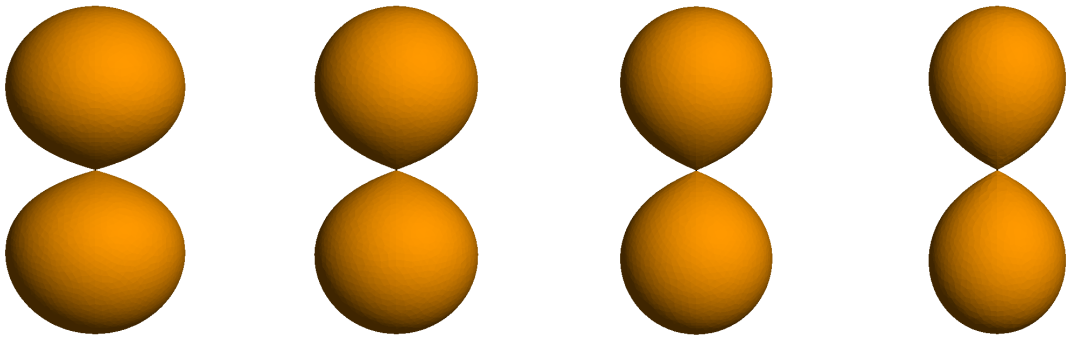

(a) $Z = 40$ (b) $Z = 50$ (c) $Z = 58.1$ (d) $Z = 70$

Figure 3.5: FEKO models of the ACD with fixed height and varying impedance.

3.2.2 Design of an Asymptotic Conical Dipole

The ACD is a surface that is defined according to an analytical curve revolved around its centre axis. FEKO features the functionality to model mathematically defined structures, and this was utilised to simulate the different models shown in Figure 3.5. These structures were generated according to the equations that are presented in Section 2.2.4. The curves are defined for impedance values of $Z = 40,\ 50,\ 58.1$, and $70\ \Omega$. The $58.1\ \Omega$ value is not arbitrary – this was computed to give a $41°$ angle at the feed of the antenna, to investigate if the results obtained by Wiid [24] may provide corresponding improvement for an ACD.

The input impedance over frequency is investigated for each of these curves, to see how the selected, design impedance correlates with the simulation values. The results of the input resistance and reactance are plotted on the following page, in Figure 3.6. Each of the resistance responses reach peak values that are slightly below their designed impedance magnitude. The reactance values all settle close to $0\ \Omega$, which corresponds to the desired condition for which Schelkunoff and Friis [26] first conceived of the design. It is important to bear in mind that these results are computed with the parameter $n = 2.5$ in Eq. 2.21, as suggested by Jacobs et al. [29]

The resistance of the $70\ \Omega$ design appears to oscillate around $60\ \Omega$, while the $58.1\ \Omega$ does the same at $50\ \Omega$. Therefore, the results suggest that the $41°$ ACD design will be best matched to a $50\ \Omega$ system. It is also interesting to note that the input impedance has a very flat variation over frequency, which is the same result that resistive loading accomplishes.

It was, however, observed that the simulated feed distance was different for each of these tests: due to the port being held to constant radius, and the apex angle becoming more obtuse with greater impedance, the corresponding feed length had to become longer to connect the spheres. Therefore, additional simulations were performed to investigate how much of the variation of Z_{in} was a result of the feed. Results are provided in Figure 3.7, which show that the length of the feed gap

Stellenbosch University https://scholar.sun.ac.za

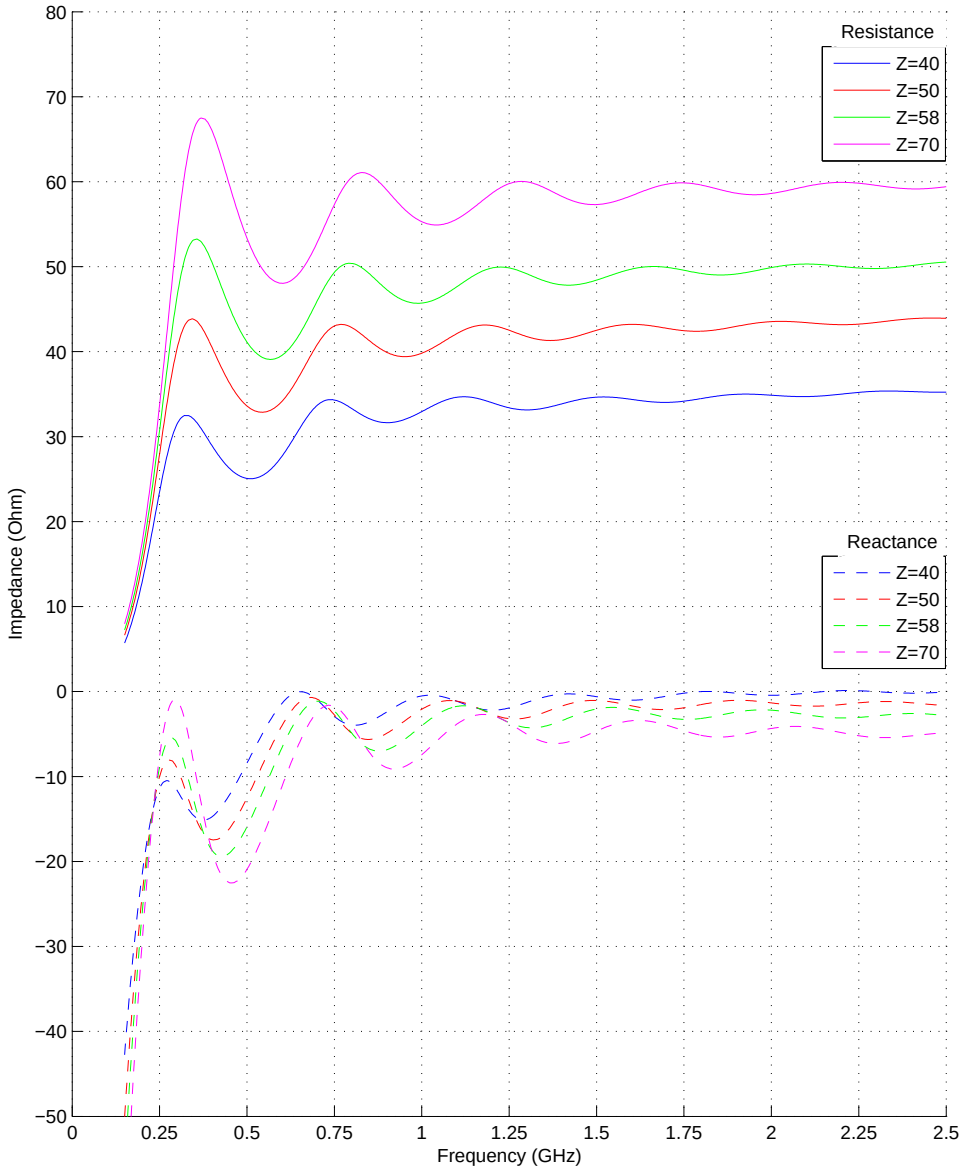

Figure 3.6: Simulated input impedance of ACD with varied curves, for fixed height $h = 22\ cm$ (total antenna length of 44 cm).

Stellenbosch University https://scholar.sun.ac.za

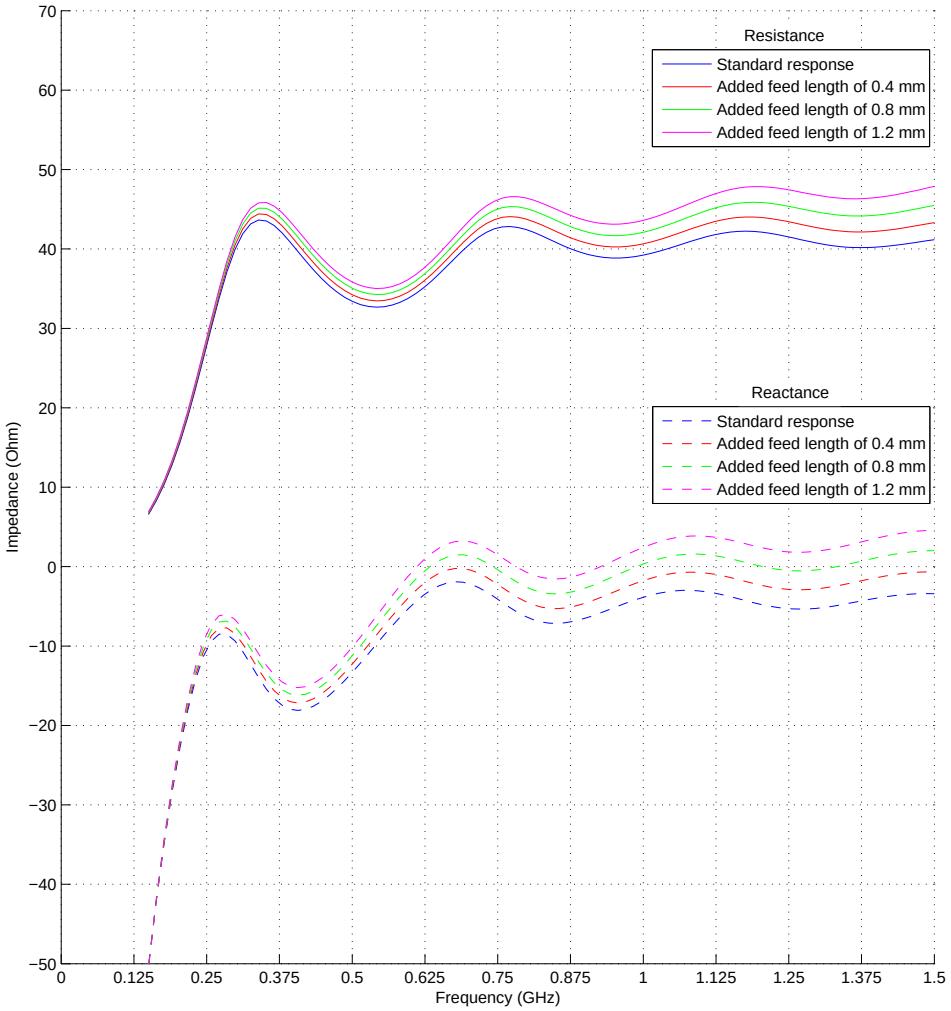

Figure 3.7: Simulated input impedance of ACD, $Z = 50\ \Omega$, with varied feed gap lengths. $h = 22\ cm$. It is clear that input resistance and reactance increases very sensitively with the feed gap length.

Stellenbosch University https://scholar.sun.ac.za

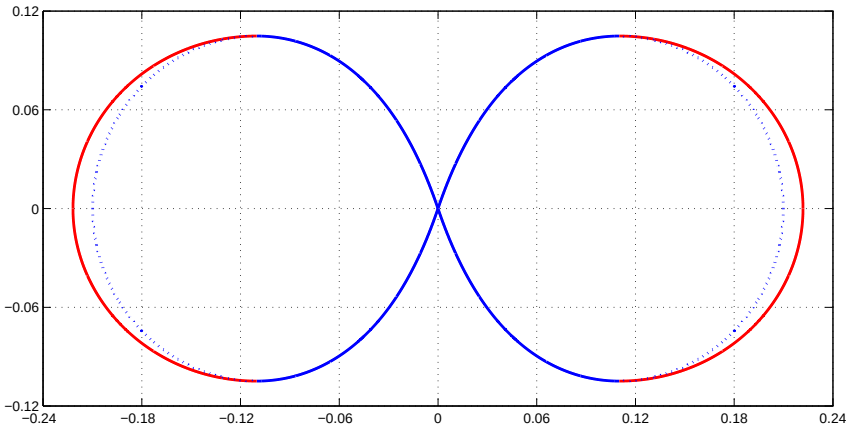

Figure 3.8: Combined curve design of the ACD, plotted in Cartesian coordinates.

is an incredibly sensitive parameter. This corresponds with the results obtained by Wiid in [24]: a longer feed gap causes an increase in antenna inductance and resistance. This means that the simulated Z_{in} of the higher impedance curves are indeed further increased by the fact that their feed lengths are longer.

Wideband simulations revealed that a 50 Ω ACD can be significantly improved by extending the length of the feed gap. This has the effect of increasing input resistance past 50 Ω, after which it begins dropping off at higher frequencies. This is an improvement over the standard 58.1 Ω design, which maintains a 50 Ω input resistance, but begins falling off sooner.

Combined curves

The simulated input impedances showed that the 70 Ω curve gave better performance at lower frequencies, whereas a feed-adjusted 50 Ω curve had improved performance at high frequencies. It was considered that the form of these two curves can be combined, by taking the bottom half of the 50 Ω curve, and adding a 70 Ω curve to the top half (illustrated in Figure 3.8), so as to extend the total length and obtain an enhanced low-frequency cut-off. This was investigated in FEKO by scaling and translating the 70 Ω curve to connect seamlessly with the bottom curve. MATLAB code (available in Appendix B.3) was created to find the necessary scaling factors and Cartesian translations required for the transition to be continuous.

Simulation results at the time showed that the low-frequency performance was apparently improved with the extended top, over the plain 50 Ω design, but subsequent analysis with a normalised feed gap show that the effect of the alteration is in fact minimal. Due to time-constraints, it was necessary for a final design to be selected for manufacturing, and hence the 50 and 70 Ω combined curve design was chosen. However, further investigation is indeed required to find an even more optimal design.

Stellenbosch University https://scholar.sun.ac.za

3.3 Manufacturing the ACD Antennas

The combined curve ACD design was selected for the final testing of the DF application. The manufacturing process entailed that the design be translated to a 3D-printable model. Due to the size of the structure, a hollow-shell design was necessary to minimise printing time, as well as the cost and weight of the plastic used. This was implemented as two separate shells such that they can be connected into one "sphere". The printed structures were coated in aluminium tape, and the centre feed connections introduced to connect the spheres into a dipole. A polystyrene support structure was finally manufactured so that the dipoles can be mounted and transported without damaging the thin centre feed.

3.3.1 3D Printed Design

The 3D model was created with computer-aided design software, Autodesk Inventor. A hollow sphere was designed by creating two sets of the desired analytical curves, one of them scaled and translated, in order to form the inside of a 3 mm shell. A cross-sectional view of the model is provided in Figure 3.9.

The design was made with the intention of printing the same sphere for both the top and bottom parts of the dipole. For this purpose, a reference hole was added to the top hemisphere design, such that – if it were the bottom part of the dipole – it serves as a path for the cable to feed through; or, if it were the top part of the dipole, a metal rod can be threaded through to strengthen the structure. Similarly, the bottom hemisphere has a region to fit the metal feed, which was designed according to the dimensions of aluminium blocks that were available.

The connecting region was designed iteratively, so that the two hemispheres can interlock with a smooth transition. The old and new designs are contrasted in Appendix C.1. The first iteration resulted in additional effort for the hemispheres to interlock, because the space was unevenly filled with plastic residue. For the remaining prints, the connection was adjusted to allow more room for these minute printing errors. This was determined before final production by printing only the connecting region itself, so as to reiterate the design without printing a full structure.

The 3D printer was tested with an overhang model (or, unsupported angle tester) to verify the slopes that can be printed without support. It was found that angles above 60° resulted in an inconsistent, uneven surface. Therefore, support structures at 55° angles were introduced to the schematic, such that the extruder had a bridge over which to print the acute angles. The settings of the printer were also adjusted to obtain a high quality, smooth surface. There were, however, some rough features that needed to be sanded smooth, as shown by the photos in Appendix C.2. Further information about the 3D printer, as well as details on the settings used, is available in Appendix C.3.

Stellenbosch University https://scholar.sun.ac.za

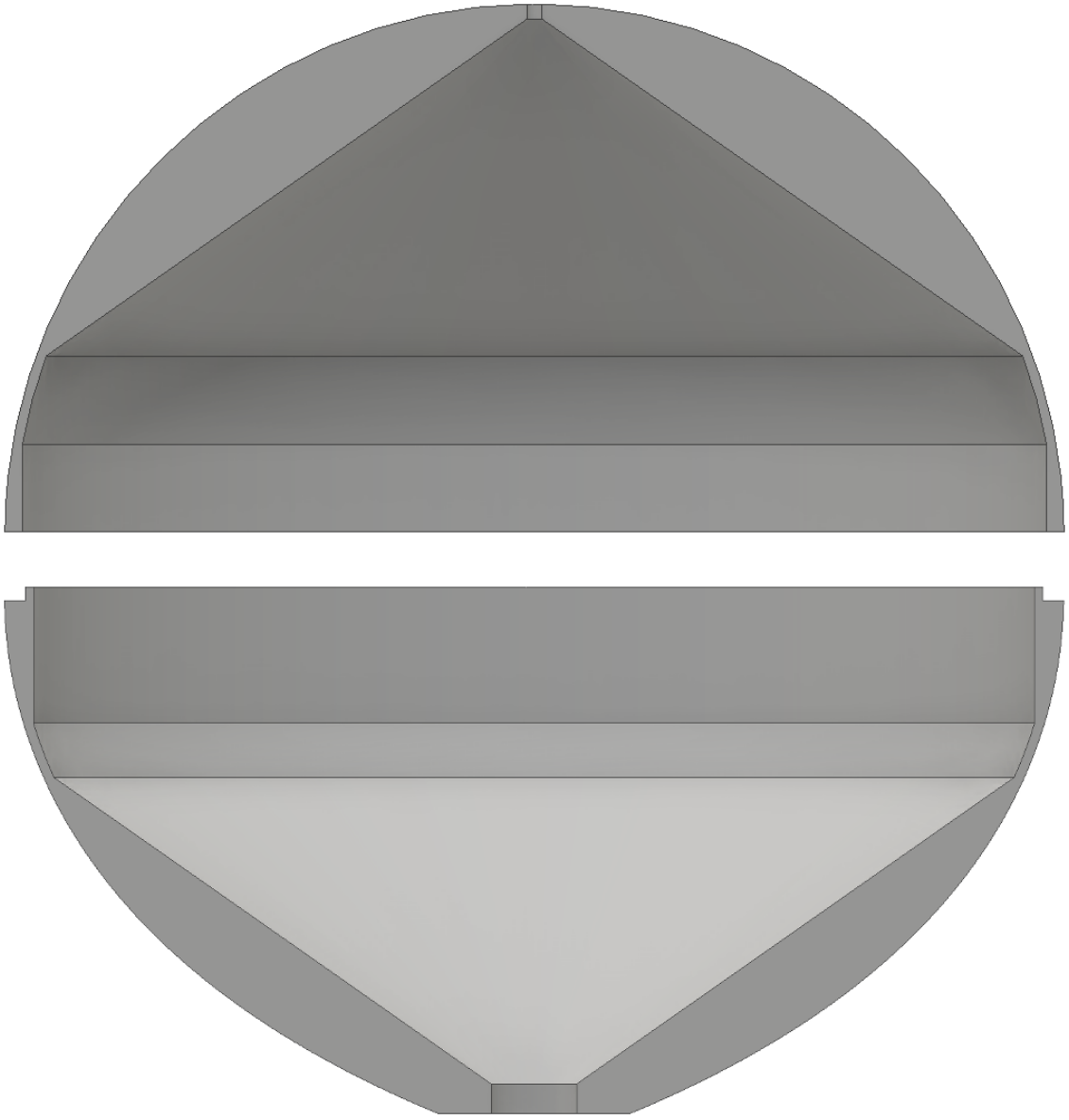

Figure 3.9: Cross-sectional view of the top and bottom half of the final 3D model.

Stellenbosch University https://scholar.sun.ac.za

(a) Aluminium tape applied in strips over the plastic sphere.

(b) Completed ACD after fully coated spheres are connected at the feed.

Figure 3.10: Coating the plastic spheres in aluminium tape.

3.3.2 Manufacturing Process

The antennas were manufactured in two batches: first, one antenna was made for the process to be understood, and for its performance to be verified with measurement; following this, three additional antennas were manufactured together. In the end, the same process was applied throughout: the printed hemispheres were connected together with an epoxy adhesive; the surface and transition region was sanded smooth; and an aluminium tape coating was applied in strips, as shown in Figure 3.10. The tape was cut into a shape with narrow to wide ends, to optimally cover the total surface area and minimise the amount of folds and creases on the coating. The tape transitions over the aluminium port, a region that was designed with a screw that attaches the top sphere to the centre wire. This can be loosened to allow the feed gap length to be tuned as desired. A schematic for this port, with photos, is available in Appendix C.4.

Due to the thin, centre wire being a mechanically weak point of the ACD, it was necessary to design a support structure that maintains the dipole in an upright form. The support is made of an insulating material, similar to polystyrene, called IsoBoard. It is a light-weight, rigid material, which was designed with three columns to hold the dipole in place. A diagram of the structure design is available in Appendix C.5.

The final ACD has a height of 44 cm, and a diameter of 22 cm. The manufactured result is imaged on the following page in Figure 3.11.

3.4 ACD Measurement Results

The performance of the first antenna was verified before additional units were manufactured. The S_{11} was measured on a vector network analyser (VNA), the Agilent

Stellenbosch University https://scholar.sun.ac.za

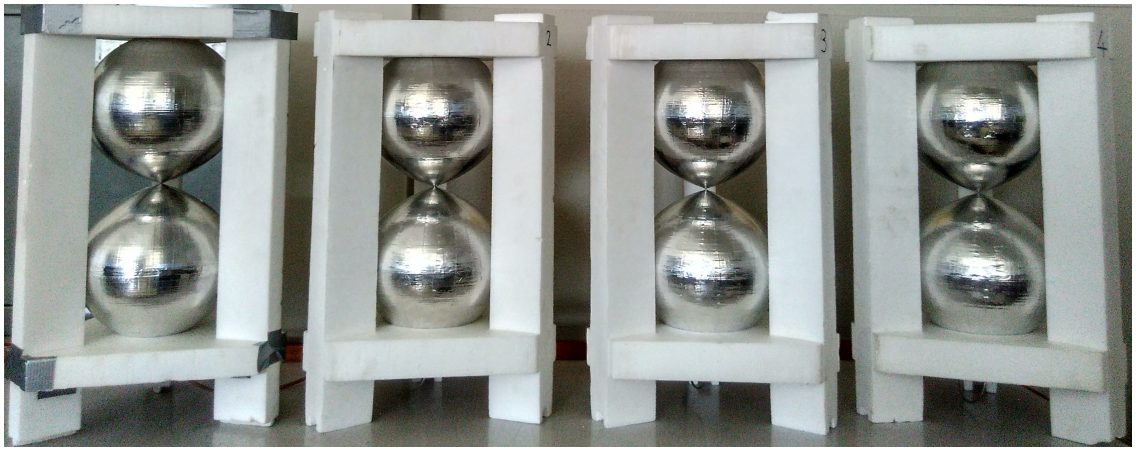

Figure 3.11: Photo of the four manufactured ACD antennas.

N5242A PNA-X, up to 26.5 GHz. The result is plotted against the simulation results in Figure 3.12, which matches up well at low frequencies, corresponding with the expected −10 dB point at 270 MHz. For the simulation at higher frequencies, the MLFMM solver of FEKO was used as a simplified method due to the excessive number of mesh elements ($\sim$ 330 000 at 20 GHz). This simplification, together with the fact that the feed gap was tuned for the physical antenna, and does not match exactly with the simulated model, may explain the 8 dB discrepancy between the results at 20 GHz. The ringing effect is primarily due to room reflections, but a factor of this measurement error may be contributed by the creases and folds in the aluminium tape at the transition from the feed. This is also observed in the reflection coefficient measurements for the other three ACD units, compared in Appendix C.6.

A secondary S_{11} measurement was performed on the Agilent 8510C VNA up to 50 GHz, in order to find the upper cut-off of the impedance bandwidth. The cables that were used for the manufacturing of the antennas are rated up to 33 GHz, and the result in Appendix C.7 shows that the performance of the ACD exceeds this cable limit. This means that the measured impedance bandwidth is well in excess of 100:1, and can only be concluded decisively by replacing the cable with one of a higher frequency rating.

Additional measurements were performed for the gain of the ACD. It was not possible to conduct a full radiation pattern measurement, as the structure could not be mechanically supported to undergo rotation. Nevertheless, the azimuth gain could indeed be evaluated with the Friis equation (Eq. 2.14) from a three-antenna measurement performed in the anechoic chamber of the Houwteq EMC facility. The result is shown in Figure 3.13, and matches up very well with simulation. The noisy effect below 300 MHz is a result of low frequency chamber reflections. From this measurement, a downside of this antenna can be seen at the 800 MHz region, as the gain falls below −3 dB. This comes as a trade-off for the exceptional bandwidth.

Stellenbosch University https://scholar.sun.ac.za

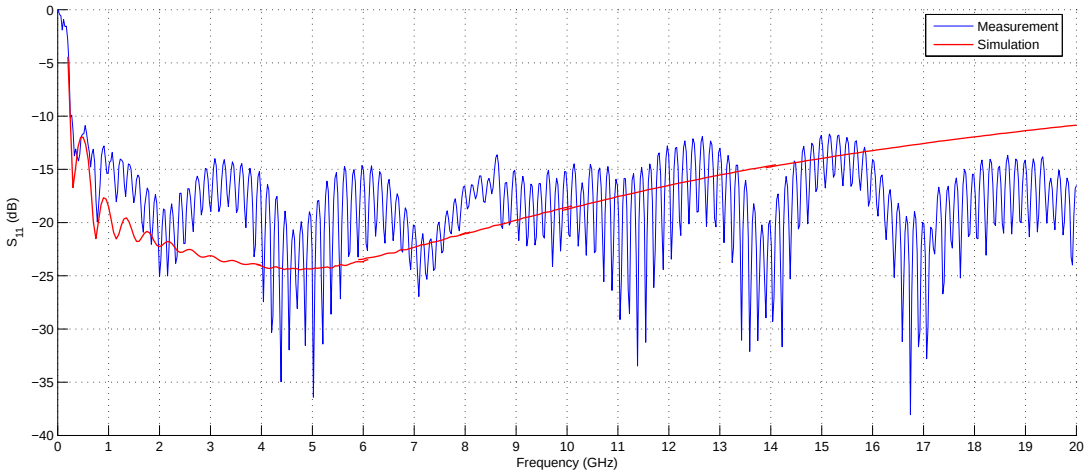

Figure 3.12: Measured reflection coefficient of the final manufactured ACD, compared to simulation. There exists a fair correlation between the two up to 2GHz, whereafter the measurement only intermittently overlaps with simulation. The ringing effect is a measurement error due to room reflections. The low-frequency -10 dB cut-off occurs at 270 MHz.

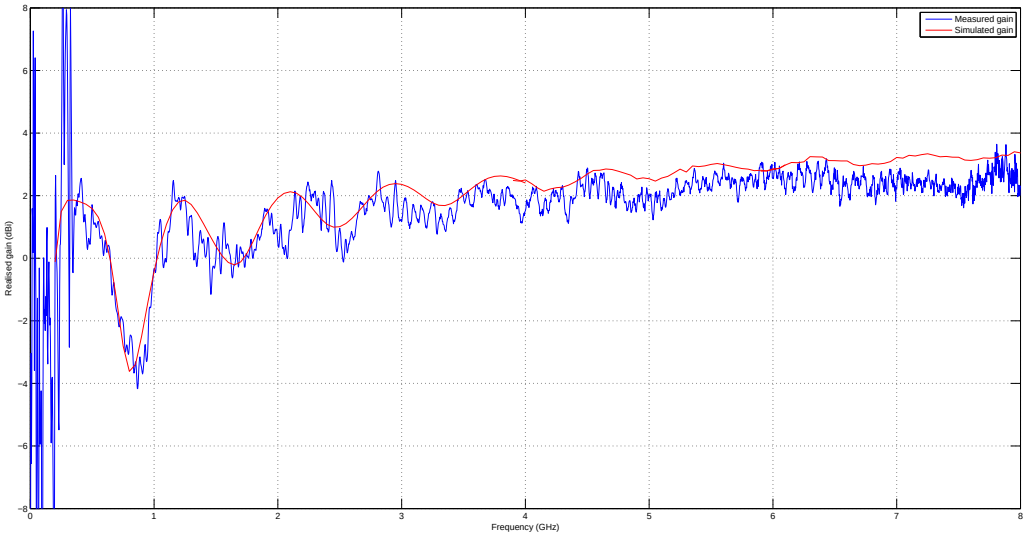

Figure 3.13: Measured realised gain on the azimuth of the manufactured ACD, compared to simulation. The low-frequency measurement error is due to chamber reflections.

Stellenbosch University https://scholar.sun.ac.za

3.5 Conclusion

This chapter covers the process of designing a wideband, omnidirectional antenna. An enhanced conical antenna design was considered, and evaluated alongside the simulated performance of the asymptotic conical dipole. The final design consists of the combination of two ACD curves to obtain an extended total length, to yield a theoretical improvement to the low frequency bandwidth. Four units of this design is manufactured with a 3D printed plastic method to yield a measured impedance bandwidth that exceeds 100:1. This serves as the receiver component for the DF system, and is applied in the field measurement conducted in Chapter 5.

Stellenbosch University https://scholar.sun.ac.za

Chapter 4

Direction Finding Algorithm

"I do not think that the wireless waves I have discovered will have any practical application."

—Heinrich Rudolf Hertz

4.1 Introduction

A phase correlation algorithm was implemented in MATLAB code to simulate the DF performance of an arbitrary antenna configuration at different frequencies. The algorithm utilises a minimum root-mean-square error method to correlate a noisy phase difference measurement over a dataset of expected phases differences from known source angles. The code is developed to be fully modular: results can be obtained for N antennas in an arbitrary layout, over any number of frequency points, to any degree of angular resolution. The signal-to-noise ratio of the phase measurement can also be adjusted as desired to evaluate and quantify the noise sensitivity of one configuration compared to another. The complete MATLAB code is available in Appendix B.4.

This chapter serves to discuss the functionality of the algorithm, followed by a presentation of the output results that quantify the angular resolution and error resistance of different configurations. These results are later verified by the field measurements performed in Chapter 5.

4.2 Algorithm Overview

The working of the phase correlation method is discussed in Section 2.3.3. The goal is to estimate the AoA of a source by comparing a measurement vector over a dataset of computed phase differences for known source angles. Therefore, the outcome for the algorithm is to generate the dataset of expected phase differences, for any given

Stellenbosch University https://scholar.sun.ac.za

array configuration. This dataset is the primary result of the algorithm, as it serves to be correlated with actual measurements and obtain an estimated AoA. However, the code that is presented goes further by testing the performance of that particular layout of antennas, by simulating the accuracy of the AoA estimation under noisy conditions. In this way, it is proven that a symmetrical antenna configuration is inherently prone to giving ambiguous results for higher frequency signals, and that the noise resistance and band of operation can be significantly improved if the placement of the antennas is varied. Therefore, the code serves as a correlation algorithm, as well as a design tool, for testing and finding an optimal layout.

Due to the reconfigurability of the code, it is deemed necessary to provide a brief discussion on its inner workings, such that it may be reused as desired. The remainder of this section serves to expand on the functionality of the algorithm, and is followed by the results.

4.2.1 Antenna Layout

There are several initial conditions that define the operation of the algorithm. The most important parameters are as follows:

- N – The number of receivers in the configuration (used to calculate the coordinates for a symmetrical antenna layout);
- N_r – Defines the number of radial points over which to compute;
- f_L – Lowest frequency point of interest (determines the antenna separation distance for the automatically generated layout);
- f_H – Highest frequency point of interest;
- N_f – Defines the number of points to evaluate between f_L and f_H.

The above parameters define all that is necessary for the code to generate an automatic layout of N antennas, and to compute the expected phase differences for a source at N_r radial points, evaluated at N_f frequencies.

The default antenna configuration is symmetrically spaced, with a maximum separation distance of half the wavelength of f_L. This is the standard design layout for operation at only one frequency point. An alternative layout can also be generated, which pseudorandomly varies the original position of the receivers by around half the wavelength of f_H. The pseudorandom technique is only to force the layout to have a set of separation distances with unique values, such that more information is available to the system. As a result, it is expected for the additional variation to improve the bandwidth of operation, by reducing ambiguous AoA estimates at higher frequencies. This is implemented with a binary variable that switches been which layout is activated, but the code will accept any set of desired antenna coordinates. The output of the two layouts is contrasted in Figure 4.1, with separation distances shown.

Stellenbosch University https://scholar.sun.ac.za

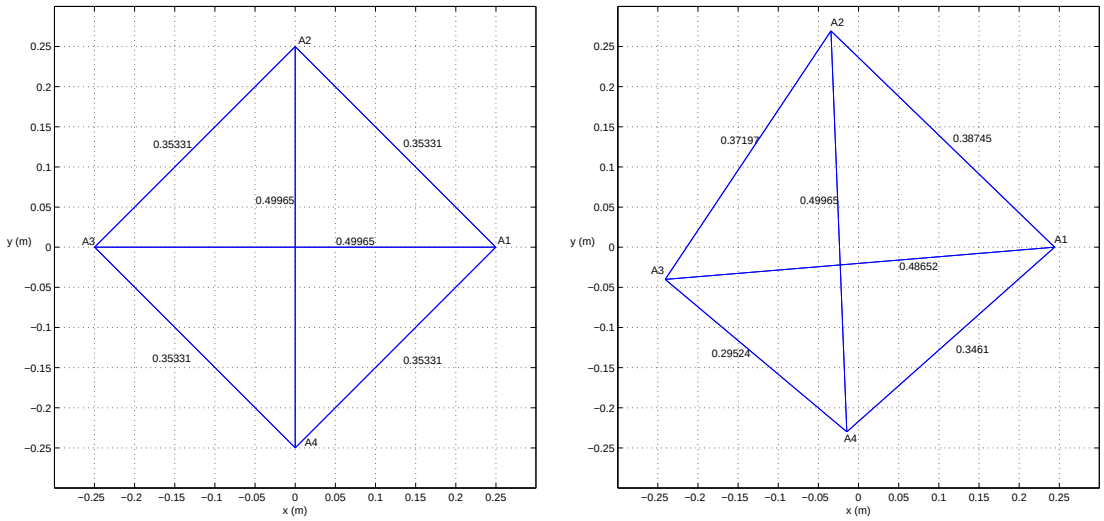

(a) Symmetrical layout.

(b) Layout with varied spacing.

Figure 4.1: Generated 4-antenna layouts for $f_L = 300$ MHz and $f_H = 1$ GHz.

4.2.2 Computing the Expected Phase Difference Dataset

Consider a source that is positioned at $\theta = 0°$ (the far right hand side of the x-axis) for the symmetrical layout in Figure 4.1(a). The incoming planar wavefront will be in line with antennas A_2 and A_4, resulting in a phase difference of 0° between them. As the source rotates around to a position at $\theta = 90°$ (lying above on the y-axis), the distance of the wavefront between antennas A_2 and A_4 is now maximal. It is clear that the measured phase differences are proportional to these wavefront separation distances after scaling to signal wavelength. Therefore, to obtain a dataset solution for any configuration, we must define the wavefront distances for any source angle θ in terms of the antenna coordinates.

A general way of expressing the difference in wavefront distance between two antennas is to take the line between receivers and to project its length onto the axis of the incoming source angle. This is equivalent to rotating the distance vector separating the antennas by an angle θ, and projecting the line onto the x-axis. This must be computed for each permutation of the different antennas, leading to a set of $\frac{N}{2}(N-1)$ phase differences.

The algorithm computes the wavefront distances (in metres) between antennas for a source placed at N_r points over the 360° range. These wavefront distances are then translated to a set of phase differences between each receiver by scaling according to the wavelength. We therefore have a total of N_f datasets (for each desired frequency point) that is now ready to use for correlation.

Stellenbosch University https://scholar.sun.ac.za

Table 4.1: Standard deviation of the phase error for corresponding SNR values.

SNR (dB)	Phase noise standard deviation
60	0.1°
46	0.5°
40	1°
34	2°
26	5°
20	10°
14	20°
10	33°
6	52°
0	104°

4.2.3 Correlation with a Noisy Measurement

The phase correlation function computes the difference (error) between a measured set of phase differences, and all the entries of the expected phase difference dataset. The entry that provides a minimum error (maximum correlation) with the measurement, corresponds with the estimated AoA.

The function is implemented with a root-mean-square error (RMSE) method to find the correlation coefficient of a given measurement over the dataset. The performance of this method was studied by evaluating the AoA estimation error at various signal-to-noise ratios (SNR). This was accomplished by extracting the phase difference entries individually, adding random noise with different variance levels, and correlating this noisy vector with the original dataset. The difference in actual and estimated AoA is then evaluated over the full 360° field of view, to quantify the angular resolution and error sensitivity of the specified antenna layout.

It is first necessary to define the phase noise in a measure of SNR. Our desired *signal* is a uniformly distributed phase measurement across a 360° range. The corresponding signal power (variance, σ^2), in degrees, is mathematically defined:

$$\sigma^2_{\text{signal}} = \frac{1}{12}(360)^2 = 10\,800. \tag{4.1}$$

The phase noise standard deviation (σ) is then calculated from the SNR definition:

$$\text{SNR} = \frac{\sigma^2_{\text{signal}}}{\sigma^2_{\text{noise}}}, \qquad \therefore\ \sigma_{\text{noise}} = \sqrt{\frac{10\,800}{\text{SNR}}}. \tag{4.2}$$

Phase deviations are computed for corresponding SNR values, and arranged in Table 4.1. It can reasonably be expected for real system measurements to have phase errors between 2–10°, and so initial testing used a SNR of 20–34 dB.

Stellenbosch University https://scholar.sun.ac.za

With the phase noise defined, the accuracy of the RMSE method can be evaluated at different noise levels. For a given antenna layout, the AoA estimation errors can be calculated over a range of SNR values, in order to find the cut-off noise levels that can be tolerated over the desired band of operation.

4.3 Angle of Arrival Estimation Results

The 4-antenna layouts shown in Figure 4.1, with symmetrical and asymmetrical placement, were used as test cases to calculate the AoA estimation errors over frequency, and to compare the noise resistance of the two configurations. A compilation of AoA estimate results is provided on the following pages, in Figures 4.2, 4.3, and 4.4, for SNR levels of 34 dB, 26 dB, and 20 dB, respectively. The plotted estimate errors are evaluated at 300 MHz, 650 MHz, and 1 GHz.

From the 300 MHz case in Figure 4.2(a), it can be seen that the estimate is accurate within $\pm 1°$, which worsens to $\pm 2°$ for an SNR of 26 dB. The error estimate increases further to $\pm 5°$ for an SNR of 20 dB, which is fairly accurate, considering that this represents a phase noise with standard deviation of $10°$.

It is evident from Figures 4.2(b-c) that the high frequency performance of the symmetrical layout is prone to giving large errors at source angles around the axes of the setup. For an SNR of 34 dB, however, these errors are in fact very sparse, because the results shown were computed over an angular distribution with arc minute increments (1/60th of a degree). Taking this into account, the total amount of angular points that give large errors is approximately 1.5–2.5%, for the 34 dB cases at 650 MHz and 1 GHz. To emphasise this, the proportion of errors greater than $45°$ is computed over SNR, and provided in Appendix D.1. From these results it is clear that the asymmetrical configuration gives remarkable improvement over the even layout. Results at 20 dB SNR in Figure 4.4 show that the varied spacing provides great resistance to ambiguity errors, but does indeed remain a problem at such noise levels.

The performance of an antenna configuration can be summarised by averaging the AoA estimation errors over all angles, and computing the result over frequency and SNR. Plots of these average errors are provided for the symmetrical and asymmetrical configurations in Figure 4.5. These plots may not directly show the prevalence of ambiguities, but provide a clear indication of the SNR levels that are required to operate over a desired frequency range. For instance, the colour map for the asymmetrical layout in Figure 4.5(b) shows that an SNR of 30 dB is adequate to guarantee an accurate angular resolution over a very high frequency range, whereas the symmetrical layout begins to encounter prevalent ambiguity errors beyond 600 MHz. Nevertheless, in order to operate at high frequencies, it is critical that the actual, physical antenna layout matches very accurately with the specified placement (for which the expected dataset is constructed), because a small variation will lead to large phase errors.

Stellenbosch University https://scholar.sun.ac.za

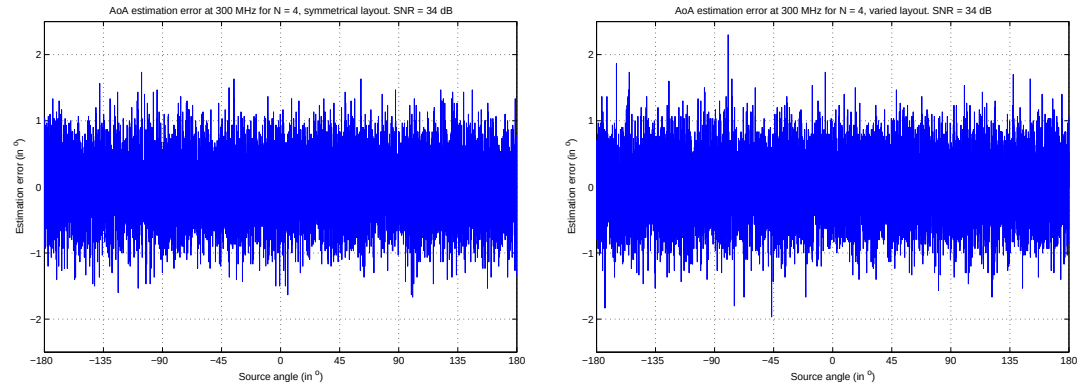

(a) $f = 300$ MHz

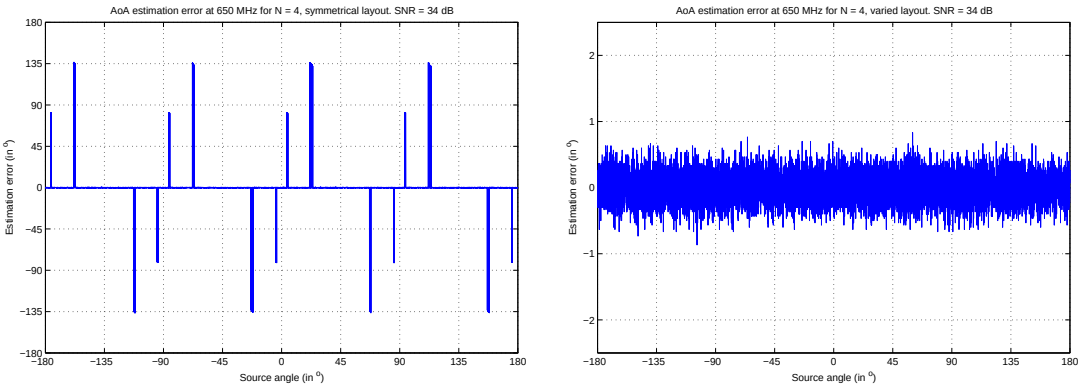

(b) $f = 650$ MHz

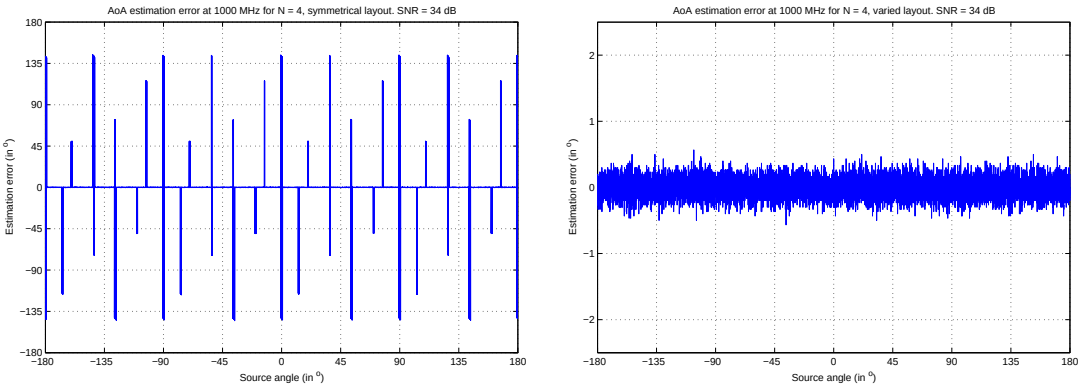

(c) $f = 1000$ MHz

Figure 4.2: AoA estimation errors for a 4-antenna symmetrical layout (left), compared with that of an asymmetrical layout (right), evaluated at different frequencies, for a SNR = 34 dB (phase noise with standard deviation of 2°). Ambiguity errors occur at fine angles around the axes of the symmetrical setup. The asymmetrical layout maintains high accuracy beyond 1 GHz.

Stellenbosch University https://scholar.sun.ac.za

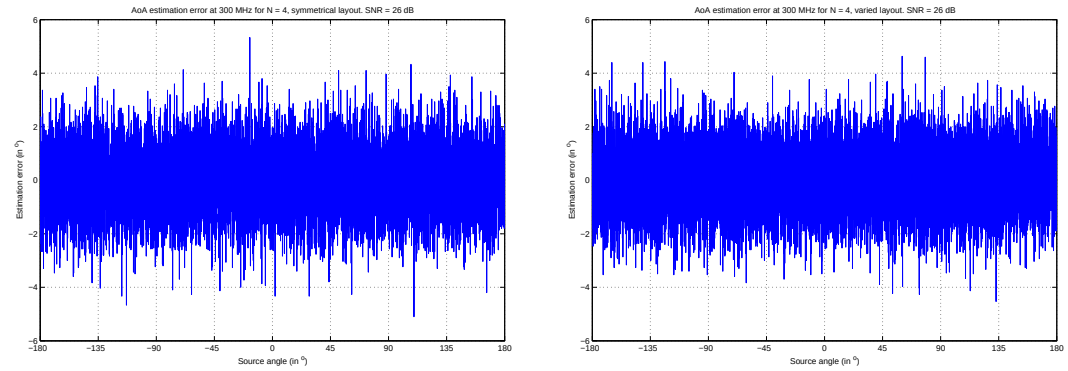

(a) $f = 300$ MHz

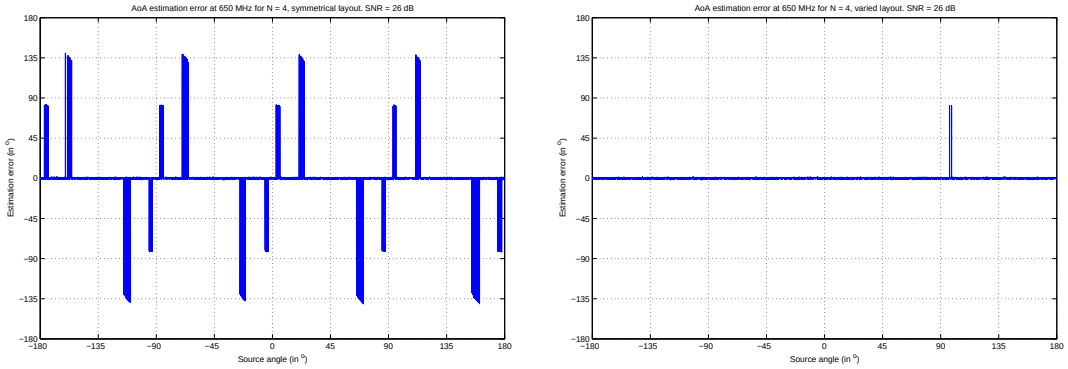

(b) $f = 650$ MHz

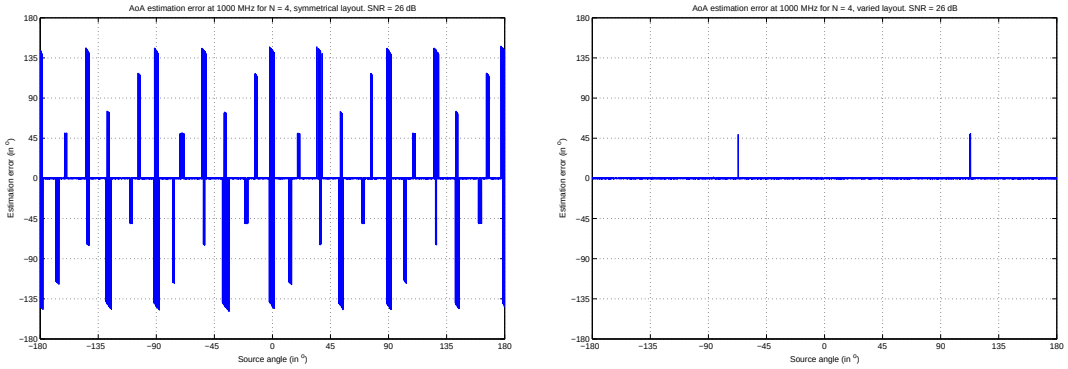

(c) $f = 1000$ MHz

Figure 4.3: AoA estimation errors for a 4-antenna symmetrical layout (left), compared with that of an asymmetrical layout (right), evaluated at different frequencies, for a SNR = 26 dB (phase noise with standard deviation of 5°). At greater noise levels, the fine ambiguous regions around the axes of the even layout begin to spread out over the field of view. The asymmetrical layout has sparse regions of ambiguity that begin to occur, yet accuracy remains well within 2° for the rest of the field of view.

Stellenbosch University https://scholar.sun.ac.za

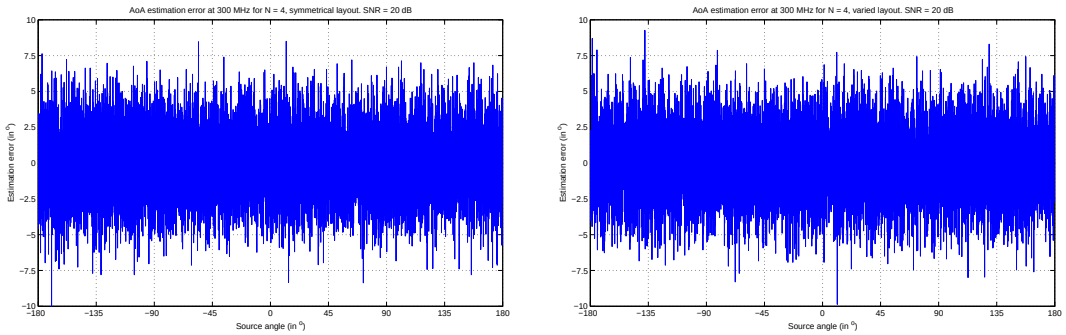

(a) $f = 300$ MHz

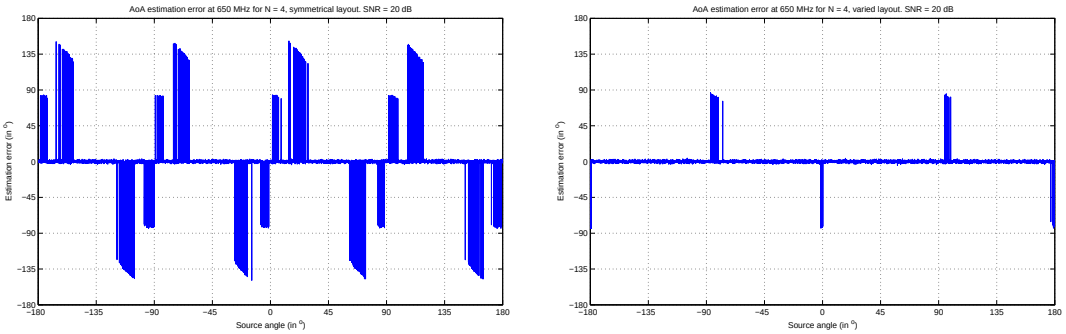

(b) $f = 650$ MHz

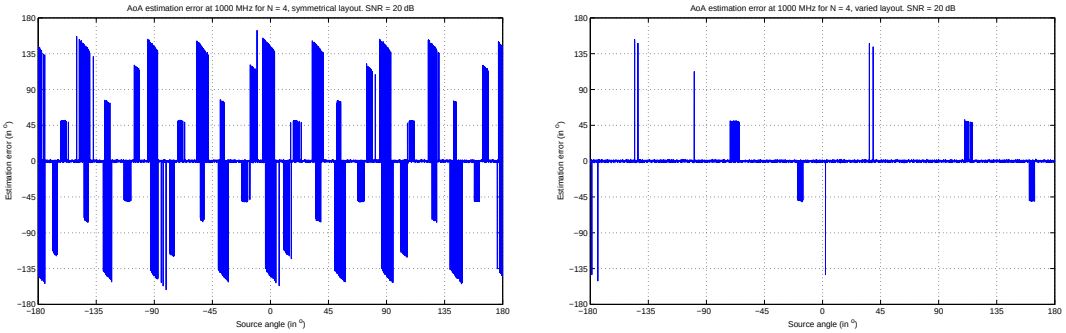

(c) $f = 1000$ MHz

Figure 4.4: AoA estimation errors for a 4-antenna symmetrical layout (left), compared with that of an asymmetrical layout (right), evaluated at different frequencies, for a SNR = 20 dB (phase noise with standard deviation of 10°). Angular resolution at 300 MHz now lies within ±5°. High frequency ambiguity errors become significant for the asymmetrical layout.

Stellenbosch University https://scholar.sun.ac.za

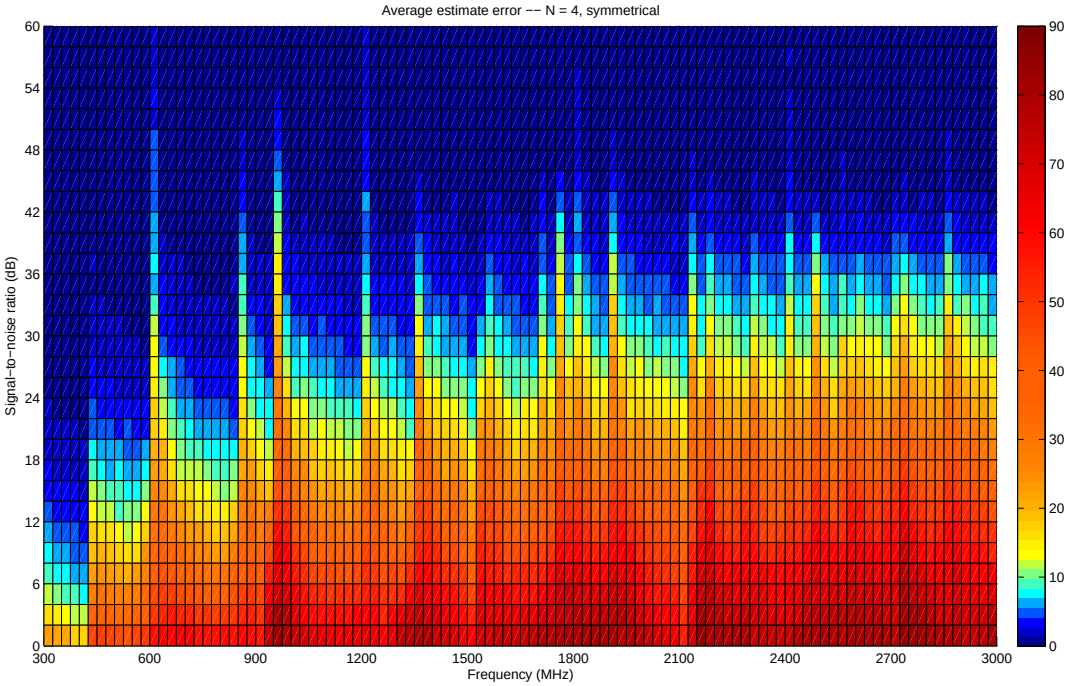

(a) Average estimation error for the symmetrical layout.

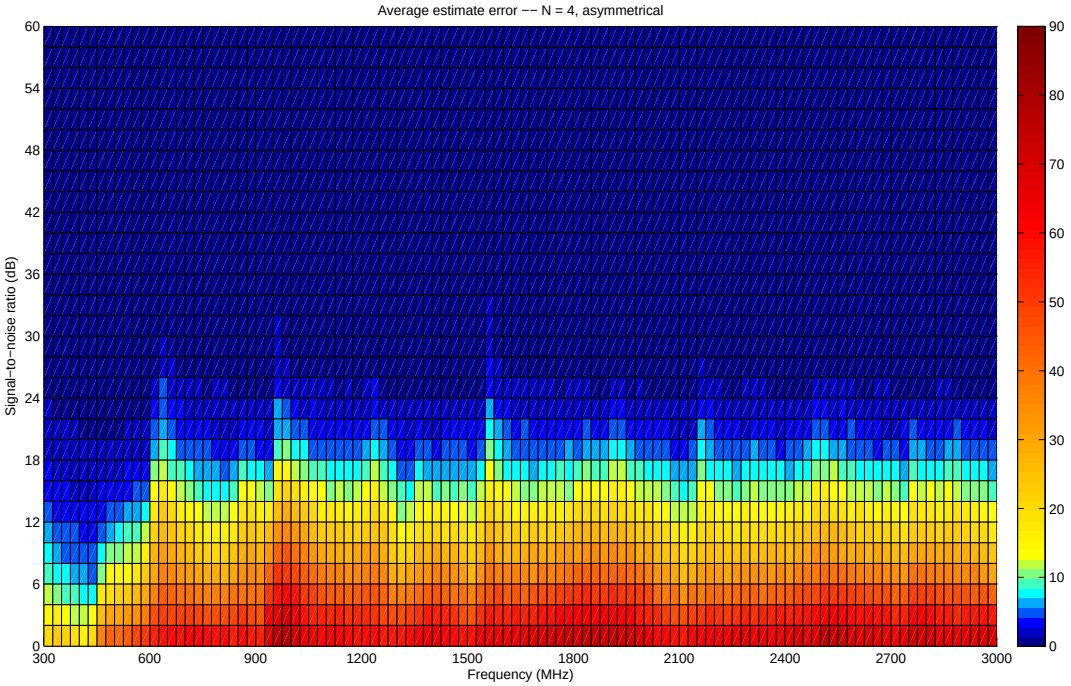

(b) Average estimation error for the asymmetrical layout.

Figure 4.5: Colour map plots of the mean AoA estimation error, for $N = 4$, averaged over all angles, plotted over frequency and SNR.

Stellenbosch University https://scholar.sun.ac.za

4.4 Conclusion

This chapter details the workings of a phase correlation DF algorithm. It has demonstrated that symmetrical 4-antenna layouts are inherently restricted to providing narrowband DF solutions, and that wideband performance can be obtained if the original placement is varied. The results that are generated further provide a useful indication of the phase errors that can be tolerated in order to operate within a specified angular resolution, over a desired frequency band. The algorithm therefore serves not only to yield estimated angles of arrival from real measured data, but also as a reconfigurable design tool for evaluating the performance of arbitrary receiver layouts. These result are verified by practical measurement in the following chapter.

Stellenbosch University https://scholar.sun.ac.za

Chapter 5

Field Measurement Results

"There is geometry in the humming of the strings, there is music in the spacing of the spheres."

—Pythagoras

5.1 Introduction

This chapter presents the results that were obtained from the field measurements conducted to verify the accuracy of direction finding with the phase correlation method. The four manufactured ACD antennas were used to measure a pulse source that radiates from known locations. The phase differences of the received signals were subsequently extracted and correlated with the expected phase differences generated by the DF algorithm in Chapter 4. The AoA estimation is then compared to the actual angle to evaluate the resolution of the setup. Results are obtained for receivers in a symmetrical and an asymmetrical layout to verify the simulated difference in performance.

5.2 Measurement Setup

The field measurements were performed at Coetzenburg sports fields, beneath Stellenbosch mountain, which was selected due to the area's natural shielding from noise sources. The system configuration consisted of the four ACD receivers, a pulse source, and a high-speed oscilloscope. A labelled photo of the setup is provided in Figure 5.1. Not indicated is the battery power supply, and the laptop used for capturing recorded data.

The radiator is an Emission Reference Source made by Laplace Instruments, and consists of a loaded monopole that periodically emits a linearly polarised pulse containing energy from 30 MHz up to 1 GHz. The signals received by the ACD

Stellenbosch University https://scholar.sun.ac.za

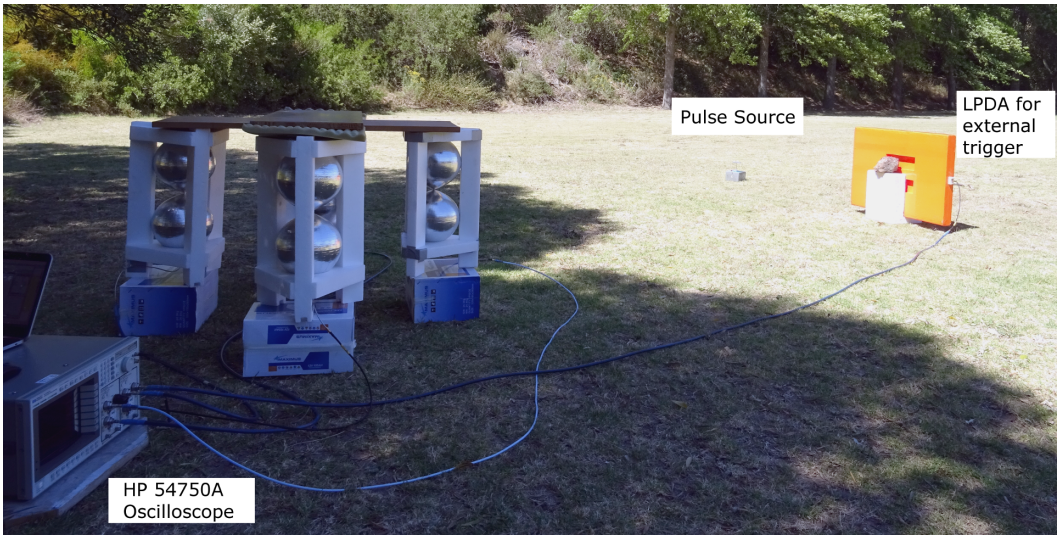

Figure 5.1: Photo of the field measurement setup.

antennas are measured on a 4-channel, high-bandwidth HP 54750A oscilloscope, which requires an external trigger source to capture the recording.

Due to the physical size of the ACD antennas, it was necessary to use a test setup with separation distances of at least a metre, to avoid the receivers capturing significant reflections off one another. The two configurations that were tested therefore corresponds to the automatically generated layouts shown in Figure 4.1, after scaling by a factor of two. This 1 metre separation distance represents a half-wavelength design for 150 MHz, and it is therefore expected that the symmetrical layout will begin to encounter ambiguity errors at 300 MHz. The asymmetrical layout should therefore perform accurately by comparison. It must be stated that the antenna layouts were approximate, which adds some phase noise in the form of a discrepancy with expected layout.

It was found that noise in the environment was in fact too significant to trigger on the pulse if the source was placed far away. Therefore, it was necessary to perform measurement at a range of only 5 metres from the radiator. This means that with the 1 m separation distance that was used, the antennas are only in the far field for signals below 750 MHz. Results are restricted to be processed below this point, as measurements above this frequency will contain added phase errors.

The position of the pulse source was varied in order to perform a total of seven measurements for each of the two configurations. The first measurement placed the source at a defined angle of 0°. Five subsequent measurements were made at 2.5° increments, up to a source angle of 12.5°. A final, additional measurement was then made at 45°. The 4-channel data recordings were captured for each of these cases. Measurement were processed individually to obtain a collection of estimated bearing results, which could then be compared with the actual angles.

Stellenbosch University https://scholar.sun.ac.za

Table 5.1: Measurement results of the cable propagation delays.

Cable length	Manufacturer / Cable series	Given cable velocity ($\times c$)	Measured velocity ($\times c$)	Phase error at 1 GHz
4 m	Huber+Suhner / Sucoflex 104A	77%	77.53%	10.2°
3.1 m	Huber+Suhner / Sucoflex 104	77%	77.44%	5.80°
1.5 m	Huber+Suhner / Sucoflex 104A	77%	76.40%	−6.54°
1 m	Times Microwave / Ultraflex LMR-195	76%	71.29%	−33.2°

5.3 Direction Finding Results

The time domain measurements were captured on the oscilloscope and recorded on a laptop. Subsequent post-processing was performed to extract the phase differences to test with correlation. The first step was to correct for the influence of the cable lengths, such that the signals can be compared without additionally contributed delays.

5.3.1 Correcting for Cable Effect

The antennas were configured with four different cables, each with a different time delay (velocity of propagation). Different cables had to be used, due to lack of availability of long cables that are more costly. Results were first processed by correcting for the cable velocities as specified in the relevant data sheets, but accurate results could not be obtained. It was therefore necessary to determine the phase variation directly, by measuring the S_{21} of the cable on a VNA. The difference in specified and measured cable velocities are composed in Table 5.1, with the resulting phase discrepancies indicated (compared to specified velocity). It is clear that for a final system design, these cable effects must be accurately accounted for. The ideal case is certainly that identical cables are used, such that there is no inconsistent variation with temperature, for instance.

An example of the results before and after cable correction are presented in Figure 5.2 to illustrate the measurements that were obtained. This is shown for the case of the symmetrical layout receiving a pulse from a 45° angle (relative to the axis between antennas 1 and 3). It is therefore expected that the wavefront will arrive at antennas 1 and 2 at the same time, as well as for antennas 3 and 4. After correcting for the cable effect, this is indeed the case.

Stellenbosch University https://scholar.sun.ac.za

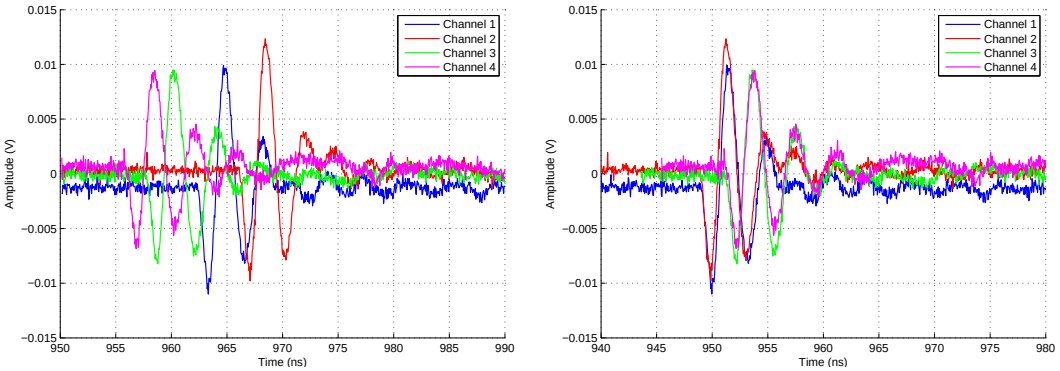

(a) Time domain measurement of the received signals.

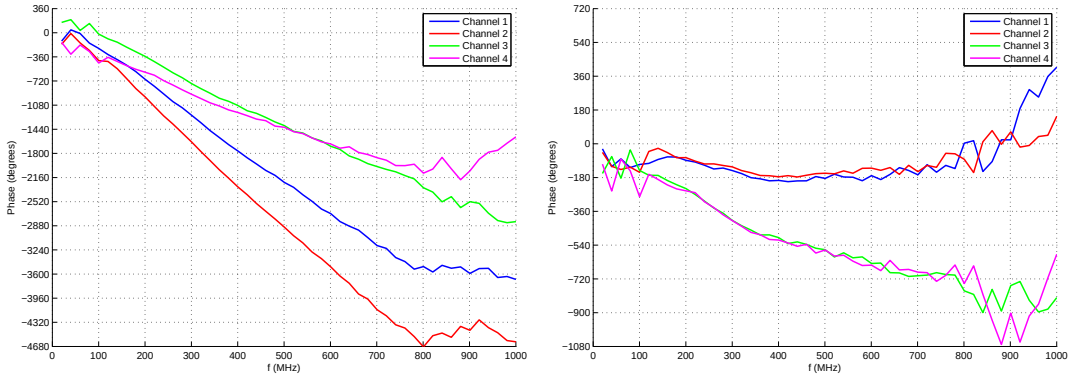

(b) Phase spectrum of the received signals.

Figure 5.2: 4-channel measurements obtained for a symmetrical layout and a source position at 45°. Before (left) and after (right) correcting for the cable effect. It is expected that signals in channels 1 and 2 should line up, due to the wavefront arriving at the same time – as with channels 3 and 4. The phase noise that is observed past 750 MHz is due to these signals being within the near-field of the receivers.

Stellenbosch University https://scholar.sun.ac.za

Table 5.2: Angle of arrival estimation results for symmetrical layout.

Actual AoA	Estimated AoA at 300 MHz	Estimated AoA at 480 MHz
0°	97°	0°
2.5°	146°	314.2°
5°	142°	314.6°
7.5°	111°	7.6°
10°	12°	205°
12.5°	15°	203°
45°	47°	48°

5.3.2 Phase Correlation

Results for the symmetrical layout

The measured phase differences are extracted from the FFT of the time signals, and wrapped to be bounded within 360°, so as to be used for correlation. This is performed for the 7 measurements of each of the configurations tested. Results are evaluated at 2 frequency points, to verify simulated expectations

Before interpreting results, the algorithm in Chapter 4 is applied to generate an expectation of AoA estimation performance for the corresponding layouts used. The simulated, expected results are provided in Appendix D.2, which indicate the regions of the field of view where ambiguities may be present. The simulations show that, for the symmetrical case, a 300 MHz measurement will yield large errors for source angles on the axes; at 480 MHz, exactly on the axes appears to be error-free, but is surrounded by an ambiguous region.

The AoA estimation results that are obtained for the symmetrical layout, with 1 metre separation distance, is provided in Table 5.2. The red cells indicate large ambiguity errors, whereas green indicates an accurate resolution of the true angle, almost all within ±2.5° error. These results match up accurately with the expectation: the axes of the symmetrical layout are clearly ambiguous for the 300 MHz case. Measurements away from the axes become accurate, which – due to already occurring at the 10° source angle – gives an indication that the SNR of the measurement is in fact better than 26 dB, for which the expected results were generated. For the 480 MHz case, a source in line with the axis was resolved accurately, but the area around it then become ambiguous. The accurate resolution of the 7.5° angle again suggests that the true SNR of the measurement is closer to 30 dB.

Plots of the root-mean-square error function for the 45° source angle measurements are provided in Appendix D.3, and show how the maximum correlation method works. It is clear that the actual source angle correlates best, but there are regions that also have improved correlation at higher frequencies, showing that added noise could result in the maximum correlation method returning errors.

Stellenbosch University https://scholar.sun.ac.za

Table 5.3: Angle of arrival estimation results for asymmetrical layout.

Actual AoA	Estimated AoA at 300 MHz	Estimated AoA at 480 MHz
0°	359.3°	358°
2.5°	4°	1.8°
5°	6.5°	4.6°
7.5°	9.1°	7.5°
10°	13.4°	249.6°
12.5°	15.5°	248.9°
45°	44°	42.6°

Results for the asymmetrical layout

The expected results in Appendix D.2 show that the 300 MHz signal should be resolved accurately, within ±2°, and that the 480 MHz case may in fact have some ambiguities appearing around a source angle of 10–20°.

The results obtained in Table 5.3 therefore match up precisely with the expectation. The 300 MHz case yielded no ambiguity errors, which is a great result for frequency wavelengths that are equal to the separation distance, as this is expected to be a case that is prone to phase ambiguities.

The 480 MHz measurement returned a couple of errors at 10° and 12.5°. These errors suggest that the SNR is in fact *worse* than 26 dB, as used for the expected results. This is believed to be due to the fact that the placement of the antennas was fairly approximate, due to the practical difficulty in constraining the set of antenna separation distances with what was specified to the algorithm. For example: the wavelength of a 480 MHz signal is 62.5 cm; therefore, a 1 cm error in antenna placement will yield a $360° \times \frac{1}{62.5} = 5.76°$ phase error. This becomes very substantial if each antenna is misplaced. The results therefore reveal that highly accurate angular resolutions will be obtained with more precise antenna placement. Nevertheless, the accurate coincidence with the generated expectations from the algorithm in Chapter 4 reveals that the simulation results provide an accurate evaluation of the performance of an arbitrary receiver layout.

Following the measurements, results were generated for a 5-receiver system to observe the theoretical accuracy improvement that may be obtained with the additional phase comparisons. Figure 5.3 shows the simulated, average AoA estimated error over frequency and SNR for a symmetrical configuration of 5 antennas. The result for an asymmetrical layout is effectively the same, due to the 5 receivers already not having full rotational symmetry. The required SNR to direction find over a wide band reduces significantly. This serves as an indication of what can be accomplished with further study.

Stellenbosch University https://scholar.sun.ac.za

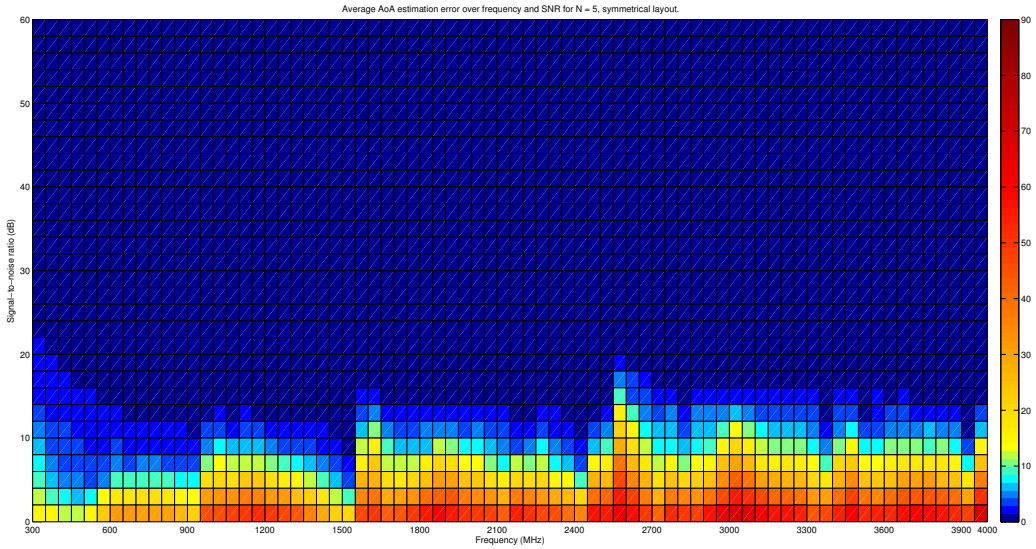

Figure 5.3: Colour map plot of the mean AoA estimation error for a 5-antenna configuration.

5.4 Conclusion

A field measurement was conducted to demonstrate the DF capability of an asymmetrical antenna configuration. An oscilloscope and a pulse emitter was used to capture time-domain measurements, which were subsequently post-processed to extract the measured phase differences. The phase correlation method is applied to the result, and it has been demonstrated that frequencies beyond a wavelength separation distance can be accurately resolved within 2.5° accuracy, even with fairly approximate antenna placement. This matches accurately with the simulated expectations that were generated by the algorithm in Chapter 4. The simulation results can therefore be interpreted with more certainty.

Further investigation remains to be done to find the optimal separation distance for operating over a specific frequency band of interest. For a higher frequency DF application, physically smaller antennas can be manufactured to permit the small separation distances that will be required. A system with a front-end interface can then be developed to process measurements in real-time, and store a recorded history of results.

Stellenbosch University https://scholar.sun.ac.za

Chapter 6

Conclusions and Recommendations

"Problems worthy of attack prove their worth by hitting back."

—Piet Hein

This thesis has presented the design of two components that make up a phase correlation direction finding system: the omnidirectional, wideband receivers; and the algorithm for processing the measurements to yield an estimated angle of arrival.

A set of four asymptotic conical dipole antennas were manufactured with a 3D-printed plastic design, which achieved a measured impedance bandwidth in excess of 100:1, with a low-frequency cut-off at 270 MHz. These antennas served as the receivers in a DF calibration test: time-domain recordings were captured of an incoming wavefront from a pulse source placed at known angles. The set of measured phase differences was correlated with a dataset of expected phase differences, one which is computationally generated according to the antenna placement, where the entry with maximum correlation provides the estimated AoA. The estimations were compared with the actual source angles to verify the simulated performance of two separate receiver configurations: a 4-antenna symmetrical layout, and a similar asymmetrical layout. It was demonstrated that symmetry inherently restricts the system to a narrow bandwidth, due to phase ambiguities that occur over the field of view at higher frequencies. This is in contrast to a layout with varied spacing, which was applied to yield accurate estimations within 2.5° over a wider bandwidth. These results of the measurement agree with simulated expectations, which indicate the signal-to-noise ratios that are required in order to operate over a desired frequency range. The simulations can therefore be applied as a design tool in configuring the optimal antenna placement of a final DF system.

Further investigation therefore remains in applying the phase correlation algorithm in a standalone, front-end interface, in order to provide a real-time monitoring solution. This can be physically realised with a multi-channel analog-to-digital con-

Stellenbosch University https://scholar.sun.ac.za

verter and a high-performance FPGA card. For a wideband application to yield accurate results, it may be necessary to have additional receivers in the system, as AoA estimations will be improved substantially, with greater resistance to phase errors. There is also great potential for the accuracy of the correlation method to be improved, as maximum correlation is the simplest possible approach. An alternative method that may further reduce ambiguities is to correlate measurements at multiple frequency points around the signal of interest, and to include cross-correlation results in the AoA computation.

Further advancements will lead to the development of an accurate, wideband, real-time direction finding system, intended to allow for the successful operation of the MeerKAT radio telescope.

Stellenbosch University https://scholar.sun.ac.za

Bibliography

[1] NRAO. *VLA Basics*. Collecting area calculated from dish size, [Online]. Available: https://public.nrao.edu/telescopes/vla/vla-basics (Date last accessed on Aug. 2, 2016).

[2] SKA. *The location of the SKA*, [Online]. Available: https://www.skatelescope.org/location/ (Date last accessed on Aug. 4, 2016).

[3] SKA. *MeerKAT dishes at the core site in the Karoo, South Africa. Credit: SKA South Africa*, [Online]. Available: http://newsletter.skatelescope.org/category/consortium-reports-skaenews-december2015/aiv-report-skaenews-december2015/ (Date last accessed on Aug. 4, 2016).

[4] SKA. *Australia*, [Online]. Available: https://www.skatelescope.org/australia/ (Date last accessed on Aug. 4, 2016).

[5] SKA South Africa. *SKA-SA Public: KAT-7*, [Online]. Available: http://public.ska.ac.za/kat-7 (Date last accessed on Aug. 4, 2016).

[6] SKA South Africa. *MeerKAT Spec and Schedule*, [Online]. Available: http://public.ska.ac.za/meerkat/meerkat-schedule (Date last accessed on Aug. 4, 2016).

[7] SKA. *SKA Project*, [Online]. Available: https://www.skatelescope.org/project/ (Date last accessed on Aug. 4, 2016).

[8] SKA Africa. *Location*, [Online]. Available: http://www.ska.ac.za/about/location/ (Date last accessed on Aug. 4, 2016).

[9] South Africa Dept. of Science and Technology, *Notice of intention to make regulations on the protection of the Karoo Central Astronomy Advantage Areas in terms of the Astronomy Geographic Advantage Act, 2007*, Available: http://www.gov.za/sites/www.gov.za/files/39442_gon1166s.pdf, Nov. 23, 2015.

[10] SKA Organisation, *Expert panel on Radio Quiet Zone and RFI Regulation report*, Available: https://www.skatelescope.org/wp-content/uploads/2012/06/79_Report_of_The_Expert_Panel_on_Radio_Quiet_Zone_and_RFI_Regulation.pdf, Oct. 12, 2011.

Stellenbosch University https://scholar.sun.ac.za

[11] H. Pienaar, "Karoo Array Telescope site shielding: Laboratory, computational and multi-copter studies," PhD thesis, Dept. Elect. & Electron. Eng., Univ. Stellenbosch, South Africa, Dec. 2015.

[12] N. C. Thompson, "RFI mitigation in radio astronomy," M.Eng. thesis, Dept. Elect. & Electron. Eng., Univ. Stellenbosch, South Africa, Apr. 2014.

[13] T. J. Phiri et al., "Propagation modelling for the South African SKA site," in *IEEE Antennas Propagat. in Wireless Commun.*, 2015.

[14] S. O. Kuja et al., "MeerKAT radio telescope electromagnetic coupling investigations," in *International Symposium on EMC*, 2016.

[15] C. A. Balanis, *Antenna Theory: Analysis and Design*, 3rd ed. John Wiley & Sons, 2005.

[16] S. R. Saunders and A. Aragón-Zavala, *Antennas and Propagation for Wireless Communication Systems*, 2nd ed. John Wiley & Sons, 2007.

[17] P. K. Langat, "Power-line sparking noise characterisation in the SKA environment," PhD thesis, Dept. Elect. & Electron. Eng., Univ. Stellenbosch, South Africa, Dec. 2011.

[18] Avionics Department, "Electronic Warfare and Radar Systems," Naval Air Warfare Center Weapons Division, Tech. Rep., 2013.

[19] T. T. Wu and R. W. P. King, "The cylindrical antenna with nonreflecting resistive loading," *IEEE Trans. Antennas Propagat.*, vol. 13, no. 3, pp. 369–373, May 1965.

[20] J. G. Maloney, "Optimization of a conical antenna for pulse radiation: An efficient design using resistive loading," *IEEE Trans. Antennas Propagat.*, vol. 41, no. 7, pp. 940–947, 1993.

[21] J. James and A. Henderson, "Electrically short monopole antennas with dielectric or ferrite coatings," *Proc. IEE*, vol. 125, no. 9, pp. 793–803, Sep. 1978.

[22] Z. Wang et al., "Giant permittivity and low dielectric loss of SrTiO3 ceramics sintered in nitrogen atmosphere," *Journal of the European Ceramic Society*, vol. 34, no. 7, pp. 1755–1760, Jul. 2014.

[23] K. S. Moon et al., "Dielectric properties of epoxy-dielectrics-carbon black composite for phantom materials at radio frequencies," *Journal of Applied Polymer Science*, vol. 77, no. 6, pp. 1294–1302, 2000.

[24] P. G. Wiid, "The answer is in fact 41, or How to get 35:1 bandwidth from a cone antenna," in *IEEE Antennas Propagat. in Wireless Commun.*, 2015, pp. 1060–1063.

[25] J. A. Andriambeloson and P. G. Wiid, "A 3D-printed PLA plastic conical antenna with conductive-paint coating for RFI measurements on the MeerKAT site," in *IEEE Antennas Propagat. in Wireless Commun.*, 2015, pp. 945–948.

Stellenbosch University https://scholar.sun.ac.za

[26] S. A. Schelkunoff and H. T. Friis, *Antennas: Theory and Practice*. John Wiley & Sons, 1952, p. 318.

[27] N. C. De et al., "Design and experimental investigation of the asymptotic conical dipole," *IEEE Trans. Electromagn. Compat.*, vol. 37, no. 2, pp. 282–285, May 1995.

[28] T. L. Simpson, "Analysis and design of the Schelkunoff-Friis antenna," *IEEE Antennas Propagat. Soc. Int. Symp.*, pp. 611–614, Jul. 2006.

[29] O. B. Jacobs et al., "Analysis and design of a wide band omnidirectional antenna," *Microwave and Optical Technology Letters*, vol. 53, no. 6, pp. 1352–1356, Jun. 2011.

[30] MMUST. *ECE 451 L Radar Engineering, Introduction to Radar*, [Online]. Available: `http://mmust.elimu.net/BSC(ELEC_COMM)/Year_4/` (Date last accessed on Nov. 3, 2016).

[31] Rohde & Schwarz, "Introduction into theory of direction finding," Radiomonitoring & Radiolocation, Tech. Rep., 2011/2012.

[32] R. A. Poisel, *Electronic Warfare Target Location Methods*, 2nd ed. Artech House, 2012.

[33] M. Groch, "HV transmission line and tower inspection safe-fly zone modelling and metrology," M.Eng. thesis, Dept. Elect. & Electron. Eng., Univ. Stellenbosch, South Africa, Dec. 2013.

Stellenbosch University https://scholar.sun.ac.za

Appendix A

Supplementary FEKO Simulation Results

A.1 Varied Meshing of Feed Region

The local mesh of the feed region was varied, to observe the difference in simulation results at higher frequencies. It was finally selected to use the mesh that is 3 times finer than default; to be more precise, the local mesh size was defined to be 1/20th of the circumference of the port.

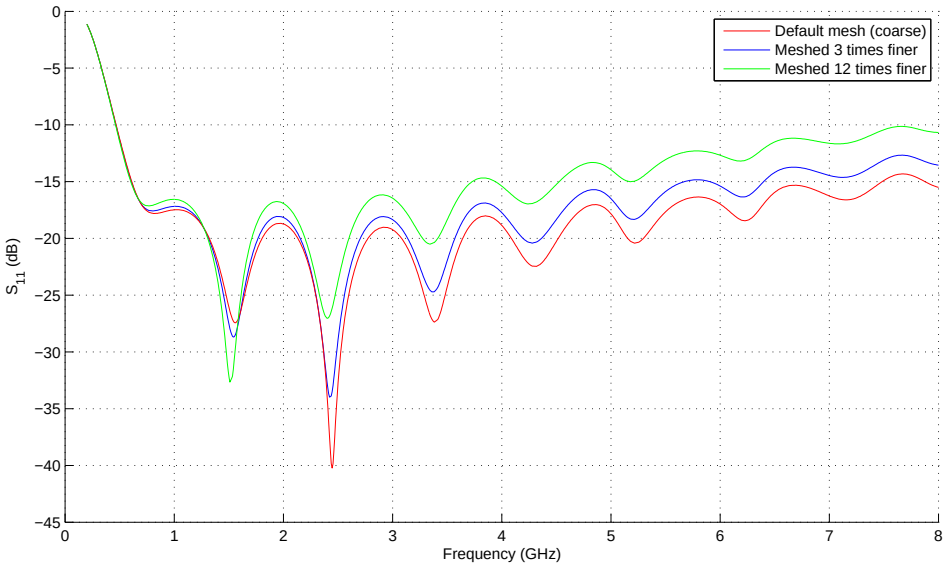

Figure A.1: Difference in simulated reflection coefficient for varied mesh sizes of feed region

Stellenbosch University https://scholar.sun.ac.za

A.2 Effect of Serrated Edges on a Monocone

As discussed in Section 3.2.1, the simulated reflection coefficients of a serrated monocone did not yield any remarkable improvement over that of a standard design. The results for some test cases are shown in Figure A.2. There is some variation in results at higher frequencies, but no improvement at low frequencies. Judging from the results, the total number of serrations does not have as large of an influence as the serration length, but either case gives negligible simulated improvement.

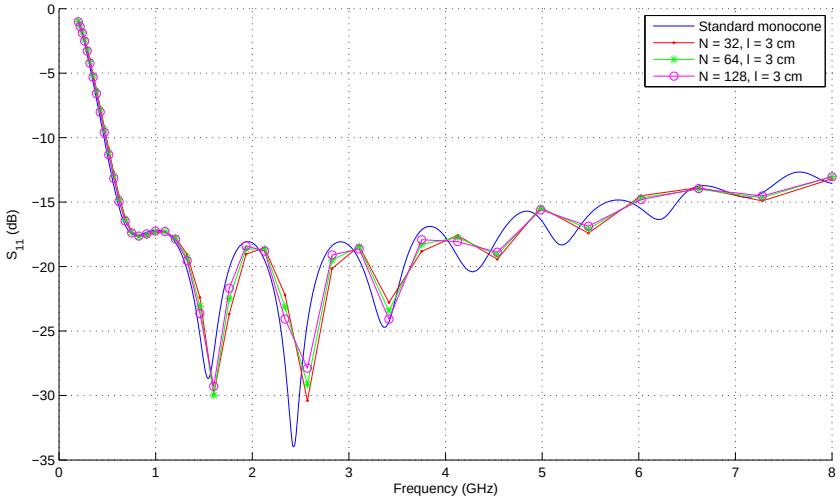

(a) Varying the total number of serrations.

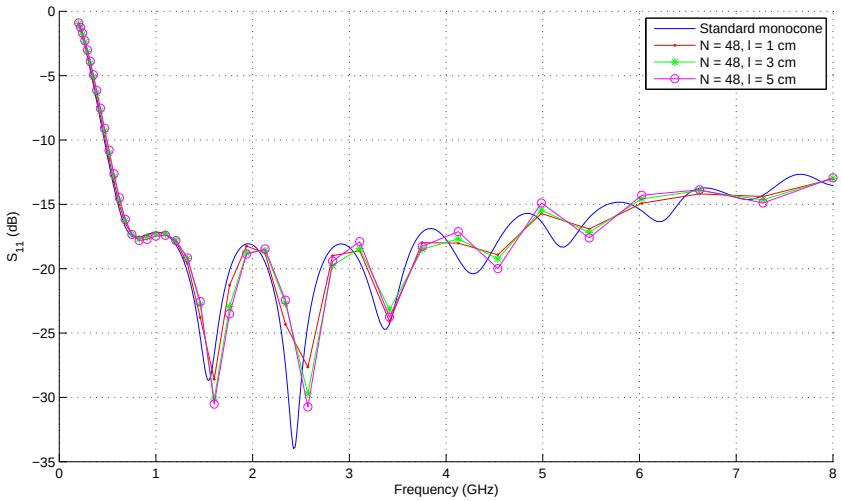

(b) Varying the length of the serrations.

Figure A.2: Simulated reflection coefficient of a serrated cone compared with a standard cone.

Stellenbosch University https://scholar.sun.ac.za

A.3 Resistive Loading with Serrations

The influence of added serrations at the top edge of a monocone was again simulated to identify if a worthwhile performance improvement can be achieved with the correct configuration. To investigate the influence, serrations of various lengths were added to a fully loaded cone.

From Figure A.3 below, it is apparent that there is only slight variation between the test cases. The reason for the lack of substantial variation is discussed in Section 3.2.1.

When analysing the different serration lengths, it appears that the longer tooth (of 5 cm) again gives the best result. This case only gives mild improvement, but the results correlates with the finding in Figure A.2(b).

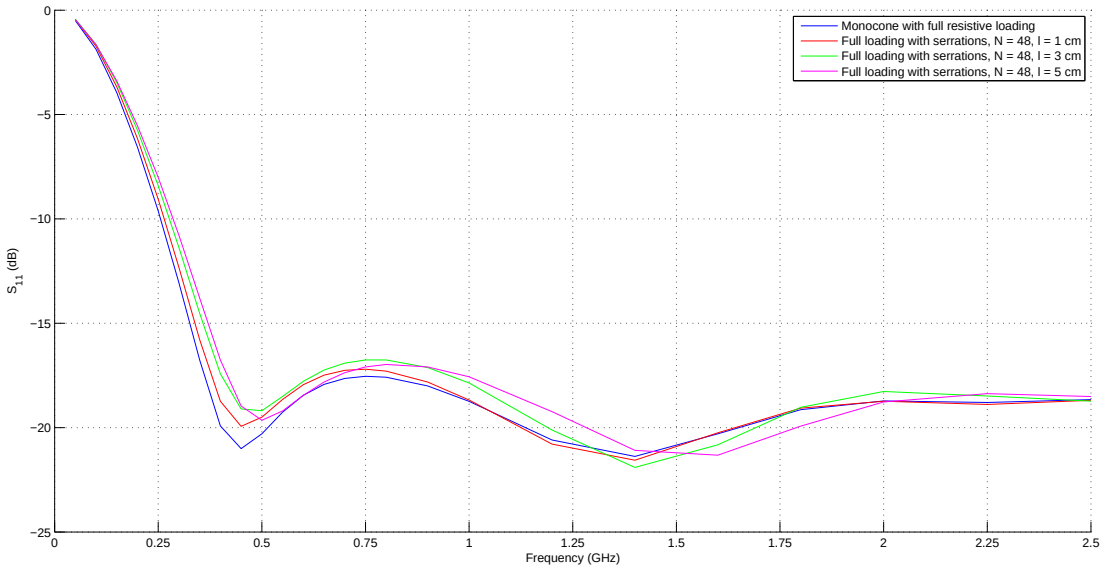

Figure A.3: Simulated reflection coefficient for a resistively loaded monocone with serrations of different lengths

Stellenbosch University https://scholar.sun.ac.za

Appendix B

MATLAB Code

B.1 Code to Generate Serrated Edges

The following code computes a list of (x, y, z) coordinates for the points that define a line of serrated edges for the top of a conical antenna. The variables can be adjusted as desired, for an arbitrary number of serrations, of arbitrary length, for a cone of any radius and angle. The output is a list of points that can be imported to FEKO as a polyline. The line must be projected onto the conical antenna, and the undesired faces deleted. In the mesh settings, it may be required to ignore geometry smaller than roughly 0.003%, in order for the FEKO solver to execute.

```
N = 48; %number of triangles
l = 0.05; %length of teeth (metres)
a = 41; %cone angle
rc = 0.12; %radius of cone (metres)

theta = 0:2*pi/(2*N):2*pi; %angular space of N points

rt = l*cos(a*pi/180); %This is the length of the serrated teeth
   projected on x/y plane
%It is the diff in x/y radius at the top and bottom of the tooth

r = [repmat( [rc, rc - rt] , 1 , N) rc];
%This is a repeated sequence of x/y lengths toward the serrated points
%There are 2N points, with lengths alternating between rc and rc-rt

%The x/y/z coordinates are computed from these values of r:
z = tan(a*pi/180).*r;
x = sin(theta).*r;
y = cos(theta).*r;

%Resulting list of point coordinates
M = [x' y' z']
%Save to text file and import to FEKO as polyline coordinates.
```

Stellenbosch University https://scholar.sun.ac.za

B.2 Wu-King Loading Profile

The equations for the Wu-King loading profile are presented at length in [19] and [20]. Groch [33, Appendix D.1] applied the equations in a MATLAB script, which is presented here for the sake of accessibility.

```
%Resistively-loaded Profile
a = 0.12; %antenna radius
h = 0.159; %antenna length
u = 0:(0.2*pi/100):(0.2*pi);
i = numel(u);
j = 1;
while (j <= i)
    C(j) = ((1 - cos(sqrt((u(j)).^2+(0.042).^2)))/(sqrt((u(j))
        .^2+(0.042).^2)));
    S(j) = ((sin(sqrt((u(j)).^2+(0.042).^2)))/(sqrt((u(j)).^2+(0.042)
        .^2)));
    j = j + 1;
end
Zc = trapz(u,C);
Zs = trapz(u,S);
A = asinh(h/a);
B = abs(-exp(-sqrt(-1)*pi*0.2));
Phi = (2 *(A - Zc - sqrt(-1) * Zs)) + (sqrt(-1)*2/(0.1*pi) * (1 + B));

i = 1;
Z = 0:(h/100):h;
j = numel(Z);
while(i <= j)
    z(i) = 0.1*(15 * Phi)/(h - abs(Z(i)));
    i = i + 1;
end

z0 = 15*Phi
figure
plot(100*Z,z,'r','LineWidth',3)
grid on
hold on
plot(100*Z,z,'xk')
xlabel('Length [cm]', 'fontsize', 20)
ylabel('Resistance [Ohms]', 'fontsize', 20)
set((findobj('type','axes')),'fontsize',16)
```

Stellenbosch University https://scholar.sun.ac.za

B.3 Calculating Combined Curves for the ACD

The following code calculates the scaling and translation that is necessary to model two combined curves with different profiles. The Z_1 and Z_2 values define the desired curves to be joined, with h as maximum height. The h_1 and $x_{translate}$ variables must be reiterated according to the output of the code.

```
%% Initial settings
c0 = 299792458;
eps0 = 8.85418781761e-12;
n = 2.5; %for a dipole. Change to 1.25 for a monopole

Z1 = 50; %Desired impedance curves. This curve is at the feed
Z2 = 70; %This curve is at the top

h = 0.25; %This is the desired maximum height. Final height will be
    reduced by the necessary translation
h2 = h;

%% Reiterate the following values for curves to join
h1 = 96.465457/114.922107*h; %Begin with h. This value must be scaled
    according to output.
x_translate = 25.902548/1000 + 2.252395/1000; %This value is computed
    iteratively. Start at 0 and adjust to output.

%% Calculate curves
k1 = exp(4*pi*eps0*c0*Z1/n); %Constant to define curve shape
k2 = exp(4*pi*eps0*c0*Z2/n);

theta_max1 = acos( (-1 + k1)/(1 + k1) ); %Maximum angle of plot
theta_max2 = acos( (-1 + k2)/(1 + k2) );

th1 = 0:theta_max1/10000:theta_max1; %Angular coordinates
th2 = 0:theta_max2/10000:theta_max2;

r1 = h1*( ( (1+k1)*cos(th1) + (1-k1) ) ./ ( (1+k1)*cos(th1) + (1 - k1)
    *(cos(th1)).^2 ) ); %Radial coordinates of curve
r2 = h2*( ( (1+k2)*cos(th2) + (1-k2) ) ./ ( (1+k2)*cos(th2) + (1 - k2)
    *(cos(th2)).^2 ) );

%% Convert to cartesian, and find necessary translation factors
[x1,y1] = pol2cart(th1,r1); [x2,y2] = pol2cart(th2,r2);

[y_1, i1] = max(y1); [y_2, i2] = max(y2);
sprintf('The maximum width of curve 1 is %f metres, and occurs at
    index %d', y_1, i1)
sprintf('The maximum width of curve 2 is %f metres, and occurs at
    index %d', y_2, i2)

x1_max = x1(i1); x2_max = x2(i2); %x-coordinates of the max width
```

Stellenbosch University https://scholar.sun.ac.za


```
%Define the region where curves exist
under = x1 < x1_max; %Beginning of first curve
over = x2 > x2_max; %New curve begins
over2 = x1 > x1_max; %Where old curve would have continued

x2 = x2 - x_translate; %Translate

figure; hold on; %Plot the combined curves
plot(x1(under),y1(under));
plot(x2(over),y2(over),'r');
plot(x1(over2),y1(over2),':');

h1_max = y_1*1000; h2_max = y_2*1000;
sprintf('\nIf widths are not equal, curves must be scaled.\n')
if h1_max - h2_max > 0.00001
    sprintf('First scale h1 (in initial settings) to be = %f/%f*h,
       then re-run', h2_max, h1_max)
end
axis([0,h,0,1.15*h1_max/1000]);

x1_max = x1(i1)*1000; x2_max = x2(i2)*1000;
sprintf('Then add the following to the current x_translate value (in
   initial settings) = %f/1000', x2_max - x1_max)

th1_max = th1(i1)*1000;
th2_max = th2(i2)*1000;
sprintf('\nThe maximum theta values to plot up to are th1_max = %f,
   th2_max = %f (in miliradians)', th1_max, th2_max)
sprintf('If the blue and red plots align, then the h1 scaling and
   x_translate values can be used for the FEKO model.\nSome minor
   adjustment to these values will be necessary for the two FEKO
   curves to align for union.')
```

Stellenbosch University https://scholar.sun.ac.za

B.4 Direction Finding Algorithm

The following DF algorithm was coded to construct a dataset of expected phase differences for an arbitrary configuration of N antennas. The angular resolution of the computation and the frequency range of interest can be defined as desired. A signal-to-noise ratio parameter can be adjusted to evaluate the error sensitivity of an antenna layout at different frequency points.

The code begins by generating an automatic antenna configuration based on the initialised parameters. The layout can be customised as needed. What follows is a computation of the expected phase difference dataset for the corresponding layout. The performance of the configuration is then simulated by extracting an expected measurement, adding noise (based on the SNR parameter), and correlating the noisy measurement with the dataset. This is performed over the full angular space, to identify the source angles that may give ambiguous results. The number of errors are tallied to provide a quantitative evaluation of a given layout's performance at different frequencies. Example output is provided in Section 4.3.

The following code concludes with the processing of the real measurement results obtained in Chapter 5.

```
%% Initial parameters
c = 299792458; %speed of light
i = sqrt(-1);

N = 4; %Number of antennas in layout
Np = (N-1)*N/2; %Total number of phase differences between N antennas

layout = 0; %0 for symmetrical layout. 1 for varied spacing

f_L = 300e6; %Lowest frequency point
f_H = 4000e6; %Highest frequency point

Nf = 3700/50 + 1; %Number of frequency points to compute between f_L
    and f_H (must be at least 2)
freq = f_L : (f_H-f_L)/(Nf-1) : f_H; %Frequency space

Nr = 360*7; %Number of radial points to compute
theta = 0 : 2*pi/Nr : 2*pi*(1-1/Nr); %Radial space
%The code may require minutes to compute over a high angular
    resolution.
%For fast computation, keep Nr < 360*30

%SNR = 26; %Set the desired SNR of the measurement error (in dB)
%This tests the error sensitivity of the layout at diff freq points
%For a sweep over SNR values, set the following instead:
Nsnr = 31; %number of SNR values to compute over
SNR = 0:2:2*(Nsnr-1);

%% Open up parfor loop (parallelization) capability
```

Stellenbosch University https://scholar.sun.ac.za


```
%This is especially necessary if computing a fine angular resolution
    over several frequency points
if matlabpool('size') == 0 % checking to see if pool is already open
        matlabpool open 4 %Change to 4 for a quadcore processor. 2 for
            dual. 8 if you're lucky, 1 if you're not.
end

%%%%%%%%%%%%%%%%%%%%%%%%%%%%%%%%%%%%%%%%%%%%%%%%%%%%%%%%%%%%%%%%%%%%%%%
%% Antenna Layout
%%%%%%%%%%%%%%%%%%%%%%%%%%%%%%%%%%%%%%%%%%%%%%%%%%%%%%%%%%%%%%%%%%%%%%%
%Compute coordinates of Antennas. Distributed radially starting at
    theta = 0;
%Coordinates stored as complex values, corresponds to x,y plot

% The separation distance is computed to be half the wavelength f_L
 d = c/f_L / 2 / 2; %Mean radial distance for antennas
% d = 0.5; %To force own layout, change to desired radius. The
    following layout generation code will have to be commented out in
    this case.
%  A=  [ 0.4913, -0.0308 + 0.5272i, -0.4876 - 0.0601i , -0.0138 -
    0.4727i]; %Coordinates of field measurement (varied layout)

%Asymmetrical variations are selected by binary value of "layout"
d_v = c/f_H / 2 / 2 * layout; %Variation around mean - around the
    order of f_H wavelength / 2.
d_th = 2*d_v/d * layout; %Variation in angular layout

%Receivers are placed at these angles (if placed evenly, symmetrical):
an = 0: 2*pi/N : 2*pi*(1-1/N);

%Calculate the coordinates for each receiver
r(N) = zeros; %Radius of antenna location
th(N) = zeros; %Angle at which to place antenna
A(N) = zeros; %Vector to store antenna coordinates
for p = 1:N
    r(p) =     d  + d_v *sin( an(p)        )*(N+1-p)*(p-1)/p/N;
    th(p) = an(p) - d_th*cos( an(p) + d_th )*(N+1-p)*(p-1)/p/N;
    %if layout = 0, then r(p) and th(p) = d.

    A(p) = r(p) * exp(i * th(p)); %Vector with antenna coords
end

%layout = 1 will introduce the varied spacing
%The above function was implemented ad hoc, and is not necessarily
    optimal.
%Purpose of d_v * sin()*factor is for r to increase with theta, and
    then to
%decrease back to 0 as p moves around the layout.
%As for th() -- while r increases, th decreases

%Now compute the distances between each element
```

Stellenbosch University https://scholar.sun.ac.za


```
D(N,N) = zeros;
for p = 1:N
    for q = 1:N
        D(p,q) = abs(A(p) - A(q));
    end
end
%Matrix D(i,j) contains absolute distances between antennas A(i) and A
    (j).

%D is used to scale the spacing according to f_L wavelength/2 or the
    set distance
Dmax = max(max(D));
%Normalise max separation to = lambda_L / 2 [== 2*d]
n_factor = 2*d / Dmax;
A = n_factor*A; D = n_factor*D;


%Plot the layout, with separation distances shown
 figure; hold on; grid on;
for p = 1:N
    text( real(A(p)) , imag(A(p))+Dmax/50, strcat('A',num2str(p) ) );
    for q = 1:N
        if D(p,q) ~= 0
            %plot lines individually, followed by text plotted around
                the middle of the line
            line(  [  real(A(p))  real(A(q))  ] , [  imag(A(p))  imag(
                A(q))  ]  );
            text( ( real( A(p) ) + real( A(q) ) )/1.5, ( imag( A(p) )
                + imag( A(q) ) )/1.5, num2str(D(p,q)));
        end
    end
end
xlim([-1.2*d 1.2*d]); xlabel('x (m)');
ylim([-1.2*d 1.2*d]); ylabel('y (m)');
axis square;

%%%%%%%%%%%%%%%%%%%%%%%%%%%%%%%%%%%%%%%%%%%%%%%%%%%%%%%%%%%%%%%%%%%%%%%
%% Compute the wavefront distances between the antennas, over theta
%%%%%%%%%%%%%%%%%%%%%%%%%%%%%%%%%%%%%%%%%%%%%%%%%%%%%%%%%%%%%%%%%%%%%%%
%For every angle a around the antenna system, there are corresponding
%wavefront differences between each antennas.
%There are Np such differences between each of the antennas.
%These differences (in meters) are calculated and stored

wavefront_diff(Nr, Np) = zeros;
parfor a = 1:Nr
    %Observing from angle a corresponds to rotating a projected line
        between Antennas p and q
    a_th = exp( -i * theta(a) ); %Rotation angle

    temp1 = []; %Temp vars are required for parallelized for loop
```

Stellenbosch University https://scholar.sun.ac.za


```
    for p = 1 : N-1
        temp2 = zeros(1, N-p);

        for q = (p+1) : N
            %calculate wavefront diff in m between Antenna p and
                Antenna q
            temp2(q - p) = real( (A(q) - A(p)) * a_th );
            %Line between A(p) and A(q) is rotated and projected to
                obtain the wavelength diff (in m)
        end
        temp1 = [temp1 temp2]; %Differences are stored in a vector of
            length Np
    end
    wavefront_diff(a,:) = temp1; %Differences between antennas stored
        for each angle
end
clearvars temp1 temp2;
%The vector "wavefront_diff" now contains the differences in distance
    between
%antennas p and q for a wavefront from angle theta(a).
%For N = 4, this matrix has 6 columns.
%Vector is ordered to be the diff between A12, A13, A14, A23, A24, A34
    .

%%%%%%%%%%%%%%%%%%%%%%%%%%%%%%%%%%%%%%%%%%%%%%%%%%%%%%%%%%%%%%%%%%%%%%%
%% Phase differences dataset
%%%%%%%%%%%%%%%%%%%%%%%%%%%%%%%%%%%%%%%%%%%%%%%%%%%%%%%%%%%%%%%%%%%%%%%
%Now translate wavefront_diff into the phase_diff at each specified
    frequency point


%Step through frequency points and scale wavefront_diff (in meters) to
     be a
%phase difference - i.e. scale to lambda
phase_diff_dataset(Nf,Nr,Np) = zeros;
% phase_diff_dataset(n,Nf,Nr,Np(n)) = zeros;
for f = 1:Nf
    phase_diff_dataset(f,:,:) = wrapToPi( wavefront_diff * 2*pi / c *
        freq(f)) * 180/pi;
    %Wrapped to be bounded by [-pi pi] and converted to degrees
end

%%%%%%%%%%%%%%%%%%%%%%%%%%%%%%%%%%%%%%%%%%%%%%%%%%%%%%%%%%%%%%%%%%%%%%%
%% Correlation
%%%%%%%%%%%%%%%%%%%%%%%%%%%%%%%%%%%%%%%%%%%%%%%%%%%%%%%%%%%%%%%%%%%%%%%
%Measurement vectors are extracted from the phase differences dataset
    and
%have noise/error added, as defined by initialiised parameter snr_db.
%This noisy measurement is correlated over the dataset to test how
%sensitive the layout and frequency point is to noise.
```

Stellenbosch University https://scholar.sun.ac.za


```
%Variables must be preallocated for parfor loop.
error_RMSE(Nsnr,Nf,Nr) = zeros;
average_error(Nf) = zeros;
error_tally_above_5(Nf) = zeros;
error_tally_above_45(Nf) = zeros;
error_average(Nsnr) = zeros;
error_average_above_5(Nsnr) = zeros;
error_average_above_45(Nsnr) = zeros;
%Define anonymous function to calculate the root mean square error
   difference
%between the measured vector and the dataset matrix
findRMSE = @(vector, matrix) sqrt(mean( (matrix - repmat(vector, size(
   matrix, 1), 1)).^2, 2));

meas(1, Np) = zeros;
for s = 1:Nsnr %To only evaluate one SNR value, remove this loop
snr_db = SNR(s)
for f = 1:Nf
    %First reshape the 3D matrix (over f) into 2D (for specific f)
    dataset_f = reshape(phase_diff_dataset(f,:,:) , [Nr Np]);
    %We now have dataset of phase differences over angle range for
       freq f

    %Temp vector to store errors for using maximum correlation
    meas_w_noise_AoA_error = zeros(1,Nr);
    parfor a = 1:Nr
        %a is the index of the true AoA of our source for this
           measured vector

        meas = dataset_f(a,:);
        %This is the ideal phase_diff we expect from angle a

        snr = 10^(snr_db/10); %Linear snr
        var = 10800/snr; %noise variance
        %The number 10800 corresponds to the variance of a uniformly
        %distributed signal with values over -180 to 180. var = 1/12(b
           -a)^2

        meas_w_noise = meas + sqrt(var)*(randn(1, Np)); %Add noise

        %Now correlate a noisy measurement with the dataset
        meas_w_noise_RMSE = findRMSE(meas_w_noise, dataset_f );
        %This vector stores the total RMSE values over all angles.

        %Find the column with minimum RMSE -- index corresponds with
        %estimated AoA
        [minRMSE, index_estimate ] = min(meas_w_noise_RMSE);

        %Compute the error of the AoA estimation, in degrees
        meas_w_noise_AoA_error(a) =  wrapToPi(( index_estimate - a )
           *2*pi/Nr)*180/pi;
```

Stellenbosch University https://scholar.sun.ac.za


```
    end
    %Store the errors of the max correlation method, over all angles,
        for this f:
    error_RMSE(s,f,:) = meas_w_noise_AoA_error;

    %Plot the errors over theta for each f
    %-- only uncomment for single SNR calculations, and small Nf
%     figure; hold on; grid on;
%     plot(theta*180/pi - 180, circshift(reshape(error_RMSE(s,f,:),[1
    Nr]), round(Nr/2)));
%     if layout == 1
%         title(['AoA estimation error at ' num2str(freq(f)/1e6) ' MHz
     for N = ' num2str(N) ', varied layout. SNR = ' num2str(snr_db) '
    dB']);
%     else
%         title(['AoA estimation error at ' num2str(freq(f)/1e6) ' MHz
     for N = ' num2str(N) ', symmetrical layout. SNR = ' num2str(snr_db
    ) ' dB']);
%     end
%     xlabel('Source angle (in ^o)'); ylabel('Estimation error (in ^o)
    ');
%     xlim([-180 180]);
%     set(gca,'xtick', -180 : 45 : 180);
%     set(gca,'ytick', -180 :  45  : 180);

    %Find average error:
    average_error(s,f) = mean(abs(error_RMSE(s,f,:)));
    error_tally_above_5(s,f) = size(find( abs(error_RMSE(s,f,:)) > 5 )
        ,1);
    error_tally_above_45(s,f) = size(find( abs(error_RMSE(s,f,:)) > 45
         ),1);
end
% The following variables can be used to quantify the layout
    performance
% error_average(s) = mean(average_error(s,:)); %Average error over
    frequency range
% error_average_above_5(s) = sum(error_tally_above_5(s,:))/Nr/Nf; %
    Average amount of errors above 5degrees
% error_average_above_45(s) = sum(error_tally_above_45(s,:))/Nr/Nf; %
    Average amount of errors above 45degrees
end
% Plot the average error over freq and SNR
figure; surf(freq/1e6, SNR, average_error)
xlabel('Frequency (MHz)'); ylabel('Signal-to-noise ratio (dB)');
zlabel('Average AoA estimation error (in ^o)');
if layout == 1
    title(['Average AoA estimation error over frequency and SNR for N
        = ' num2str(N) ', asymmetrical layout.']);
else
    title(['Average AoA estimation error over frequency and SNR for N
        = ' num2str(N) ', symmetrical layout.']);
```

Stellenbosch University https://scholar.sun.ac.za


```
end

% As commented above -- a way to quantify performance
% average_error_for_configuration = sum(error_average)/Nsnr
% average_error_for_configuration_5 = sum(error_average_above_45)/Nsnr
% average_error_for_configuration_45 = sum(error_average_above_45)/
    Nsnr

%
% %%%%%%%%%%%%%%%%%%%%%%%%%%%%%%%%%%%%%%%%%%%%%%%%%%%%%%%%%%%%%%%%%%%
% %% Estimate AoA for real measurement data
% %%%%%%%%%%%%%%%%%%%%%%%%%%%%%%%%%%%%%%%%%%%%%%%%%%%%%%%%%%%%%%%%%%%
% %Below are the results of the field measurement conducted at
    Coetzenburg
% %2 layouts were tested, with 7 measurements each
%
% %The actual source angles for the measurements are stored as follows
    :
% actualAoA_0 =    0 + layout*5;  actualIndex_0 = round(actualAoA_0
    /360*Nr) + 1;
% actualAoA_1 = 2.55 + layout*5;  actualIndex_1 = round(actualAoA_1
    /360*Nr) + 1;
% actualAoA_2 =  5.1 + layout*5;  actualIndex_2 = round(actualAoA_2
    /360*Nr) + 1;
% actualAoA_3 =  7.6 + layout*5;  actualIndex_3 = round(actualAoA_3
    /360*Nr) + 1;
% actualAoA_4 = 10.1 + layout*5;  actualIndex_4 = round(actualAoA_4
    /360*Nr) + 1;
% actualAoA_5 = 12.5 + layout*5;  actualIndex_5 = round(actualAoA_5
    /360*Nr) + 1;
% actualAoA_45 = 45 - layout*2; actualIndex_45 = round(actualAoA_45
    /360*Nr) + 1;
% % The initial source position for the asymmetrical layout was offset
% % by approximately 5 degrees, because the source was placed in line
% % with Antennas 1 and 3, as a reference, hence the correction factor
    .
% % The 45 degree measurement was placed in line with Antennas 2 and 3
% % which corresponds to an offset of about 2 degrees
%
% %Below are the measured phase differences taken at 300 MHz and 480
    MHz
% %for layouts 1 (symmetrical) and 2 (asymmetrical)
% %The comments 1_0 -> 1_45 corresponds to the different measurements
% measuredData_300_0 = [-168.9590   41.2039 -147.2594  -149.8371
    21.6995  171.5366]; %1_0
% measuredData_300_1 = [ -30.9014  -37.4431  115.4434   -6.5416
    146.3448  152.8865]; %1_1
% measuredData_300_2 = [ -38.5852  -55.0929   85.6157  -16.5077
    124.2009  140.7086]; %1_2
% measuredData_300_3 = [-132.8669   31.3172 -176.7309  164.1842
    -43.8639  151.9519]; %1_3
```

Stellenbosch University https://scholar.sun.ac.za


```
% measuredData_300_4 = [-115.0283   34.5957  175.3081  149.6240
   -69.6636  140.7124]; %1_4
% measuredData_300_5 = [-104.2311   34.6747  167.2638  138.9057
   -88.5051  132.5891]; %1_5
% measuredData_300_45 = [ 19.4766   94.3803   93.5471   74.9036
   74.0704   -0.8332]; %1_45
%
% measuredData_480_0 = [106.6108  156.8550  106.3851   50.2442
   -0.2257  -50.4699]; %1_0
% measuredData_480_1 = [100.4607 -100.5465 -148.9424  158.9927
   110.5968  -48.3959]; %1_1
% measuredData_480_2 = [76.8744  -122.5591 -155.2543  160.5665
   127.8713  -32.6951]; %1_2
% measuredData_480_3 = [133.1099  166.3007   59.0348   33.1909
   -74.0750 -107.2659]; %1_3
% measuredData_480_4 = [148.7933  163.6742   37.9559   14.8809
   -110.8374 -125.7183]; %1_4
% measuredData_480_5 = [152.5001  171.2780   21.4197   18.7779
   -131.0803 -149.8583]; %1_5
% measuredData_480_45 = [15.7277  -21.5546  -47.4271  -37.2823
   -63.1548  -25.8724]; %1_45
%
% %These are measurements for the asymmetrical configuration.
% %It is therefore assumed that this is executed with layout = 1
% % measuredData_300_0 = [-149.8554   32.2103  177.3611 -177.9342
   -32.7835  145.1507]; %2_0
% % measuredData_300_1 = [-143.4129   31.6910  169.3902  175.1039
   -47.1968  137.6992]; %2_1
% % measuredData_300_2 = [-130.8919   34.0277  166.9747  164.9196
   -62.1334  132.9470]; %2_2
% % measuredData_300_3 = [-119.2617   34.2004  157.2168  153.4620
   -83.5215  123.0165]; %2_3
% % measuredData_300_4 = [-103.0861   34.5424  153.9280  137.6284
   -102.9860  119.3856]; %2_4
% % measuredData_300_5 = [ -88.2862   32.5605  149.8477  120.8467
   -121.8661  117.2873]; %2_5
% % measuredData_300_45 = [  0.0252   70.5272  105.5685   70.5020
   105.5433   35.0413]; %2_45
% %
% % measuredData_480_0 = [108.9384  171.4133   83.5935   62.4748
   -25.3449  -87.8197]; %2_0
% % measuredData_480_1 = [114.8359  177.0308   67.8295   62.1948
   -47.0064 -109.2013]; %2_1
% % measuredData_480_2 = [125.4160  173.2593   41.4650   47.8433
   -83.9510 -131.7943]; %2_2
% % measuredData_480_3 = [132.3807  177.7265   18.6332   45.3458
   -113.7474 -159.0933]; %2_3
% % measuredData_480_4 = [149.3711 -172.4400   -1.9661   38.1889
   -151.3371  170.4739]; %2_4
% % measuredData_480_5 = [161.9190 -171.2842   -6.6879   26.7969
   -168.6068  164.5963]; %2_5
```

Stellenbosch University https://scholar.sun.ac.za


```
% % measuredData_480_45 = [-8.4101  -91.3427  -27.3341  -82.9325
    -18.9240   64.0086]; %2_45
%
% %Store the expected phase differences dataset.
% %This assumes f_L = 300, f_H = 480, and Nf=2.
% dataset_f_300 = reshape(phase_diff_dataset(1,:,:) , [Nr Np]);
% dataset_f_480 = reshape(phase_diff_dataset(2,:,:) , [Nr Np]);
%
% %For interest's sake, store the expected differences, for contrast
% expectedDifferences_300_0 = dataset_f_300(actualIndex_0,:);
% expectedDifferences_300_1 = dataset_f_300(actualIndex_1,:);
% expectedDifferences_300_2 = dataset_f_300(actualIndex_2,:);
% expectedDifferences_300_3 = dataset_f_300(actualIndex_3,:);
% expectedDifferences_300_4 = dataset_f_300(actualIndex_4,:);
% expectedDifferences_300_5 = dataset_f_300(actualIndex_5,:);
% expectedDifferences_300_45 = dataset_f_300(actualIndex_45,:);
%
% expectedDifferences_480_0 = dataset_f_480(actualIndex_0,:);
% expectedDifferences_480_1 = dataset_f_480(actualIndex_1,:);
% expectedDifferences_480_2 = dataset_f_480(actualIndex_2,:);
% expectedDifferences_480_3 = dataset_f_480(actualIndex_3,:);
% expectedDifferences_480_4 = dataset_f_480(actualIndex_4,:);
% expectedDifferences_480_5 = dataset_f_480(actualIndex_5,:);
% expectedDifferences_480_45 = dataset_f_480(actualIndex_45,:);
%
% %Perform correlation on all measured points, 300 and 480MHz
% f_300_rmse_0 =  findRMSE(measuredData_300_0, dataset_f_300);
% f_300_rmse_1 =  findRMSE(measuredData_300_1, dataset_f_300);
% f_300_rmse_2 =  findRMSE(measuredData_300_2, dataset_f_300);
% f_300_rmse_3 =  findRMSE(measuredData_300_3, dataset_f_300);
% f_300_rmse_4 =  findRMSE(measuredData_300_4, dataset_f_300);
% f_300_rmse_5 =  findRMSE(measuredData_300_5, dataset_f_300);
% f_300_rmse_45 = findRMSE(measuredData_300_45, dataset_f_300);
%
% f_480_rmse_0 =  findRMSE(measuredData_480_0, dataset_f_480);
% f_480_rmse_1 =  findRMSE(measuredData_480_1, dataset_f_480);
% f_480_rmse_2 =  findRMSE(measuredData_480_2, dataset_f_480);
% f_480_rmse_3 =  findRMSE(measuredData_480_3, dataset_f_480);
% f_480_rmse_4 =  findRMSE(measuredData_480_4, dataset_f_480);
% f_480_rmse_5 =  findRMSE(measuredData_480_5, dataset_f_480);
% f_480_rmse_45 = findRMSE(measuredData_480_45, dataset_f_480);
%
% [min_300_0, index_300_0] = min(f_300_rmse_0);
% [min_300_1, index_300_1] = min(f_300_rmse_1);
% [min_300_2, index_300_2] = min(f_300_rmse_2);
% [min_300_3, index_300_3] = min(f_300_rmse_3);
% [min_300_4, index_300_4] = min(f_300_rmse_4);
% [min_300_5, index_300_5] = min(f_300_rmse_5);
% [min_300_45, index_300_45] = min(f_300_rmse_45);
%
% [min_480_0, index_480_0] = min(f_480_rmse_0);
```

Stellenbosch University https://scholar.sun.ac.za


```
% [min_480_1, index_480_1] = min(f_480_rmse_1);
% [min_480_2, index_480_2] = min(f_480_rmse_2);
% [min_480_3, index_480_3] = min(f_480_rmse_3);
% [min_480_4, index_480_4] = min(f_480_rmse_4);
% [min_480_5, index_480_5] = min(f_480_rmse_5);
% [min_480_45, index_480_45] = min(f_480_rmse_45);
%
% estimatedAoA_300_0 = theta(index_300_0)*180/pi;
% estimatedAoA_300_1 = theta(index_300_1)*180/pi;
% estimatedAoA_300_2 = theta(index_300_2)*180/pi;
% estimatedAoA_300_3 = theta(index_300_3)*180/pi;
% estimatedAoA_300_4 = theta(index_300_4)*180/pi;
% estimatedAoA_300_5 = theta(index_300_5)*180/pi;
% estimatedAoA_300_45 = theta(index_300_45)*180/pi;
%
% estimatedAoA_480_0 = theta(index_480_0)*180/pi;
% estimatedAoA_480_1 = theta(index_480_1)*180/pi;
% estimatedAoA_480_2 = theta(index_480_2)*180/pi;
% estimatedAoA_480_3 = theta(index_480_3)*180/pi;
% estimatedAoA_480_4 = theta(index_480_4)*180/pi;
% estimatedAoA_480_5 = theta(index_480_5)*180/pi;
% estimatedAoA_480_45 = theta(index_480_45)*180/pi;

%matlabpool close;

%% --> Please contact me @ mouritsdebeer@gmail.com if you need help in
    using or making sense of this code!
```

Stellenbosch University https://scholar.sun.ac.za

Appendix C

Manufacturing of the ACD

C.1 Model for 3D Printing

Figure C.1 below indicates the connecting region of the full diagram shown in Figure C.2 on the following page. Design decisions are discussed in Section 3.3.1.

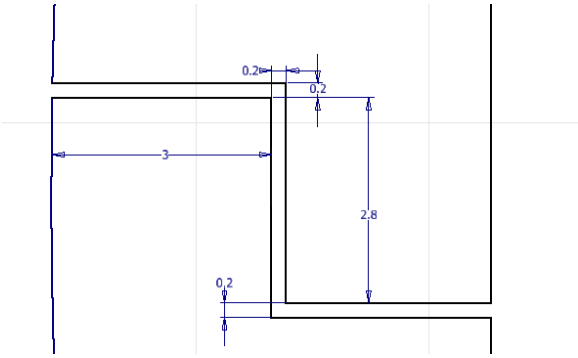

(a) Close-up of connection region for the old design.

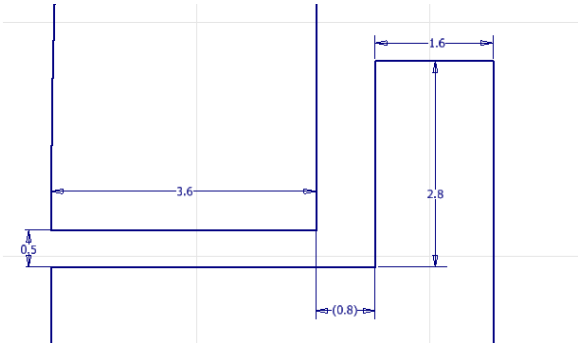

(b) Close-up of connection region for the final design.

Figure C.1: Schematics of the connecting region for the 3D model.

Stellenbosch University https://scholar.sun.ac.za

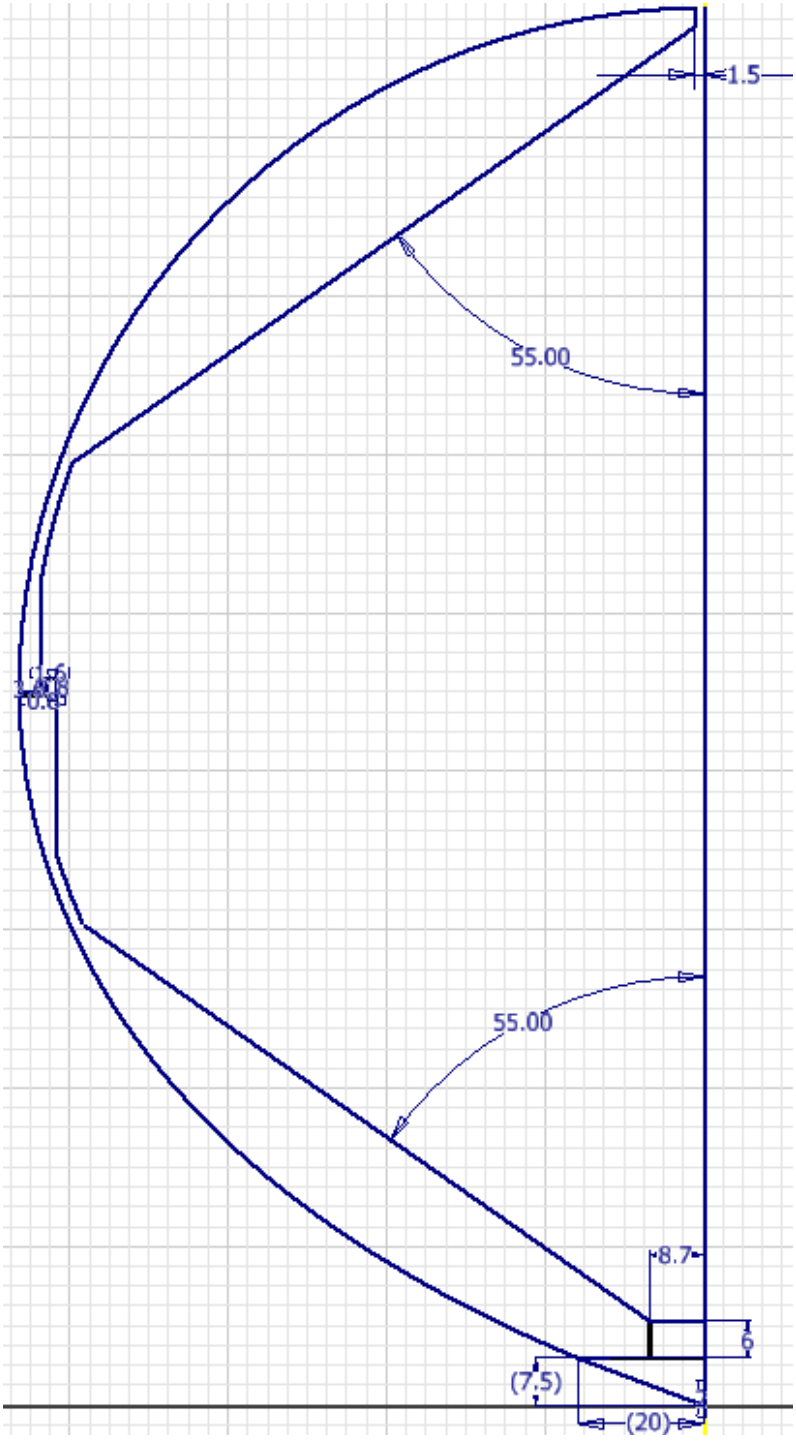

Figure C.2: Full schematic drawing of the ACD 3D model. All dimensions are in mm.

Stellenbosch University https://scholar.sun.ac.za

C.2 3D Printed Result

(a) Photo of the printed result after being conjoined.

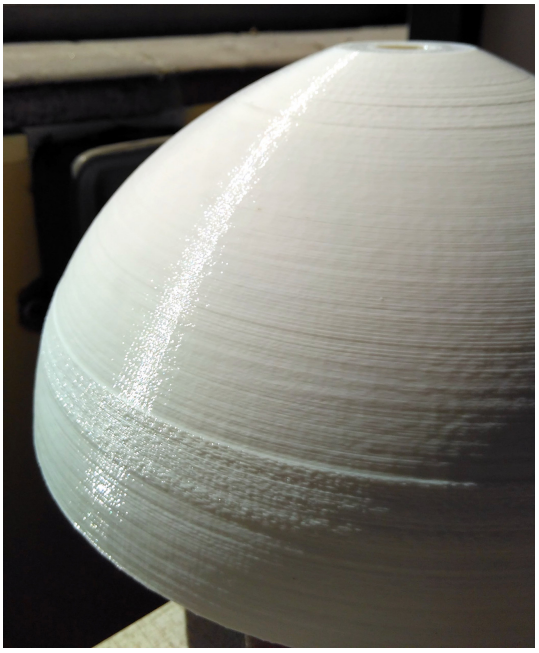

(b) Close-up view showing the texture on the surface of the printed model. Uneven features were smoothed with sandpaper.

(c) The transition region at the connection also required smoothing before aluminium tape was applied.

Figure C.3: Photos of the 3D printed model.

Stellenbosch University https://scholar.sun.ac.za

C.3 3D Printer Configuration

The Makerbot Z18 was the 3D printer that was used for the manufacturing of the ACD antennas. There are numerous printer settings that are critical in determining the time required to print, the amount of plastic used, and the quality of the result. A few of the most important settings are listed below:

- Infill pattern: Linear
- Infill density: 6%
- Infill layer height: 0.2 mm
- Model layer height: 0.2 mm
- Number of shells: 3
- Roof/floor thickness: 0.6 mm
- Chamber temperature: 40°C

The number of shells was adjusted to 3, because the default 2 shells generates some additional infill overhead, which adds 2-3 hours to the printing time. Furthermore, support structures must be activated for printing of the bottom hemisphere, due to the 90° edge at the connection.

With these settings, each of the hemispheres required about 15 hours of printing time, and used 230 g of plastic. This translates to 60 hours of printing time for a full dipole, at almost 1kg of plastic.

Stellenbosch University https://scholar.sun.ac.za

C.4 Centre Feed

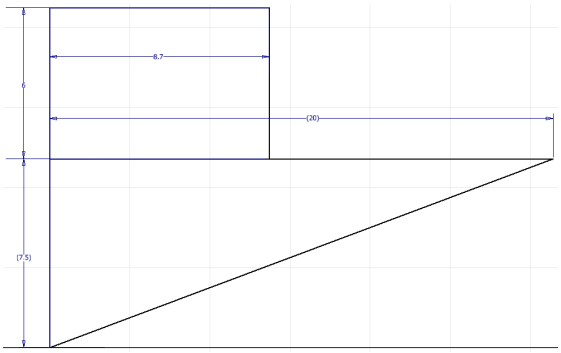

(a) Schematic with radial dimensions (mm)

(b) Photo of cable and feed interface.

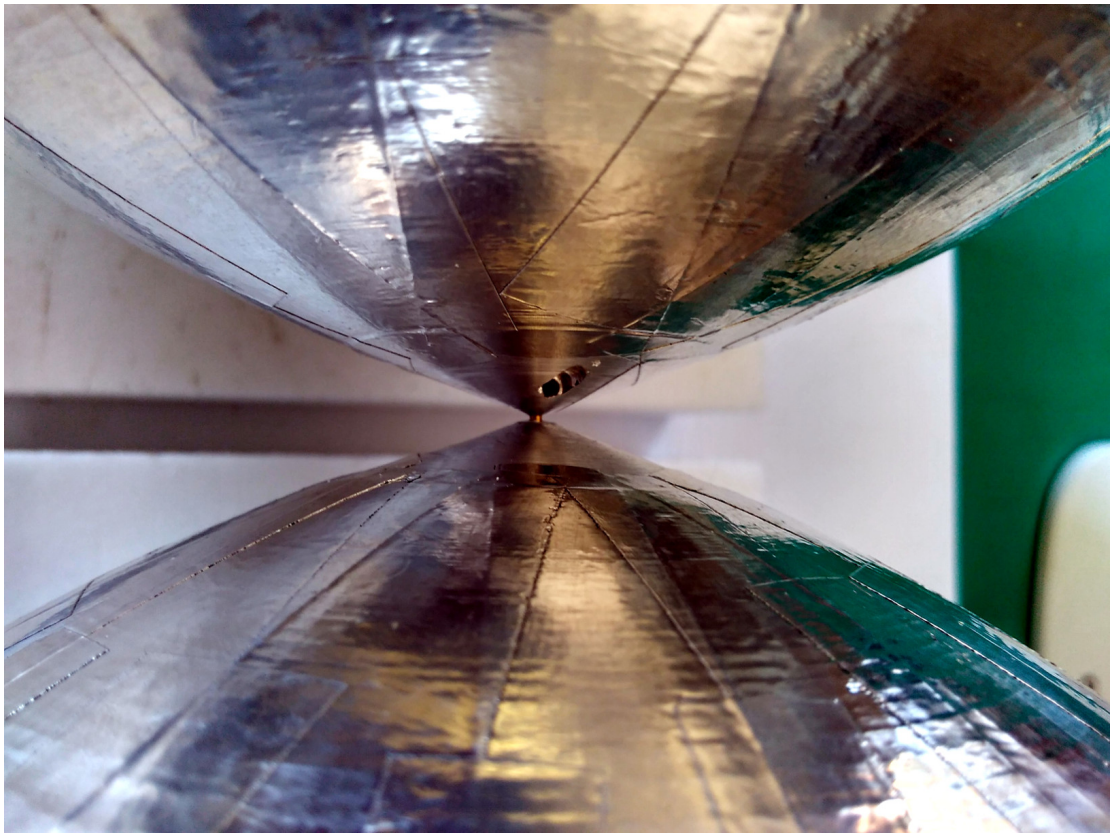

(c) Close-up photo of the tunable feed gap, showing the hole for a 1 mm hex key.

Figure C.4: Centre feed connection for the ACD.

Stellenbosch University https://scholar.sun.ac.za

C.5 Structural Design

The support structure for the manufactured ACD was designed by Wessel Croukamp of the Stellenbosch University's Electrical Department. The design was made of the commercial product, IsoBoard, an insulating material that was cut into a triangular structure with three support columns that held the ACD in place. The top-view dimensions for the cuts are shown in the diagram below. Vertical dimensions for the columns are around the height of the ACD, of 45 cm.

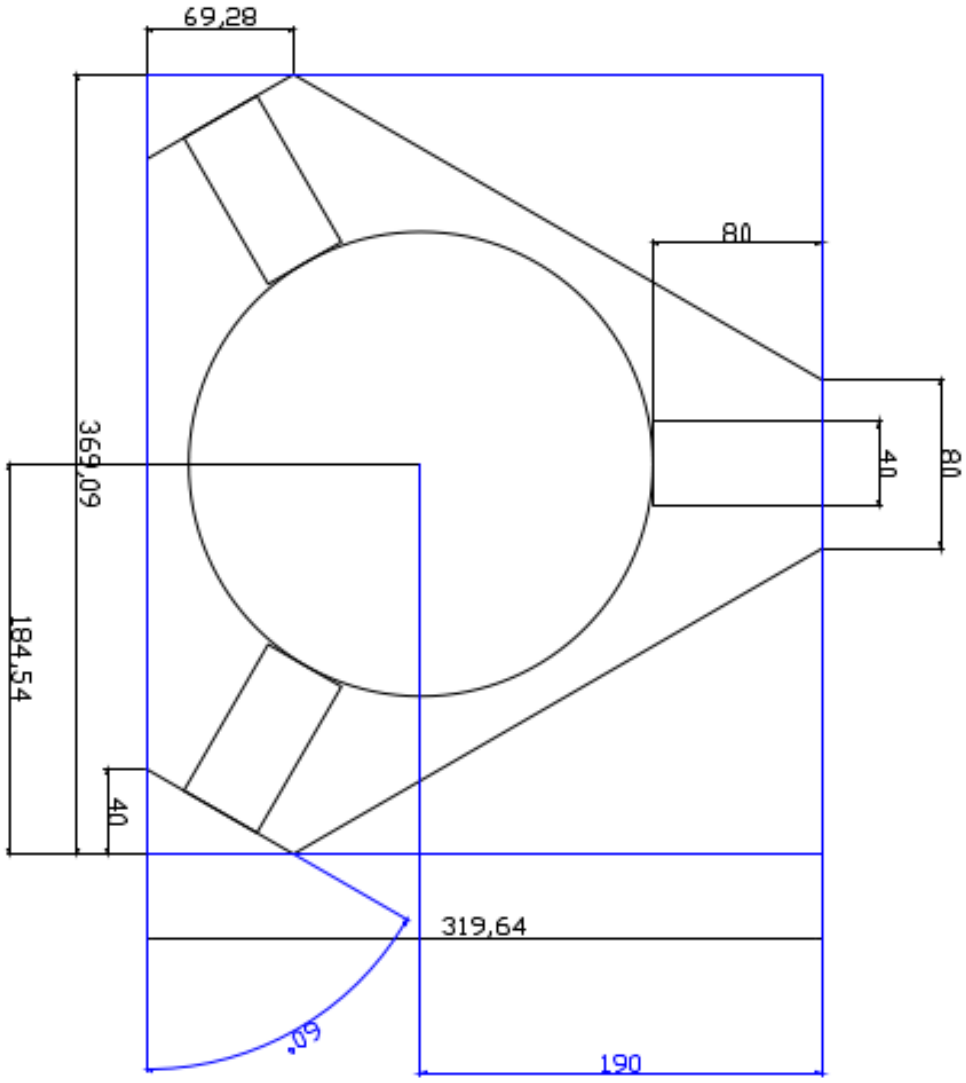

Figure C.5: Top view diagram of the physical support structure.

Stellenbosch University https://scholar.sun.ac.za

C.6 Reflection Coefficient Measurement of the Four ACDs

From the results below, it is evident that the first manufactured antenna achieved the best response. This is believed to be due to the care that was taken for the first implementation: the aluminium tape was applied smoothly with very few creases. In subsequent manufacturing of the final three antennas, the tape was indeed applied carefully, but additional folds may have resulted in a worsened high frequency response.

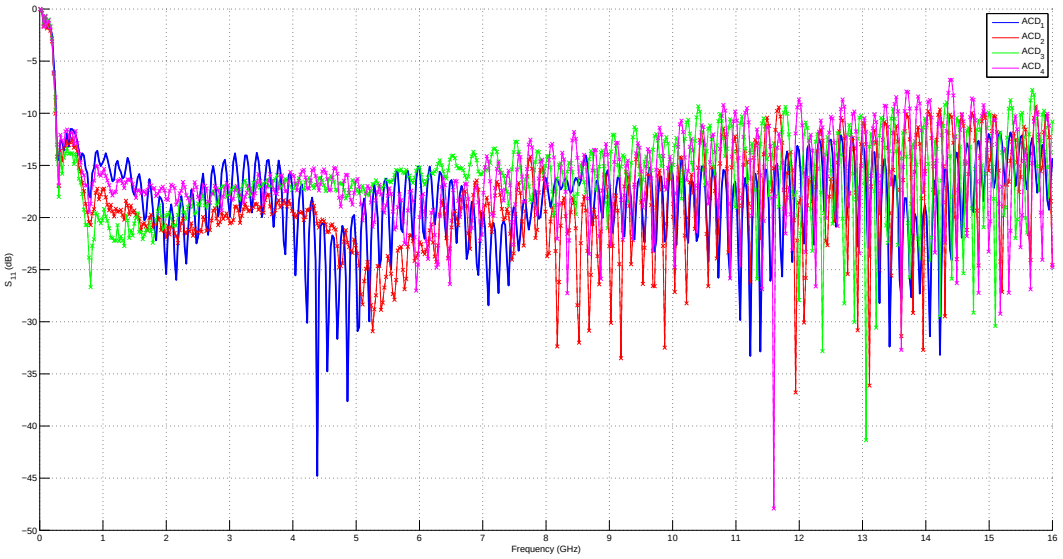

Figure C.6: Reflection coefficient for each of the 4 ACD antennas.

Stellenbosch University https://scholar.sun.ac.za

C.7 Reflection Coefficient Measured up to 50 GHz

The first manufactured ACD was measured up to 50 GHz on the Agilent 8510C VNA. The specific cable used (aluminium/tin-coated EZ-141 conformable cable) is only rated up to 33 GHz, after which cable attenuation will begin to influence the result.

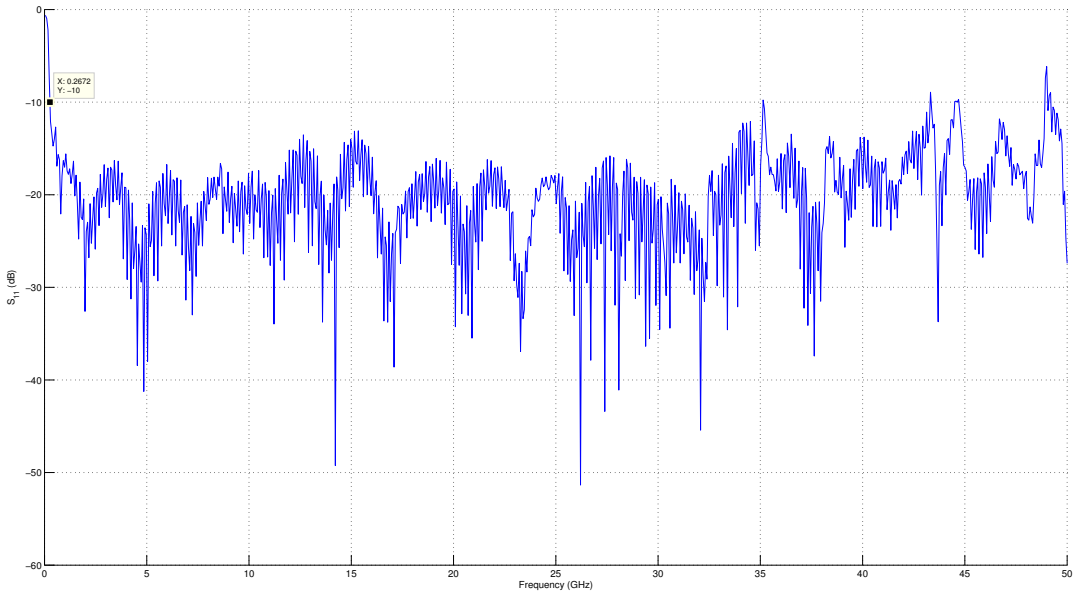

Figure C.7: Reflection coefficient of the ACD, measured up to 50 GHz. The cable limitation can be seen to create disturbance in the measurement past 33 GHz. Any result past this point is affected by cable attenuation, and not representative of antenna performance.

Stellenbosch University https://scholar.sun.ac.za

Appendix D

Additional DF Algorithm Results

D.1 Ambiguity Errors

The figure below shows the factor of total angle estimates that have errors greater than 45°, for the symmetrical and asymmetrical layout, as complement for the results provided in Section 4.3. The plot indicates that large ambiguity errors only occur for the asymmetrical layout once SNR levels fall below 24 dB. The symmetrical layout, however, yields a large proportion of errors even for SNR above 36 dB.

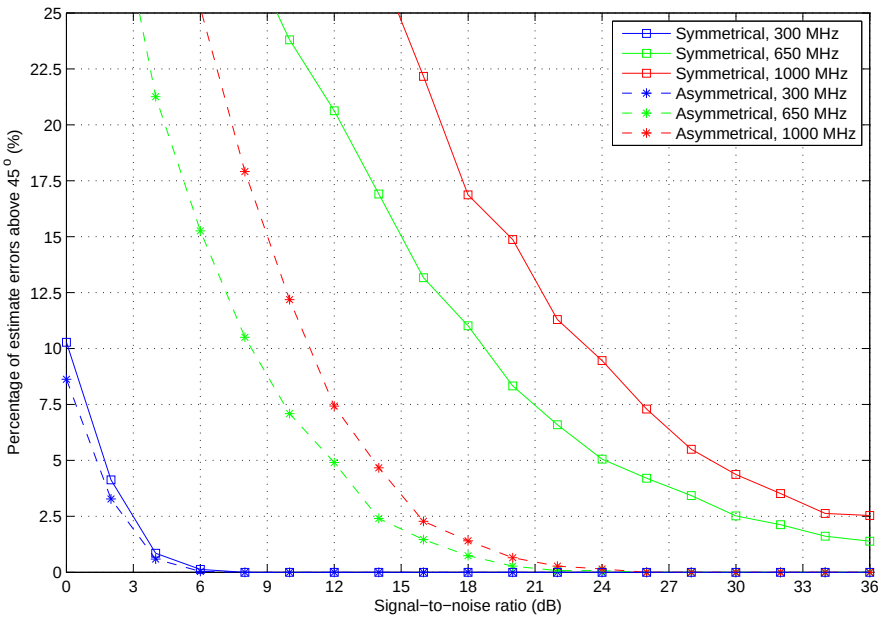

Figure D.1: Percentage of AoA estimate errors that are greater than 45°, at different frequencies, for symmetrical and asymmetrical layout.

Stellenbosch University https://scholar.sun.ac.za

D.2 Field Measurement Expected Results

The following results were computed for layouts designed with a separation distance of 1 m, which corresponds to a $f_L = 150$ MHz. These are the expected results for the AoA estimation performed in Section 5.3.2, assuming an SNR of 26 dB. For the different measurements performed, we therefore expect the symmetrical layout to give incorrect estimates around source angles $\theta = 0°$, while the varied layout should yield estimates within 2° accuracy.

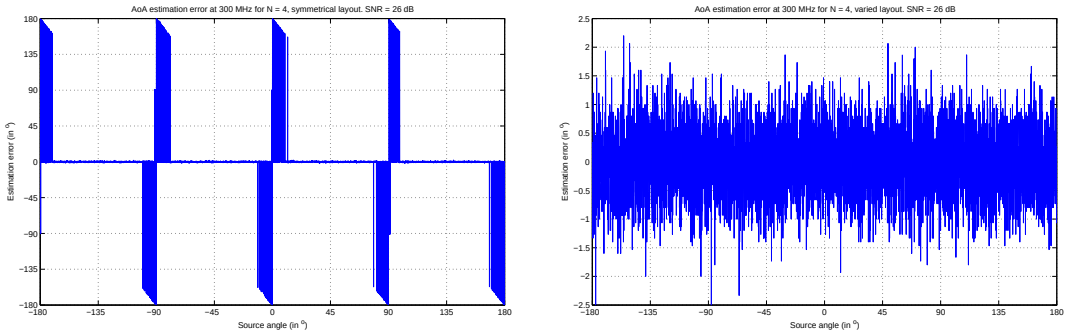

(a) $f = 300$ MHz

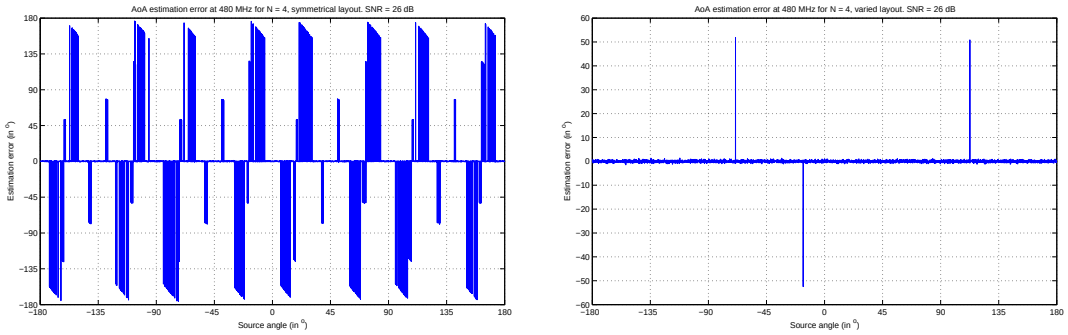

(b) $f = 480$ MHz

Figure D.2: Expected AoA estimation errors for the final measurement configurations, evaluated for an SNR of 26 dB (phase error σ of 5°). The symmetrical layout is on the left, with varied spacing on the right.

Stellenbosch University https://scholar.sun.ac.za

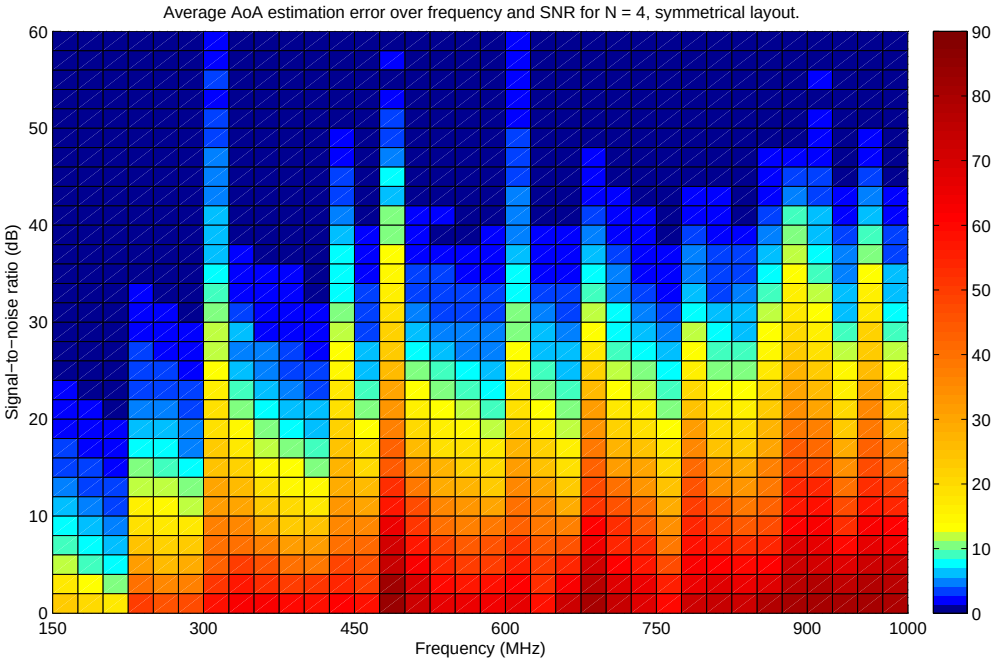

(a) Average estimation error for the symmetrical layout

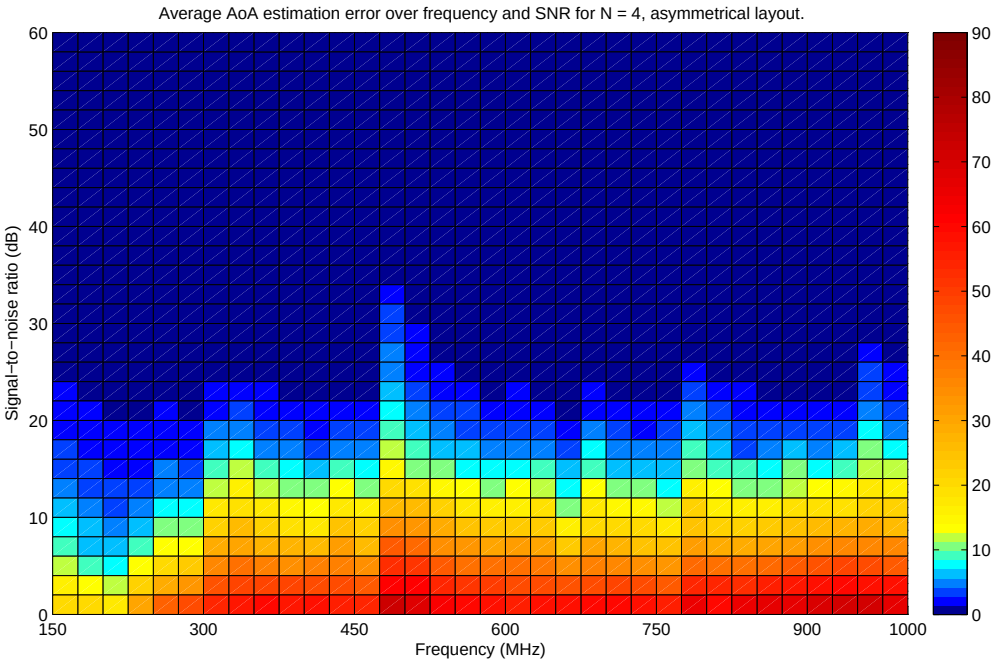

(b) Average estimation error for the asymmetrical layout

Figure D.3: Colour map plots of the mean AoA estimation error for the final field measurement configurations.

Stellenbosch University https://scholar.sun.ac.za

D.3 Root-Mean-Square Error Plots

The below figures show the result of the correlation (RMSE function) applied for the measurements over the expected phase difference dataset. The points of minimum value correspond with the estimated AoA.

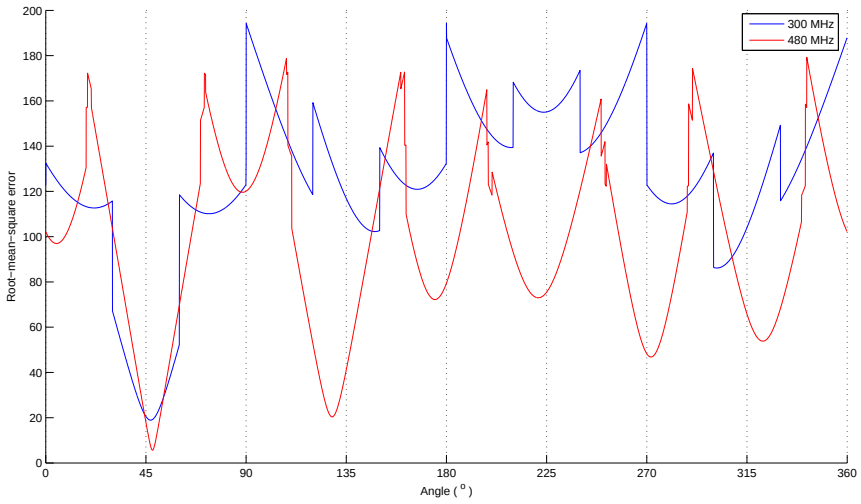

(a) RMSE for symmetrical layout.

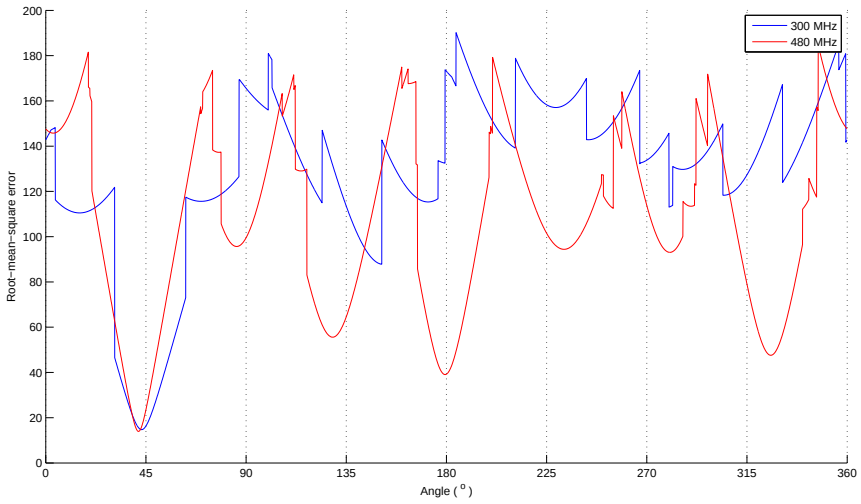

(b) RMSE for asymetrical layout.

Figure D.4: Root-mean-square error plots for a source angle of 45°. Accurate angular resolution was obtained, but it is evident that the higher frequency case is much more sensitive to noise, due to the amount of low-RMSE points.

Stellenbosch University https://scholar.sun.ac.za

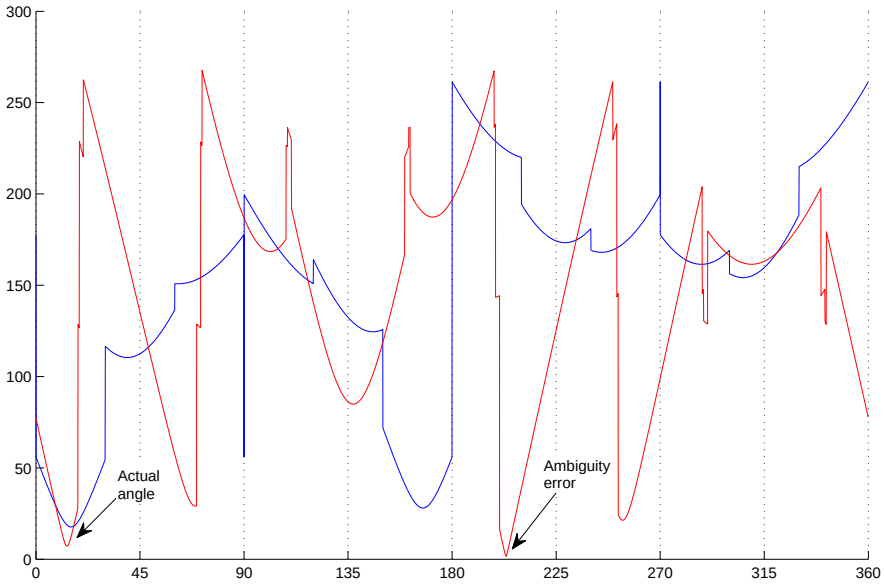

Figure D.5: RMSE plot for the asymmetrical layout, and a source angle of 12.5°. The blue plot is for 300 MHz, and the red for 480 MHz. Using maximum correlation returns an ambiguity error greater than 180°.